A Unified and Microscopic Approach to Astrophysical Nuclear Reactions using Fermionic Molecular Dynamics

---

Vom Fachbereich Physik
der Technischen Universität Darmstadt

zur Erlangung des Grades
eines Doktors der Naturwissenschaften
(Dr. rer. nat.)

genehmigte Dissertation von

M.Phys. Robert Cussons
aus Binfield

Darmstadt 2008
D17

Referent: Prof. Dr. H. Feldmeier
1. Korreferent: Prof. Dr. K. Langanke

Tag der Einreichung: 16 Juni 2008
Tag der Prüfung: 9 Juli 2008

For my parents without whom I would never have begun this

and for my wife without whom I would never have finished it.

Man’s mind, once stretched by a new idea,
never regains its original dimensions.

- Oliver Wendell Holmes Sr.

Contents

Abstract

The aim of nuclear astrophysics is to understand the formation of the elements and the role played by nuclear reactions in the evolution of the universe, specifically by studying the complex interactions which occur on a microscopic scale between nuclei. To achieve this we must complement our understanding of how processes proceed on a quantum mechanical nuclear scale with observations made on an astrophysical scale, with the aim of improving our understanding of the universe in which we live.

In this thesis a method will be described by which the astrophysical S-factor of radiative capture reactions can be calculated in a microscopic and unified way. Fermionic Molecular Dynamics (FMD) will be used to construct a non-orthogonal many-body basis out of explicitly antisymmetrised and angular momentum projected Slater determinants. The single particle basis states consist of gaussian wave packets which are localised in coordinate and momentum space and possess different widths.

This provides an over-complete basis that can describe both scattering and bound states of nuclei. These serve as initial and final states, respectively, in the calculation of the transition matrix elements for electromagnetic transitions. By multiplying with the appropriate phase space factors, the cross section and hence the S-factor for radiative capture reactions can be calculated.

In a microscopic description of nuclei an effective interaction between nucleons is required that is consistent with the chosen many-body basis. Realistic nucleon-nucleon potentials that perfectly describe the two-body phase shift data induce short-range correlations, which cannot be represented by the Slater determinants used in FMD. Therefore the Unitary Correlation Operator Method (UCOM) is employed to create an effective interaction that by construction delivers the same phase shifts as the realistic interaction.

To formulate boundary conditions for the scattering states in the FMD basis the Collective Coordinate Representation (CCR) is used. This enables an operator to be defined that measures the relative distance between two well separated, completely antisymmetrised, many-body states.

By matching to the known solution of the Coulomb problem for two point charges, the resonance energies and widths as well as the phase shifts can be calculated and compared with experimental data.

Two radiative capture reactions which are of astrophysical interest are investigated: $^{3}\mathrm{He}(\alpha,\gamma)^{7}\mathrm{Be}$ and $^{14}\mathrm{C}(\alpha,\gamma)^{18}\mathrm{O}$. The energy spectra of the compound nuclei are then compared with the experimental data for bound and resonant states.

In the case of $^{3}\mathrm{He}(\alpha,\alpha)^{3}\mathrm{He}$ scattering, for which measurements of the elastic scattering phase shifts exist, comparisons are made to the calculations for both resonant and non-resonant channels. The agreement of the microscopic calculation with the experimental data is amazingly good considering that no use is made of an optical potential which has been fitted to the scattering data. The role of the nucleus-nucleus potential is fulfilled by the microscopic nucleon-nucleon interaction between the projectile and the target.

For both reactions the astrophysical S-factor is calculated in separate partial waves at the low energies relevant for astrophysics for the chosen FMD model spaces. For the $^{3}\mathrm{He}(\alpha,\gamma)^{7}\mathrm{Be}$ reaction, this result is then compared with experimental data.

Zusammenfassung

Die nukleare Astrophysik versucht die Entstehung der Elemente und die Rolle, die kernphysikalische Prozesse in der Entwicklung des Universums spielt, auf der Grundlage von komplexen Reaktionen zu verstehen, die auf mikroskopischer Skala zwischen Atomkernen stattfinden. Um das zu erreichen, müssen wir unsere Vorstellungen wie die Prozesse auf der quantenmechanischen nuklearen Skala ablaufen mit den Beobachtungen in astrophysikalischen Längenskalen vereinen, um das Universum, in dem wir leben, besser zu verstehen.

In dieser Arbeit wird eine Methode beschrieben, mit der astrophysikalische S-Faktoren für Strahlungseinfangreaktionen in einem vereinheitlichten mikroskopischen Modell berechnet werden können. Die Fermionische Molekulardynamik (FMD) wird benutzt, um eine nichtorthogonale Vielteilchenbasis aus explizit antisymmetrisierten und drehimplusprojizierten Slaterdeterminanten aufzubauen. Die Einteilchenbasiszustände bestehen aus gaußförmigen Wellenpaketen, die im Orts- und Impulsraum lokalisiert sind und variable Breite aufweisen.

Damit erhält man eine übervollständige Basis, mit der man sowohl Vielteilchenstreuzustände als auch gebundene Kernzustände darstellen kann. Diese können dann als Anfangs- und Endzustände bei der Berechnung von Übergangsmatrixelementen für elektromagnetische Übergänge dienen. Nach Multiplikation mit den entsprechenden Phasenraumfaktoren erhält man den Wirkungsquerschnitt und den S-Faktor für Strahlungseinfang.

In einer mikroskopischen Beschreibung benötigt man außerdem eine effektive Wechselwirkung zwischen Nukleonen, die konsistent mit der gewählten Vielteilchenbasis ist. Realistische Nukleon-Nukleon-Potentiale, die Streudaten des Zweiteilchensystems perfekt beschreiben, induzieren kurzreichweite Korrelationen, die nicht mit den Slaterdeterminanten der FMD dargestellt werden können. Deshalb wird eine mit der Unitären Korrelator Operator Methode (UCOM) gewonnene effektive Wechselwirkung benutzt, die per Konstruktion die gleichen Streuphasen wie die Ausgangswechselwirkung besitzt.

Um für die in der mikroskopischen FMD Darstellung gegebenen Kern-Kern-Streuzustände Randbedingungen zu formulieren, wird die sogenannte “Collective Coordinate Representation” benutzt, die es erlaubt, für Drehimpulseigenzustände eines komplett antisymmetrischen Vielteilchenzuständs für große Abstände der streuenden Kerne ein Operator für den Relativabstand zu definieren.

Durch Anpassen an die bekannten Lösungen des Coulombproblems für zwei Punktladungen bei großen Abständen werden damit Resonanzenergien und Resonanzbreiten sowie Streuphasen berechnet, die dann mit experimentellen Daten verglichen werden.

Zwei Reaktionen mit Strahlungseinfang, die von astrophysikalischen Interesse sind, ^{3}He$(\alpha,\gamma)^7$Be und ^{14}C$(\alpha,\gamma)^{18}$O, werden untersucht. Die Energiespektren der Compoundkerne werden mit den experimentellen Daten für gebundene Zustände und Resonanzen verglichen.

Für ^{3}He$(\alpha,\alpha)^3$He, wo gemessene Streuphasen für elastische Streuung existieren, werden diese mit den Rechnungen sowohl für resonante als nicht resonante Kanäle verglichen. Die Übereinstimmung der mikroskopischen Rechnung mit den Daten ist erstaunlich gut, bedenkt man, dass keine an die Streudaten angepassten optischen Potentiale Verwendung finden. Die Rolle der Kern-Kern-Potentiale wird durch die mikroskopische Nukleon-Nukleon-Wechselwirkung zwischen Projektil und Target übernommen.

Für beide Reaktionen wird der astrophysikalische S-Faktor bei niedrigen Energien für die im gewählten FMD Modellraum vertretenen Partialwellen berechnet und für ^{3}He$(\alpha,\gamma)^7$Be mit vorhandenen Daten verglichen.

1. Introduction

1.1. Nuclear astrophysics

Nuclear astrophysics is the branch of physics concerned with trying to understand the origin of the elements and the evolution of the universe in terms of the complicated interactions that occur between nuclei on a microscopic scale. To achieve this we must unify our vision of how processes are mediated on a nuclear scale, which is encapsulated in quantum mechanics, and to build up from this microscopic framework an understanding of how the universe comes to be as we observe it on an astrophysical scale.

At first glance this may seem certain to require the use of enormous computing power, yet the pioneering work on the synthesis of the elements by Burbidge, Burbidge, Fowler and Hoyle [3] was published over fifty years ago. There has been much work done in the period since then, from looking at how relatively light stars like the sun produce their energy to how heavier stars provide the ingredients needed to make up the solar system's, the Earth's and even our bodies' elemental abundances and how these stars then go on to form neutron stars or black holes.

In this thesis a number of reactions that occur in stars are investigated in the framework of a unified and microscopic nuclear model: Fermionic Molecular Dynamics (FMD) [10][14]. The reactions studied range from those that are occurring in the sun at the moment such as $^{3}\mathrm{He}(\alpha,\gamma)^{7}\mathrm{Be}$, to reactions that will occur during its last throes of life in about five billion years time when it becomes a red giant star: $^{14}\mathrm{C}(\alpha,\gamma)^{18}\mathrm{O}$.

One of the main aims in nuclear astrophysics is to determine the processes that occur within the universe that produce the elemental abundances we observe. These abundances are determined by the various nuclear and electromagnetic processes that produce the elements. They are normally strongly dependent on the properties of the production site, particularly the density, temperature and nuclear elemental abundances. They are also of course heavily influenced by the forces that mediate the reactions. As the reactions occur below the Coulomb barrier on a distance scale on the order of femtometres, the processes are quantum mechanical in nature.

The quantity which is essential in calculating elemental abundances is the reaction rate per particle pair $\langle \sigma v \rangle$, as this determines the amount of an isotope that is created and destroyed in a particular astrophysical environment. This rate depends on the cross section $\sigma(E)$, the density and the mean velocity of the nuclei, which is given by the temperature.

In this thesis radiative capture reactions will be considered in which two nuclei A and B fuse together and their relative kinetic energy plus the binding energy of a bound state in the compound nucleus C is emitted in the form of a photon γ. This is commonly written in the abbreviated form: $A(B, \gamma)C$. Reactions of this type are very common in astrophysics and provide the capture part of the path by which the r, s, p and rp processes proceed, respectively through neutron and proton captures.

The method described in this thesis would also be applicable to particle exchange reactions in which two nuclei collide and exchange a number of particles and then depart again as two different nuclei. However this is yet to be investigated.

1.2. The nuclear many-body problem

The aim of this thesis is to calculate cross sections and thereby estimate reaction rates for a number of astrophysically relevant radiative capture reactions. To achieve this a description of both the incoming and outgoing channels is required. The incoming channel is composed of two nuclei that are well separated and are referred to as cluster states. These are calculated at a number of different scattering energies in a range that is relevant to the astrophysical scenario under consideration.

The fusion of the two incoming nuclei can occur either through a resonant or non-resonant reaction. In the non-resonant case, the two clusters come together with a certain relative kinetic energy (or scattering energy) and decay to a particular bound state in the compound nucleus by emitting a γ-ray, in accordance with the selection rules for electromagnetic transitions. If a resonance exists at the energy corresponding to the scattering energy of the two clusters, then the clusters can form a metastable or resonant state in the compound nucleus. This state lives for a certain time, which increases the probability for it to decay through the emission of a γ-ray to an allowed bound state in the compound nucleus, rather than separating back into the two incoming clusters. The presence of the resonance state in the compound nucleus thus results in a peak in the reaction cross section near to the resonance energy; the width of the peak is inversely proportional to the lifetime of the resonance.

An excited state of the compound nucleus will decay by γ-ray emission to the ground or another excited state at lower energy, meaning that the bound states have a characteristic width for decay by γ-ray emission, known as their γ width Γ_γ. If the bound state in question is just below the particle emission threshold energy[1] then the γ-width of this state can extend above the threshold, making the bound state behave like a resonance in radiative capture reactions. Consequently states such as this are known as sub-threshold resonances. Being close to the particle emission threshold also means that the tail of the wave function of these bound states can extend a very long way under the Coulomb barrier. This increases the transition matrix element and hence the cross section relative to more deeply bound states. For both of these reasons, bound states close to the particle emission threshold can make an important contribution to radiative capture reaction rates [27][35]; an example of this is the second 1^- state in ^{18}O.

Typical temperatures in non-explosive stellar environments are of the order of 10^7-10^9 K, corresponding to energies $\approx$ 1-100 keV. These reactions are often very difficult or impossible to measure in the laboratory at astrophysical energies due to the incredibly low cross section caused by the scattering wave having to penetrate so far through the Coulomb barrier. For this reason, it is often necessary to extrapolate from the measured data to lower energies using theoretical models. The calculation of both the resonant and non-resonant contributions to the reaction rate is possible in a microscopic and unified way within the framework of the nuclear many-body model FMD.

To describe the incoming channel the scattering states for the relevant partial waves must be calculated. This involves solving the nuclear many-body problem with boundary conditions appropriate for scattering. This is done by solving the Schrödinger equation for the relative motion of the clusters. The time-independent Schrödinger equation:

$$\underset{\sim}{H}\big|\, \Psi_i \,\big\rangle = E_i\big|\, \Psi_i \,\big\rangle, \tag{1.1}$$

is appropriate for calculating the scattering states $\big|\, \Psi_i \,\big\rangle$ as we seek, for a particular incoming relative kinetic energy E_i, stationary states of the Hamiltonian $\underset{\sim}{H}$ that describes the interactions involved in the scattering process[2].

In the case of narrow resonances (whose width Γ is much smaller than their energy E_R), using the formulation of Gamow states [17], the energy and width of the resonant state can be found by solving equation (1.1), with an outgoing wave as a boundary condition. This is equivalent to solving the time-dependent Schrödinger equation for a decaying resonance because the resonant state may be well approximated by a stationary state with a slowly decreasing amplitude. This means that the shape of the wave function within the range of the nuclear interaction essentially does not change over time, its amplitude merely slowly decreasing as a small probability flux leaks out through the Coulomb barrier.

---

[1] The threshold energy is given by the sum of the binding energies of the clusters minus the binding energy of the compound nucleus.

[2] A list of the nomenclature and conventions used in this thesis is included in appendix A.3.

1.3. The required tools

The ingredients that are required to formulate the nuclear many-body problem are a basis and an interaction. In FMD a set of Slater determinants, each constructed as an antisymmetrised product of Gaussian single-particle states, is used to describe the many-body states; this will be further described in section 2.1. The Gaussian basis makes it very versatile in describing a wide range of nuclear phenomena from cluster structure to halo nuclei which can be observed in both bound states and resonances of nuclei.

The interaction that is used herein is derived from the realistic two-body interaction known as the Argonne-V18 interaction (AV18) [51] which is “tamed” by the use of the Unitary Correlation Operator Method (UCOM) [13] to arrive at a correlated interaction in which the low and high momentum components are decoupled from one another. This decoupling enables the simple FMD basis states to be used with a correlated, but still realistic, AV18 interaction. This correlated interaction is then referred to as V_{UCOM}, which is discussed further in section 2.2.

To describe scattering reactions among nuclei, states that represent the asymptotic part[3] of the Hilbert space must be included in the model space. The Gaussians that make up the FMD many-body states can be easily shifted in coordinate space, therefore the nuclei can be positioned at different relative distances, for an example of this see figure 2.5. These and other configurations of FMD states can also be used to calculate the bound states of the compound nucleus, thus enabling the same basis states and interaction to be used to describe both scattering and bound states of nuclei. Other configurations that are often added to the model space to improve the descriptions of bound states are FMD states minimised under constraints (see section 2.1.3), examples of these are shown in figure 4.9.

The cross section for electromagnetic transitions between these bound and scattering states can then be calculated. From this the astrophysical S-factor and reaction rates for different radiative capture reactions can be deduced. Hence the approach is unified in its consistent use of the same states and interaction throughout the calculation of a particular reaction.

In summary, the same interaction and model space can be used to describe bound, scattering and resonance phenomena and from these calculated states the cross section and astrophysical S-factor can be deduced; leading to a microscopic and unified description of radiative nuclear capture reactions.

The next chapter describes a theoretical framework in which the principles of quantum mechanics and specifically the model of FMD, can be brought to bear on calculating reaction properties.

---

[3] Asymptotic in this context means corresponding to relative distances much larger than the radius of the nucleus.

2. Theoretical Framework

In this chapter the theoretical framework for this thesis will be laid out. The different elements that are required for solving the various many-body problems that are considered later in the thesis form the sections of this chapter.

To solve the time-independent Schrödinger equation (1.1) in an A-body Hilbert space $\mathfrak{H}^{[A]}$, the abstract mathematics of (1.1) must be connected to physical reality. This is achieved by specifying the relevant degrees of freedom and the interactions of the system under consideration. As the aim is to describe nuclei at low energies, the protons and neutrons are considered as the elementary components of the nucleus because the first excited state of a nucleon, the Δ-resonance, is at an excitation energy of 300 MeV and thus will only be virtually excited. Hence, the elementary degrees of freedom of the nucleons are taken to be:

1. Their centre of mass positions (nucleons are extended objects with a radius of about 0.7 fm).
2. Their spin.
3. Their isospin.

The next step is to set up a many-body Hilbert space $\mathfrak{H}^{[A]}$ for A nucleons describing these degrees of freedom. First one defines the properties of states $\left|\, \psi \,\right\rangle$ and operators $\underset{\sim}{a}$ in the one-body Hilbert space $\mathfrak{H}$. In line with the postulated degrees of freedom, the single-particle Hilbert space is regarded as a tensor product of a spatial Hilbert space $\mathfrak{H}^{space}$ of infinite dimensions, times a two dimensional spin space $\mathfrak{H}^{spin}$, times a two dimensional isospin space $\mathfrak{H}^{isospin}$

$$\mathfrak{H} = \mathfrak{H}^{space} \otimes \mathfrak{H}^{spin} \otimes \mathfrak{H}^{isospin} \ . \tag{2.1}$$

The A-body Hilbert space is then written as a tensor product of one-body Hilbert spaces:

$$\mathfrak{H}^{A} = \underbrace{\mathfrak{H} \otimes \mathfrak{H} \otimes \ldots \otimes \mathfrak{H}}_{\text{A times}} \ . \tag{2.2}$$

2.1. Fermionic Molecular Dynamics (FMD)

FMD is a microscopic and unified approach to nuclear structure and reactions. It is microscopic in the sense that it takes the degrees of freedom of the individual nucleons: the centre of mass positions, spins and isospins as the fundamental degrees of freedom of the system and uses a fully antisymmetrised wave function to describe the many-body problem. It is unified because in describing scattering, resonant and bound states, the same interaction and Hilbert space are used throughout.

Our first goal is to describe an A-body nucleus within the framework of FMD. The nucleus is composed of neutrons and protons which are both fermions and as such are subject to the Pauli exclusion principle. Therefore the A-body state representing the nucleus must be antisymmetric with respect to the exchange of any two of the single-particle states. This is achieved by applying the antisymmetrisation operator $\underset{\sim}{\mathcal{A}}$ to the many-body state. In this work $\underset{\sim}{\mathcal{A}}$ is defined as:

$$\underset{\sim}{\mathcal{A}} = \frac{1}{A!} \sum_{\text{all } \mathcal{P}}^{A!} \operatorname{sgn}(\mathcal{P}) \, \underset{\sim}{\mathcal{P}} \ , \tag{2.3}$$

where $\underset{\sim}{\mathcal{P}}$ is the operator that performs the permutations through a number of transpositions. Hence, the right hand side of (2.3) is to be read as the sum of all permutations, of which there are $A!$, where $\operatorname{sgn}(\mathcal{P}) = (-1)^{n_T}$ and n_T is the number of transpositions required to achieve the permutation $\mathcal{P}$. Using this definition $\underset{\sim}{\mathcal{A}}$ is a projection operator:

$$\underset{\sim}{\mathcal{A}}^2 = \underset{\sim}{\mathcal{A}} \ , \qquad \underset{\sim}{\mathcal{A}}^\dagger = \underset{\sim}{\mathcal{A}} \ . \tag{2.4}$$

$\underset{\sim}{\mathcal{A}}$ operating on a state projects out the state's antisymmetric component in the A-body Hilbert space. In quantum mechanics, observable quantities are represented by Hermitian operators. It is important to note that for identical particles these operators must be symmetric with respect to permutations of the particles. Therefore they must commute with the antisymmetrisation operator.

An A-body Slater determinant is written as an antisymmetric Kronecker product of A one-body states:

$$\big| \, Q \, \big\rangle = \underset{\sim}{\mathcal{A}} \big| \, q_1 \, \big\rangle \otimes \big| \, q_2 \, \big\rangle \otimes \cdots \otimes \big| \, q_{A-1} \, \big\rangle \otimes \big| \, q_A \, \big\rangle . \tag{2.5}$$

The coordinate representation of such a state is:

$$\big\langle \, \vec{x}_1 \, \big| \otimes \big\langle \, \vec{x}_2 \, \big| \otimes \cdots \otimes \big\langle \, \vec{x}_{A-1} \, \big| \otimes \big\langle \, \vec{x}_A \, \big| \, \underset{\sim}{\mathcal{A}} \, \big| \, q_1 \, \big\rangle \otimes \big| \, q_2 \, \big\rangle \otimes \cdots \otimes \big| \, q_{A-1} \, \big\rangle \otimes \big| \, q_A \, \big\rangle \ . \tag{2.6}$$

In FMD, the spatial part of a single-particle wave function is represented by a

Gaussian, hence the last equation can be written as:

$$\begin{aligned}\frac{1}{A!}\sum_{\text{all }\mathcal{P}}^{A!}\operatorname{sgn}(\mathcal{P})\exp\left(-\frac{\left(\vec{x}_1-\vec{b}_{\mathcal{P}(1)}\right)^2}{2a_{\mathcal{P}(1)}}\right)&\left|\,\chi_{\mathcal{P}(1)}\right\rangle\otimes\left|\,\xi_{\mathcal{P}(1)}\right\rangle\\ \otimes\exp\left(-\frac{\left(\vec{x}_2-\vec{b}_{\mathcal{P}(2)}\right)^2}{2a_{\mathcal{P}(2)}}\right)&\left|\,\chi_{\mathcal{P}(2)}\right\rangle\otimes\left|\,\xi_{\mathcal{P}(2)}\right\rangle\\ \otimes\cdots\otimes\exp\left(-\frac{\left(\vec{x}_A-\vec{b}_{\mathcal{P}(A)}\right)^2}{2a_{\mathcal{P}(A)}}\right)&\left|\,\chi_{\mathcal{P}(A)}\right\rangle\otimes\left|\,\xi_{\mathcal{P}(A)}\right\rangle ,\end{aligned}\tag{2.7}$$

where χ and ξ are the spin and isospin components of the single-particle states, respectively. The subscript $\mathcal{P}(i)$ represents all the possible permutations achieved by changing the placement of the i^{th} state in the ordering of the single particle states.

In the form of FMD that is discussed in this work, ξ can only denote a proton or neutron state, there is no mixing of the isospin. The spin is free to take any direction. The complex parameters a and $\vec{b}=\vec{r}+ia\vec{p}$ represent the mean position and momentum of a single particle state [10]:

$$\vec{r}=\frac{\left\langle a,\vec{b}\,\middle|\,\underset{\sim}{\vec{x}}\,\middle|\,a,\vec{b}\right\rangle}{\left\langle a,\vec{b}\,\middle|\,a,\vec{b}\right\rangle}=\frac{a\vec{b}^*+a^*\vec{b}}{a^*+a}\qquad \vec{p}=\frac{\left\langle a,\vec{b}\,\middle|\,\underset{\sim}{\vec{k}}\,\middle|\,a,\vec{b}\right\rangle}{\left\langle a,\vec{b}\,\middle|\,a,\vec{b}\right\rangle}=i\frac{\vec{b}^*-\vec{b}}{a^*+a}\tag{2.8}$$

and the spread in coordinate and momentum space

$$\begin{aligned}(\Delta\vec{r})^2&=\frac{\left\langle a,\vec{b}\,\middle|\left(\underset{\sim}{\vec{x}}-\vec{r}\right)^2\middle|\,a,\vec{b}\right\rangle}{\left\langle a,\vec{b}\,\middle|\,a,\vec{b}\right\rangle}=3\frac{a^*a}{a^*+a}\\ (\Delta\vec{p})^2&=\frac{\left\langle a,\vec{b}\,\middle|\left(\underset{\sim}{\vec{k}}-\vec{p}\right)^2\middle|\,a,\vec{b}\right\rangle}{\left\langle a,\vec{b}\,\middle|\,a,\vec{b}\right\rangle}=3\frac{1}{a^*+a}\ .\end{aligned}\tag{2.9}$$

These are the ingredients that form the non-orthogonal basis used in FMD.

It has been found helpful in representing nuclei with diffuse halos [12] to use a superposition of two Gaussians per single-particle state. This enables one Gaussian to represent the core of the nucleus and the other to represent the diffuse tail of the single-particle density. Equation (2.7) is then written:

$$\frac{1}{A!}\sum_{\text{all }\mathcal{P}}^{A!}\operatorname{sgn}(\mathcal{P})\sum_{i=1}^{2}c_{\mathcal{P}(1)i}\exp\left(-\frac{\left(\vec{x}_1-\vec{b}_{\mathcal{P}(1)i}\right)^2}{2a_{\mathcal{P}(1)i}}\right)\big|\,\chi_{\mathcal{P}(1)i}\,\big\rangle\otimes\big|\,\xi_{\mathcal{P}(1)}\,\big\rangle$$
$$\otimes\cdots\otimes\sum_{i=1}^{2}c_{\mathcal{P}(A)i}\exp\left(-\frac{\left(\vec{x}_A-\vec{b}_{\mathcal{P}(A)i}\right)^2}{2a_{\mathcal{P}(A)i}}\right)\big|\,\chi_{\mathcal{P}(A)i}\,\big\rangle\otimes\big|\,\xi_{\mathcal{P}(A)}\,\big\rangle\,, \tag{2.10}$$

where $c_{\mathcal{P}(k)l}$ gives the strength of the l^{th} Gaussian for the permutations of the k^{th} particle. To describe the most general normalised two component spinor only two real numbers and a phase are needed, however in the FMD code two complex coefficients are stored. This redundancy enables the coefficients $c_{\mathcal{P}(k)l}$ to be absorbed into the $\chi_{\mathcal{P}(k)l}$ and means the complex parameters required to describe each Gaussian are: $a_{\mathcal{P}(k)l}$, $\vec{b}_{\mathcal{P}(k)l}$, $\chi^{\uparrow}_{\mathcal{P}(k)l}$ and $\chi^{\downarrow}_{\mathcal{P}(k)l}$.

2.1.1. Ritz variational principle

According to the Ritz variational principle [40], the expectation value of the energy of any trial state $\big|\,\phi\,\big\rangle$ will always be greater than or equal to the energy of the lowest eigenvalue of the Hamiltonian E_0:

$$\frac{\big\langle\,\phi\,\big|\,\underset{\sim}{H}\,\big|\,\phi\,\big\rangle}{\big\langle\,\phi\,\big|\,\phi\,\big\rangle}=E'\geq E_0\,. \tag{2.11}$$

Therefore, minimising the expectation value of the Hamiltonian by varying the parameters of a trial state provides a method to find an upper bound for the true ground state energy of a nucleus and to approximate its structure. Improving the model space by using an initial trial state that is closer to the true ground state, or by using a superposition of trial states, delivers a better approximation of the true structure of the nucleus in question.

2.1.2. Projection formalism

Using the formalism explained in section 2.1 it is possible to calculate observables. For example, calculating:

$$\frac{\big\langle\,Q\,\big|\,\underset{\sim}{H}-\underset{\sim}{T}_{\text{CM}}\,\big|\,Q\,\big\rangle}{\big\langle\,Q\,\big|\,Q\,\big\rangle}\,, \tag{2.12}$$

with the definition of the Slater determinant $\big| \, Q \, \big\rangle$ given in equation (2.5), gives the expectation value of the energy of the A-body state with its centre of mass kinetic energy removed. To get a first approximation to the ground state of the nucleus, the value of (2.12) is minimised by varying the single-particle parameters of all Gaussians [29]:

$$q_\alpha = \{a_\alpha, \vec{b}_\alpha, \chi^{\uparrow}_\alpha, \chi^{\downarrow}_\alpha\} \qquad \underset{\{q_\alpha\}}{min} \frac{\big\langle \, Q \, \big| \, \underset{\sim}{H} - \underset{\sim}{T}_{\mathrm{CM}} \, \big| \, Q \, \big\rangle}{\big\langle \, Q \, \big| \, Q \, \big\rangle} \; , \tag{2.13}$$

in accordance with the Ritz variational principle described in section 2.1.1.

In experiment, nuclei are found to be in states that possess a definite angular momentum and parity. In terms of a theoretical description this means that the nuclear Hamiltonian that is used must commute with parity operations and rotations. This in turn means that its eigenstates are also the eigenstates of the parity operator $\underset{\sim}{\Pi}$, total angular momentum squared $\underset{\sim}{\vec{J}}^2$ and one of its components, which by convention is chosen to be $\underset{\sim}{J}_z$. In the absence of significant external fields the eigenstates separate the centre of mass motion from the intrinsic motion of the nucleons. Therefore the eigenstates can be chosen to be invariant with respect to translations in space, which requires them to be eigenstates of the centre of mass linear momentum operator $\underset{\sim}{\vec{K}}_{\mathrm{CM}}$.

In general the FMD many-body state (2.5) does not possess these symmetries [10]. Therefore appropriate projections are performed on the FMD states so that the eigenstates of the Hamiltonian exhibit the required symmetries [11].

Centre of mass projection

The centre of mass motion of a nucleus should be separated from its internal motion. If the Gaussians all have the same width parameter a, as is the case for example in Antisymmetric Molecular Dynamics (AMD) [23], then the relative motion and centre of mass motion can be factored out (see section 2.3.4). However, the possibility for the single-particles states to have different widths is an important degree of freedom in the nuclear many-body problem. Therefore in FMD a projection on the momentum zero eigenstate of total momentum $\underset{\sim}{\vec{K}}_{\mathrm{CM}} = \sum_{i=1}^{A} \underset{\sim}{\vec{k}}(i)$ is normally performed, which causes the state to become translationally invariant. This is done using the following operator:

$$\underset{\sim}{P}_{\mathrm{CM}} = \frac{1}{(2\pi)^3} \int d^3X \, \exp\left\{ -i \, \underset{\sim}{\vec{K}}_{\mathrm{CM}} \vec{X} \right\} = \delta^3 \left(\underset{\sim}{\vec{K}}_{\mathrm{CM}} \right) \; . \tag{2.14}$$

This projects the state onto a centre of mass momentum of zero. The quality of the projection can be ascertained by checking the expectation value of the centre of mass kinetic energy, which should be zero.

Parity projection

The Hamiltonian also has mirror symmetry and therefore the states need to be projected on parity. The projection on positive or negative parity is performed using the following operator:

$$\underset{\sim}{P}^{\pi} = \frac{1}{2}\left(\underset{\sim}{1} + \pi\underset{\sim}{\Pi}\right) \qquad \pi = \pm 1 \tag{2.15}$$

where $\underset{\sim}{1}$ is the identity and $\underset{\sim}{\Pi}$ is the parity operator.

Angular momentum projection

To restore the rotational invariance of the Hamiltonian, the states are projected onto the eigenstates of the total angular momentum operator $\vec{\underset{\sim}{J}}^{2}$, by using the following operator [34]:

$$\underset{\sim}{P}^{J}_{MK} = \frac{2J+1}{8\pi^2}\int d\alpha\,\sin\beta\,d\beta\,d\gamma\; D^{J\,*}_{MK}(\alpha,\beta,\gamma)\;\underset{\sim}{R}(\alpha,\beta,\gamma) \tag{2.16}$$

in which α, β and γ are the Euler angles. The rotation operator $\underset{\sim}{R}$ is given by ([49], sec. 1.4.5):

$$\underset{\sim}{R}(\alpha,\beta,\gamma) = \exp\left\{-\,i\alpha\underset{\sim}{J}_z\right\}\exp\left\{-\,i\beta\underset{\sim}{J}_y\right\}\exp\left\{-\,i\gamma\underset{\sim}{J}_z\right\} \tag{2.17}$$

and the Wigner D-functions D^{J}_{MK} are defined as:

$$D^{J}_{MK}(\alpha,\beta,\gamma) = \left\langle\, JM \,\middle|\, \underset{\sim}{R}(\alpha,\beta,\gamma) \,\middle|\, JK \,\right\rangle = e^{-iM\alpha}\; d^{J}_{MK}(\beta)\; e^{-iK\gamma}\;, \tag{2.18}$$

where $d^{J}_{MK}(\beta) = \left\langle\, JM \,\middle|\, \exp\left\{-\,i\beta\underset{\sim}{J}_y\right\} \,\middle|\, JK \,\right\rangle$, these coefficients are given in explicit forms in ([49], sec. 4.3).

Strictly speaking, $\underset{\sim}{P}^{J}_{MK}$ is not a projector, but it has the property:

$$\left(\underset{\sim}{P}^{J}_{MK}\right)^{\dagger}\underset{\sim}{P}^{J'}_{M'K'} = \delta_{JJ'}\,\delta_{MM'}\;\underset{\sim}{P}^{J}_{KK'}\;. \tag{2.19}$$

States projected on total angular momentum are denoted by:

$$\left|\, Q; JMK \,\right\rangle := \underset{\sim}{P}^{J}_{MK}\left|\, Q \,\right\rangle\;. \tag{2.20}$$

The expectation value of $\vec{\underset{\sim}{J}}^{2}$ with respect to the projected states is calculated and is used as a check on the quality of the angular momentum projection.

The result of all these projections acting together on a Slater determinant is a projected state, which is denoted by:

$$\big|\, Q; J^\pi M K \,\big\rangle := \underset{\sim}{P}^{J^\pi}_{MK}\, \underset{\sim}{P}_{\mathrm{CM}} \big|\, Q \,\big\rangle = \underset{\sim}{P}^{J}_{MK}\, \underset{\sim}{P}^{\pi}\, \underset{\sim}{P}_{\mathrm{CM}} \big|\, Q \,\big\rangle \; . \tag{2.21}$$

M and K can take the $2J+1$ values from $-J$ to $+J$, however, in general not all of these states are linearly independent. For example, in the case of axial symmetry there is only one linearly independent state and one may choose $K = J$.

Scalar operators such as the Hamiltonian commute with any rotation operator. Thus (2.19) allows a large reduction in the computational effort required to calculate the matrix elements of scalar operators, as the projection operator only needs to operate on the ket [29]:

$$\begin{aligned}
&\big\langle\, Q; JMK \,\big|\, \underset{\sim}{H} \,\big|\, Q; JM'K' \,\big\rangle \\
&= \big\langle\, Q \,\big| \left(\underset{\sim}{P}^{J}_{MK}\right)^{\dagger} \underset{\sim}{H}\, \underset{\sim}{P}^{J}_{M'K'} \big|\, Q \,\big\rangle \; = \big\langle\, Q \,\big|\, \underset{\sim}{H}\, \underset{\sim}{P}^{J}_{KK'} \big|\, Q \,\big\rangle \, \delta_{MM'} \\
&= \frac{2J+1}{8\pi^2} \int d\alpha \, \sin\beta \, d\beta \, d\gamma \; D^{J\;*}_{KK'}(\alpha,\beta,\gamma) \, \big\langle\, Q \,\big|\, \underset{\sim}{H}\, \underset{\sim}{R}(\alpha,\beta,\gamma) \,\big|\, Q \,\big\rangle \; ,
\end{aligned} \tag{2.22}$$

as the Hamiltonian matrix elements require by far the most computing time this is a big advantage.

As the Hamiltonian also commutes with the operators that project the states on parity and a centre of mass momentum of zero, the matrix elements of the Hamiltonian for a single Slater determinant can be calculated as:

$$\mathsf{H}_{KK'} = \big\langle\, Q \,\big|\, \underset{\sim}{H}\, \underset{\sim}{P}^{J^\pi}_{KK'} \underset{\sim}{P}_{\mathrm{CM}} \big|\, Q \,\big\rangle \tag{2.23}$$

where $\underset{\sim}{P}^{J^\pi}_{KK'} = \underset{\sim}{P}^{\pi} \underset{\sim}{P}^{J}_{KK'}$.

To optimise the quality of the projection for a given number of angles, the eigenvalues of the inertia tensor are calculated so as to determine its principal axes. The inertia tensor is given by:

$$\begin{aligned}
I_{ij} &= \mathrm{Tr}(\theta)\delta_{ij} - \theta_{ij} \; ; \qquad & \theta_{ij} &= \int d^3r \; \rho(\vec{r}) x_i x_j \qquad & i,j &= 1,2,3 \\
x_l &= x'_l - X_{\mathrm{CM},l} \; ; \qquad & X_{\mathrm{CM},l} &= \frac{\int d^3r' \rho(\vec{r}\,') x'_l}{\int d^3r' \rho(\vec{r}\,')} \qquad & l &= 1,2,3 \; .
\end{aligned} \tag{2.24}$$

The system is then oriented so that the eigenvalue that is most different from the other two points along the z-axis. This does not make such a great improvement to the quality of the projection for largely deformed triaxial shapes, but for a shape that is nearly a prolate or oblate spheroid (nearly axially symmetric) this ensures that rotations around the z-axis will have a large overlap with one another (and therefore require less angles for the integration) and rotations around the y-axis will have a smaller overlap with one another (hence requiring more angles).

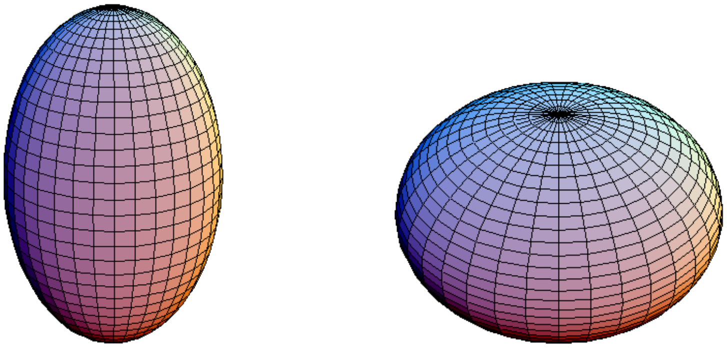

Figure 2.1.: A prolate spheroid (left) and oblate spheroid (right).

A graphical depiction of an oblate and prolate spheroid is shown in figure 2.1. Consequently, the normal parameters that are used in the angular momentum projection correspond to an integration over ten angles in α, twenty in β and ten in γ. The integration points are chosen on a regular grid for the angles α and γ and according to a Gauss-Legendre, or if the matrix elements fall off very quickly, a Gauss-exponential integration for β [29].

If the system has spherical symmetry, then the state is the same no matter how it is rotated and therefore only $J = K = M = 0$ gives a non-zero result, so no integration is required.

If the system has axial symmetry and is therefore an eigenstate of $\underset{\sim}{J}_z$ then rotating the state around the z-axis does not yield a new state. Hence the sum over K' in (2.23) is not required and $K = K' = J$ can be chosen. This means that only an integration over the angle β must be performed. Using the aforementioned parameters for the number of angles, this leads to a hundredfold reduction in the computing time required. This fact is exploited in the calculation of frozen states (see section 2.3.1). In all the reactions chosen for study so far the frozen states have been axially symmetric to take advantage of this big reduction in the computational effort required and hence make the problem tractable within an acceptable timescale.

K-mixing

The eigenvalue equation for the Hamiltonian written in matrix form is:

$$\sum_{K'=-J}^{J} \mathsf{H}_{KK'} \cdot C^{\kappa}_{K'} = E_{\kappa} \sum_{K'=-J}^{J} \mathsf{N}_{KK'} \cdot C^{\kappa}_{K'} \ , \tag{2.25}$$

this is a generalised eigenvalue problem as it involves an overlap matrix $\mathsf{N}_{KK'}$ which is required by the non-orthogonality of the FMD basis states. This can be transformed into a normal eigenvalue problem by inverting the overlap matrix and applying it to the left of (2.25). However, if the set of states $\left| Q; J^\pi MK \right\rangle$ contains members that are linearly or almost linearly dependent then numerically singular values will render the inversion unstable. This can be avoided if a singular value decomposition is used to rewrite the overlap matrix. Eigenstates of the overlap matrix for which the eigenvalue is numerically zero, or below a certain fraction of the largest eigenvalue, can then be easily found and excluded before the inversion is performed.

Decomposing the overlap matrix as:

$$\mathsf{N}_{KK'} = \sum_{i=1}^{2J+1} \mathsf{U}_{Ki} \cdot \sigma_i \cdot \left(\mathsf{V}^\dagger\right)_{iK'} \qquad K, K' = -J, -J+1, \ldots, J \ , \tag{2.26}$$

where U and V are unitary matrices containing the singular vectors of N, and σ contains the singular values of the overlap matrix. States with singular values smaller than a given relative threshold η can then be discarded as being linearly dependent:

$$\frac{\sigma_i}{\max_{i'} \left\{\sigma_{i'};\ i' = 1, \ldots, 2J+1\right\}} > \eta \qquad i = 1, \ldots, 2J+1 \ . \tag{2.27}$$

From this restriction, a space spanned by a number of orthogonal states t is defined.

Inserting equation (2.26) into (2.25) gives:

$$\sum_{K'=-J}^{J} \mathsf{H}_{KK'} \cdot C^\kappa_{K'} = E_\kappa \sum_{i=1}^{2J+1} \sum_{K'=-J}^{J} \mathsf{U}_{Ki} \cdot \sigma_i \cdot \left(\mathsf{V}^\dagger\right)_{iK'} \cdot C^\kappa_{K'} \ . \tag{2.28}$$

By multiplying from the left with $\mathsf{U}^\dagger$ and then dividing by σ_i, this equation can be rewritten as:

$$\sum_{K,K'=-J}^{J} \frac{1}{\sigma_i} \left(\mathsf{U}^\dagger\right)_{iK} \cdot \mathsf{H}_{KK'} \cdot C^\kappa_{K'} = E_\kappa \ \psi^\kappa_i \qquad i, \kappa = 1, \ldots, t \ . \tag{2.29}$$

where $\psi^\kappa_i = \sum_{K'=-J}^{J} \left(V^\dagger\right)_{iK'} \cdot C^\kappa_{K'}$ and the unitarity of U has been exploited. Also, note that the index i now only runs from 1 to $t \leq 2J+1$ to avoid division by any of the σ_i that are numerically equal to zero. Inserting the identity

$\sum_{l=1}^{2J+1} \mathsf{V}_{K'l} \left(\mathsf{V}^\dagger\right)_{lK''}$ gives:

$$
\begin{aligned}
\sum_{K,K',K''=-J}^{J} \sum_{l=1}^{2J+1} \frac{1}{\sigma_i} \left(\mathsf{U}^\dagger\right)_{iK} \cdot \mathsf{H}_{KK'} \cdot \mathsf{V}_{K'l} \cdot \left(\mathsf{V}^\dagger\right)_{lK''} \cdot C^\kappa_{K''} &= E_\kappa \, \psi^\kappa_i \\
\sum_{K,K'=-J}^{J} \sum_{l=1}^{2J+1} \frac{1}{\sigma_i} \left(\mathsf{U}^\dagger\right)_{iK} \cdot \mathsf{H}_{KK'} \cdot \mathsf{V}_{K'l} \cdot \psi^\kappa_l &= E_\kappa \, \psi^\kappa_i \\
& \qquad i,\kappa = 1,\ldots,t \; .
\end{aligned}
\tag{2.30}
$$

The coefficients of the eigenvectors of the Hamiltonian ψ^κ_i found by this method can then each be written in the original n-dimensional space using:

$$
C^\kappa_K = \sum_{i=1}^{t} \left(\mathsf{V}^\dagger\right)_{Ki} \psi^\kappa_i \qquad K = -J,\ldots,J \tag{2.31}
$$

Thus the eigenvalue problem has been solved in a more numerically reliable way by first removing linear dependencies.

The other requirement for the continued use of each of these orthogonal states in the calculation is that they have sufficient overlap with the unprojected state $\left|\, Q \,\right\rangle$:

$$
\frac{\left\langle\, Q \,\middle|\, Q; J^\pi M; \kappa \,\right\rangle}{\sqrt{\left\langle\, Q \,\middle|\, Q \,\right\rangle \left\langle\, Q; J^\pi M; \kappa \,\middle|\, Q; J^\pi M; \kappa \,\right\rangle}} > \epsilon \qquad \kappa = 1,\ldots,n \qquad n \leq t \; , \tag{2.32}
$$

this removes from the model space states that are just due to numerical noise. This gives a final dimension of n for the space spanned by the projected states $\left|\, Q; J^\pi M; \kappa \,\right\rangle$ out of the original $2J+1$ states.

To summarise, this process mixes the different K values to produce a set of $n \leq 2J+1$ projected basis states

$$
\left|\, Q; J^\pi M; \kappa \,\right\rangle \tag{2.33}
$$

that are linearly independent, whilst also removing from the model space states that are just due to numerical noise.

2.1.3. Minimisation schemes

As already shown at the beginning of the last section, a Hartree-Fock approximation to the nuclear many-body problem can be obtained from (2.13). This is only an approximation as the variational manifold is restricted to the parameters of the FMD states, rather than the most general single particle state. The minimisation is performed on unprojected states, which can later be projected if so desired. However, it is possible to get a better representation of a nuclear state by performing minimisation after projection on certain symmetries. This can be understood in terms of increasing the size of the model space. By a parity projection, a superposition of two configurations is available rather than a single one; by angular momentum projection, a superposition of a much larger number of configurations can be varied. However these extra configurations must also be calculated, so the improvement in model space must be paid for in computing time. The three schemes of minimisation commonly used in FMD are:

- Hartree-Fock approximation: the parameters of a Slater determinant are varied so as to minimise the energy of the ground state, as shown in equation (2.13).

- Minimisation of a parity projected state: a parity projected state is calculated and then its parameters are varied, so that the energy of a parity projected trial state:

  $$\frac{\langle\, Q \,|\, \underset{\sim}{H} \left(\underset{\sim}{1} + \pi \underset{\sim}{\Pi}\right) |\, Q \,\rangle}{\langle\, Q \,|\, \underset{\sim}{1} + \pi \underset{\sim}{\Pi} \,|\, Q \,\rangle} \qquad \pi = \pm 1 \tag{2.34}$$

  is minimised. The result of the minimisation is then projected on angular momentum, parity and centre of mass momentum of zero, therefore this is known as 'projection after variation of a parity eigenstate' or PAV$^{\pi}$ for short.

- Minimisation of an angular momentum and parity projected state: this is by far the most time consuming of the minimisation schemes as it minimises:

  $$\frac{\langle\, Q \,|\, \underset{\sim}{H} \underset{\sim}{P}^{J\pi}_{KK} \,|\, Q \,\rangle}{\langle\, Q \,|\, \underset{\sim}{P}^{J\pi}_{KK} \,|\, Q \,\rangle} \tag{2.35}$$

  and therefore requires a full angular momentum projection and parity projection to be performed before each minimisation step. This is known as 'variation after angular momentum and parity projection', or VAP for short. As the calculation is so time consuming, VAP calculations are only feasible for light nuclei. The value of K in (2.35) is chosen as the one with the largest K-mixing component. The final result of the minimisation is again projected on angular momentum, parity and a centre of mass momentum of zero.

2.1.4. Multiconfiguration mixing

So far only a single Slater determinant has been discussed. However, in situations where the multidimensional energy surface described by the variation of the parameter set is relatively flat; more than one set of parameter values give a similar energy. This implies that more than one of the states in the chosen model space has a sizeable contribution to the ground state configuration. Hence a superposition of the basis states, which are now therefore numbered with an index a: $\left| Q^{(a)}; J^\pi M K \right\rangle$, will describe the ground state better than any one of them alone. The process of discovering the optimal weightings to apply to each basis state so as to minimise the ground state energy is known as multiconfiguration mixing [22]. Special examples of this are the superposition of all translations and all rotations, which when combined with the relevant coefficients, are just the centre of mass and angular momentum projections described in section 2.1.2.

Each of the K-mixed basis states from equation (2.33) is denoted in the following way:

$$\begin{aligned} \left| Q^{(a)}; J^\pi M; \kappa_a \right\rangle = \sum_{K=-J}^{J} \left| Q^{(a)}; J^\pi M K \right\rangle C_K^{(a,\kappa_a)} \\ a = 1,\ldots,n\,; \quad \kappa_a = 1,\ldots,n^{(a)}\,, \end{aligned} \tag{2.36}$$

where n is the number of Slater determinants included in the model space. Matrix elements of the Hamiltonian and overlap matrix can be written in the original non-orthogonal basis as:

$$\begin{aligned} \mathsf{H}_{(a,\kappa_a),(b,\kappa_b)} &= \sum_{K,K'=-J}^{J} C_K^{(a,\kappa_a)*} \left\langle Q^{(a)} \right| \underset{\sim}{H} \underset{\sim}{P}{}^{J^\pi}_{KK'} \underset{\sim}{P}_{\mathrm{CM}} \left| Q^{(b)} \right\rangle C_{K'}^{(b,\kappa_b)} \\ \mathsf{N}_{(a,\kappa_a),(b,\kappa_b)} &= \sum_{K,K'=-J}^{J} C_K^{(a,\kappa_a)*} \left\langle Q^{(a)} \right| \underset{\sim}{P}{}^{J^\pi}_{KK'} \underset{\sim}{P}_{\mathrm{CM}} \left| Q^{(b)} \right\rangle C_{K'}^{(b,\kappa_b)}\,. \end{aligned} \tag{2.37}$$

Using an abbreviated notation, where $i = (a, \kappa_a)$ and $j = (b, \kappa_b)$, these matrix elements can be written in the new basis as:

$$\begin{aligned} \mathsf{H}_{ij} &= \left\langle Q^{(a)}; J^\pi M; \kappa_a \right| \underset{\sim}{H} \left| Q^{(b)}; J^\pi M; \kappa_b \right\rangle \\ \mathsf{N}_{ij} &= \left\langle Q^{(a)}; J^\pi M; \kappa_a \middle| Q^{(b)}; J^\pi M; \kappa_b \right\rangle\,. \end{aligned} \tag{2.38}$$

The Hamiltonian can then be diagonalised in a model space composed of n of these sets of K-mixed states:

$$\begin{aligned} \underset{\sim}{H}\big|\, J^\pi M; \alpha \,\big\rangle &= E_\alpha \big|\, J^\pi M; \alpha \,\big\rangle \\ \big|\, J^\pi M; \alpha \,\big\rangle &= \sum_{a=1}^{n} \sum_{\kappa_a=1}^{n^{(a)}} \Psi^\alpha_{(a,\kappa_a)} \sum_{K=-J}^{J} \big|\, Q^{(a)}; J^\pi M K \,\big\rangle C_K^{(a,\kappa_a)} \;, \end{aligned} \tag{2.39}$$

where α numbers the eigenstates of the Hamiltonian for a particular J^π.

2.2. Interaction and $\mathrm{V}_{\mathrm{UCOM}}$

The interaction used throughout this work is based on the AV18 interaction [51], which is a realistic two-body interaction. Realistic in this context means that it is able to reproduce the deuteron properties and the experimental nucleon-nucleon (NN) phase shifts up to around 300 MeV. The form of the potential is determined from the NN phase shifts via the inverse scattering problem. This has no unique solution if the interaction is allowed to be non-local (have momentum dependence) as is the case for realistic interactions. This can also be seen from another point of view: the particles are observed asymptotically, therefore interactions generated in this way are only certain to have the same on-shell (asymptotic) properties, as the phase shifts are determined at infinite relative distance. This leaves an infinite amount of freedom for them to exhibit different off-shell behaviour and hence an infinite number of realistic interactions can be constructed, all of which reproduce the NN scattering phase shifts.

The NN interaction induces strong short-range correlations. The main contributions to these correlations arise from: a strong repulsion at interparticle distances $\lesssim 0.6$ fm (known as central or radial correlations) and short-range tensor correlations which are dependent on the orientation of the spins of the nucleons with respect to their spatial orientation. The effects of these correlations can even be seen in the ground state of the deuteron, where the two-body probability density of finding two nucleons at very small relative distances is greatly diminished due to the repulsive nature of the short-range part of the interaction, and the generation of a D-wave admixture in the deuteron wave function is caused by the tensor force [36].

The Gaussian wave packets in FMD are not able to represent such correlations. Even a superposition of a feasible number of Slater determinants is unable to include these correlations. Therefore the use of the bare AV18 interaction with the FMD basis states would be doomed to failure.

The problem is to find a way to imprint these correlations onto the FMD states, however this should be achieved in such a way that it does not compromise the realistic nature of the interaction; in other words the interaction should still deliver the correct properties of the deuteron and NN phase shifts.

One approach to tackling this problem is the Unitary Correlation Operator Method (UCOM) [13]. This achieves exactly the requirements listed in the last paragraph. As its name suggests, it consists of making unitary transformations to include the required short range correlations. The two types of correlations are imprinted by means of two unitary correlators: $\underset{\sim}{C}_r$ for the radial correlations and $\underset{\sim}{C}_\Omega$ for the tensor correlations. By virtue of the unitarity of the correlators, we are free to choose whether to apply them to the operators or to the states when calculating matrix elements:

$$\left\langle\, Q \,\middle|\, \underset{\sim}{C}_r^\dagger \, \underset{\sim}{C}_\Omega^\dagger \, \underset{\sim}{A} \, \underset{\sim}{C}_\Omega \, \underset{\sim}{C}_r \,\middle|\, Q' \,\right\rangle = \left\langle\, Q \,\middle|\, \underset{\sim}{C}_r^{-1} \, \underset{\sim}{C}_\Omega^{-1} \, \underset{\sim}{A} \, \underset{\sim}{C}_\Omega \, \underset{\sim}{C}_r \,\middle|\, Q' \,\right\rangle . \tag{2.40}$$

The advantage of applying the correlators to the operators is that the interaction then remains basis independent, therefore this is the method usually employed; for some examples of the use of the UCOM with different basis states see [39]. The fact that the transformations are unitary means that the eigenvalues of operators such as the Hamiltonian are unchanged. The correlators induce short-range correlations and therefore they have a finite range, as the nuclear phase shift is determined asymptotically the correlators have no effect on it. Hence the correlated interaction is phase shift equivalent to the bare interaction. These two facts together mean that the correlated interaction is also a realistic interaction.

The correlators are defined by:

$$\underset{\sim}{C}_r = \exp\left(-i \sum_{\substack{i=1 \\ i<j}}^{A} \underset{\sim}{g}_{rij} \right) \qquad \underset{\sim}{C}_\Omega = \exp\left(-i \sum_{\substack{i=1 \\ i<j}}^{A} \underset{\sim}{g}_{\Omega ij} \right) \tag{2.41}$$

where A is the total particle number and $\underset{\sim}{g}_{rij}$ and $\underset{\sim}{g}_{\Omega ij}$ are the hermitian generators of the radial and tensor correlations, respectively. For more details on the exact form of the radial generator see [13] and for the tensor generator see [28] and [38].

In figure 2.2 the effect of the correlators on the two-body density for the deuteron in the $M_S = 0$ and $M_S = \pm 1$ channel can be seen in a three dimensional density plot. In both cases it can be seen that the two-body density at low interparticle distances is suppressed by the radial correlations. The tensor correlations manifest themselves in the tendency of nucleons with parallel spins to align themselves parallel to the relative distance vector between them, hence the dumbbell structure in the right hand side of the figure where $M_S = \pm 1$ showing increased density at the poles; and of nucleons with antiparallel spins to align themselves perpendicular to the relative distance vector between them, leading to the donut structure with increased density distributed about the equator.

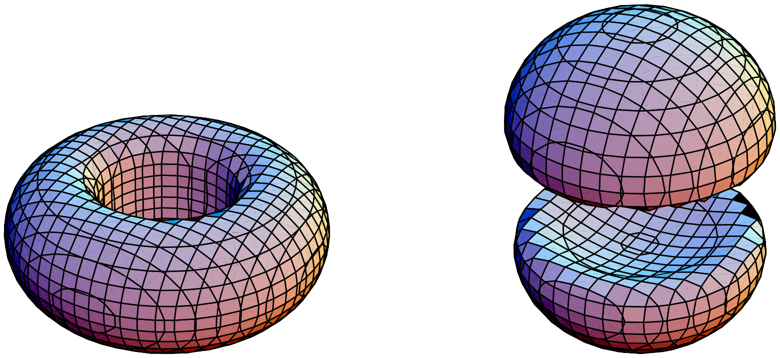

Figure 2.2.: Surfaces of constant two-body density for the deuteron in the $M_S = 0$ channel (left) and the $M_S = \pm 1$ channel (right), taken from [28].

Another way of viewing these short-range correlations is that short-range corresponds to high momenta, due to the increased curvature in the wave function at short-range. When the bare AV18 interaction is used on the simple FMD states, the operators' matrix elements in momentum representation have a highly non-diagonal structure corresponding to a strong connection between low momentum and high momentum states. By the application of the correlation operators, the off-diagonal matrix elements are suppressed due to the unitary transformations and hence they assume a band diagonal structure. This corresponds to a prediagonalisation of the model space which decouples the low momentum states from the high momentum ones. For shell model calculations this allows convergence with a lower number of oscillator shells, for FMD calculations it means that the nuclear many-body problem is easier to describe in terms of Slater determinants and hence the model space can be smaller [36].

The correlators are observed to have the correct effects, but the appropriate strength for these effects must still be determined. In the generator $\underset{\sim}{g}_{\Omega ij}$ there is still one free parameter: the range of the correlator. This range can be varied which causes alterations to the calculated binding energy of nuclei. As the aim is to calculate the properties of many-body systems whilst using only a two-body interaction, it makes sense to somehow try to include the effects of three- and higher-body forces. This is achieved in a somewhat phenomenological way by adjusting the range of the tensor correlator such that the binding energy of ^{4}He and ^{3}H are reproduced. When the range of the tensor correlator is varied the results fall in a straight line as can be seen in figure 2.3. This line coincides with the so-called Tjon line [31] which displays the correlations between the ^{4}He and ^{3}H for different realistic forces.

In the FMD model space the correlations induced by the residual medium to long-range tensor force are not properly described, this is partially corrected for by increasing the range of the tensor correlator compared to the 'pure' $\mathrm{V_{UCOM}}$. How-

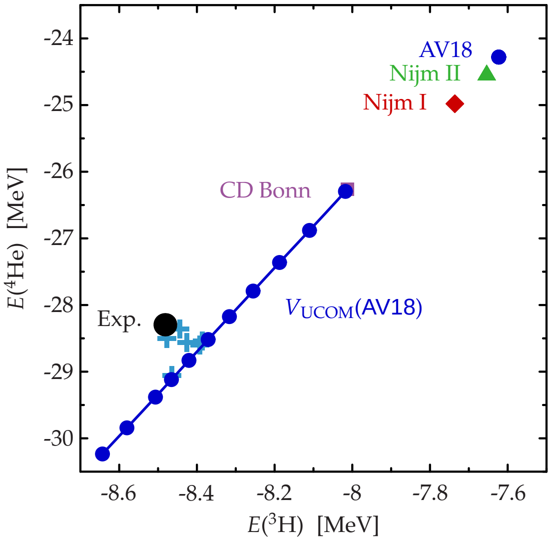

Figure 2.3.: Binding energies of ^{4}He plotted against those of ^{3}H for different realistic potentials. The points marked AV18, Nijm II, Nijm I and CD Bonn are the results of exact Faddeev calculations obtained by A. Nogga *et al.* [31] using these different realistic two body interactions. The blue crosses show results obtained by the same method but using simple three-body forces in addition to the aforementioned realistic two-body interactions. The blue circles are converged no-core shell model results for the AV18 potential correlated using V_{UCOM} with different values for the range of the tensor correlator, decreasing the range moves up the line [37].

ever, as there are no three-body forces included in the interaction, the saturation of the nuclear force is incorrect. This is presently corrected for by introducing a phenomenological two-body correction term with a momentum dependent central and isospin dependent spin-orbit component [30]. The parameters of this correction term are fitted to the binding energies and radii of the doubly-magic nuclei ^{4}He, ^{16}O, ^{40}Ca, ^{24}O, ^{34}Si and ^{48}Ca, additional spin orbit strength is also required to fit these nuclei well. The total contribution from this correction amounts to about 15% of the 'pure' V_{UCOM} potential. In the future, the aim is to replace this phenomenological correction term with a three-body or density dependent two-body force. This gives an effective interaction, which is however closely related to the correlated realistic AV18 interaction, that can then be used with the simple FMD many-body states.

2.3. Applying FMD to scattering reactions

2.3.1. Formation of an FMD Hilbert space

To describe scattering states, a Hilbert space that can represent both the cluster structure at large distances and the compound nucleus is required. The great advantage of using FMD, is that both of these parts of the Hilbert space can be treated completely consistently because the Gaussian basis states are versatile enough to describe shell model, deformed and cluster states. The same interaction and Hilbert space are used throughout the procedure, making it a truly unified approach to describing scattering.

Frozen states

When the clusters are far apart, there is no significant overlap between their wave functions, therefore their intrinsic degrees of freedom are effectively frozen and only the relative motion between the clusters is important. Consequently, the states that span this part of the Hilbert space are referred to as frozen states. As was mentioned earlier (section 2.1.2), the only systems which are considered in this work are those in which at most one of the clusters has an intrinsic spin. If one of the clusters does have a spin, then its orientation can be chosen, with no loss of generality, to lie along the axis connecting the clusters. The frozen states are just the minimised, intrinsic state of one cluster, times that of the other cluster. This means that the frozen states that are used for any reactions considered in this thesis are axially symmetric. To form these states the clusters are placed on a grid at different separations, usually with a spacing of around 1 fm, an irregular grid could also be used but this has not been employed so far. It is simple to form the frozen states as the Gaussians can easily be shifted in coordinate and momentum space:

$$\begin{aligned}\left\langle\, \vec{x} \,\middle|\, \exp\left(-i\underset{\sim}{\vec{k}}\vec{d}\right) \,\middle|\, q \,\right\rangle &= \exp\left(-\vec{d}\,\frac{\partial}{\partial\vec{x}}\right)\exp\left(-\frac{\left(\vec{x}-\vec{b}\right)^2}{2a}\right)\left|\,\chi\,\right\rangle\otimes\left|\,\xi\,\right\rangle \\ &= \exp\left(-\frac{\left(\vec{x}-\vec{b}-\vec{d}\right)^2}{2a}\right)\left|\,\chi\,\right\rangle\otimes\left|\,\xi\,\right\rangle \\ &= \left|\,a,\vec{b}+\vec{d}\,\right\rangle\otimes\left|\,\chi\,\right\rangle\otimes\left|\,\xi\,\right\rangle\,. \end{aligned} \tag{2.42}$$

The shift vector $\vec{d}$ is real and thus corresponds to a shift of the Gaussian's centroid by $\vec{d}$. Hence the clusters can easily be placed at various relative distances. This is

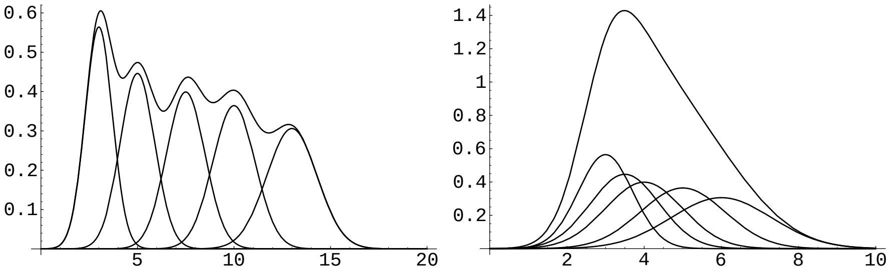

Figure 2.4.: Left: the Gaussians forming the basis are too widely spaced and bumps appear in the relative wave function. Right: the same Gaussians are used (note scale) but placed closer together, the relative wave function is now smooth.

in the spirit of the generator coordinate method (GCM) [19][21], with the relative distance between the clusters being the generator coordinate.

What now needs to be decided is the appropriate spacing between these frozen states. Positioning the frozen states too close to one another means that the basis is too dense and numerical problems can ensue due to linear dependencies. If the frozen states are positioned too far apart, the relative wave function will have holes in it. This will cause spurious bumps to appear in it, as shown in figure 2.4. To find an appropriate spacing for the frozen states Alberto Cribeiro investigated a schematic model [7]. In the case where the Gaussian widths were all equal, his findings were that the optimal spacing between frozen states Δ is given by:

$$\Delta = \sqrt{\frac{a}{1.1\ \mu_{\mathrm{A}}}} \qquad \mu_{\mathrm{A}} = \frac{A_1 A_2}{A}\ , \tag{2.43}$$

where a is the Gaussian width and A, A_1 and A_2 are the total particle number, that of cluster one and that of cluster two, respectively. In the many-body Hilbert space with different widths for each Gaussian an average of the Gaussian widths must be taken. The formula above can then be used as a first estimate for the optimal spacing.

Once a value for Δ is chosen it is easy to form the states with the required relative distance between them, as explained above. An example of some of these configurations for ^{3}He and ^{4}He is shown in the single-particle density plots in figure 2.5.

Adiabatic states

As explained in the last subsection, the clusters that form the frozen states are themselves minimised but the two cluster state as a whole is not. This explains the increase in energy shown in figure 2.6 at separations where the clusters overlap

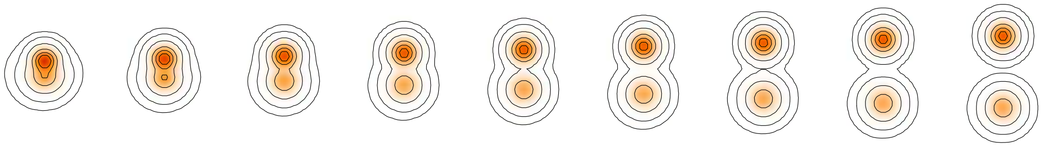

Figure 2.5.: Single particle density for ^{3}He and ^{4}He clusters posisitioned at relative distances from 1 to 9 fm in steps of 1 fm, the energies of these states are shown in figure 2.6.

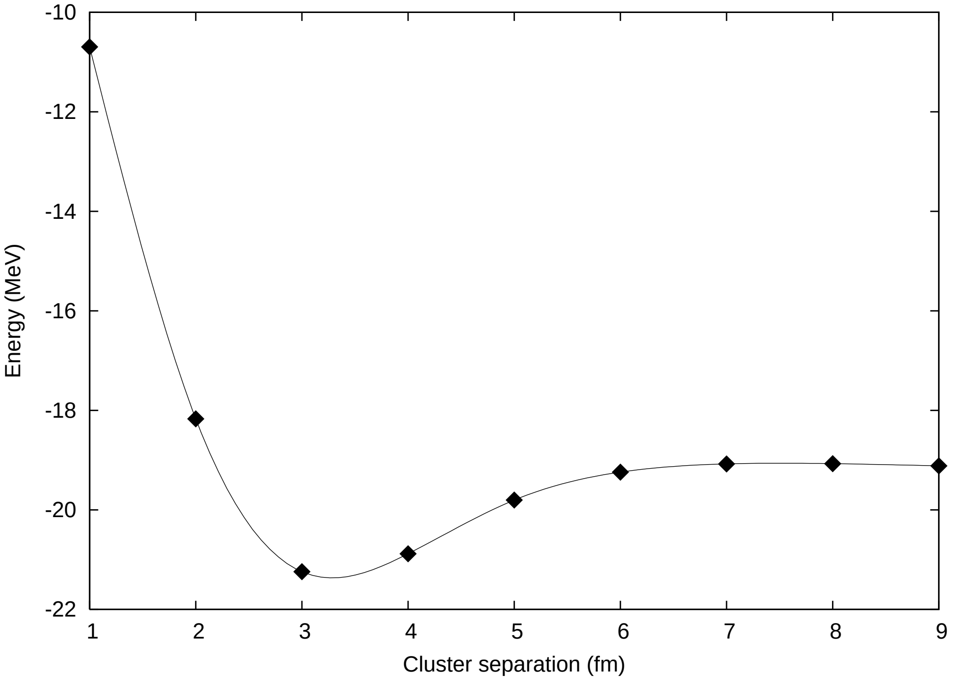

Figure 2.6.: The unprojected energies of the cluster states shown in figure 2.5 at relative distances from 1 to 9 fm. The line is just to guide the eye.

appreciably. The frozen states at small relative distances are in general not sufficient to accurately describe the compound nucleus, see for example section 4.1. A good starting point to improve the model space is to add to this Hilbert space of frozen states configurations that better represent the ground state of the compound nucleus. This then includes in the model space a compact minimised arrangement of the nucleons not provided by placing the two clusters close to one another, as is done with the frozen states. A relatively fast way of doing this is to perform a PAV$^\pi$ minimisation (section 2.1.3). Usually the frozen state with the lowest energy (figure 2.6) is taken as the starting point to speed up the minimisation. However the minimisation does not rely strongly on the starting conditions as the parameters are randomised to some extent at the start of the minimisation procedure.

For the calculation of non-resonant scattering states it is not always necessary to describe in detail the bound states of the compound nucleus, but it is clearly imperative in the case of calculating transition probabilities that the states of importance for the transitions being studied are well reproduced. This requires a certain amount of physical intuition and careful comparison with available data. Including an irrelevant state does no harm to the calculation as the Hamiltonian 'picks out' the states that it wants, however when considering heavier nuclei, for example in the sd-shell, it can be very time consuming to calculate worthless matrix elements. Therefore a judicious choice of which states to include is required.

The Gaussian basis states used in FMD are an overcomplete basis and therefore include the shell model basis states as a subset. However, by minimising the energy without any constraints, as described in section 2.1.3, there is no guarantee that FMD states which have an appreciable overlap with states known as particle-hole excitations in shell-model language will be arrived at. These excited states of the nucleus are saddle points in a multi-dimensional energy surface and depending on their exact form can be quite precipitous and hence difficult to reach by minimisation. However if some physical intuition can be employed to determine what might be the approximate configuration of the nuclei in terms of excitations, then, using constraints during minimisation these type of states can be included in the FMD model space. Examples of the type of constraints that might be used are the quadrupole moment or the number of oscillator quanta. It should be noted that only in rare circumstances will an exact shell-model configuration be arrived at by this method because the FMD states will normally include contributions also from higher shells.

Minimisation under constraints can also supplement the description of the clusters in a scattering or capture reaction because when the clusters are close together they undergo polarisations due to the nuclear force. The quadrupole moment is a good example of such a constraint, if a nucleus is taken and stretched, its new charge distribution corresponds to a change in its quadrupole moment. For larger and larger quadrupole moments, the nucleus starts to dissolve into two distinct clusters; therefore the quadrupole moment starts to resemble a distance measure between the clusters. If the quadrupole moment of the lowest energy frozen state is calculated, then states with quadrupole deformations around this value help to describe the system as the nuclei start to fuse.

In the case of bound states, the amplitude of the wave function outside the range of the nuclear potential is very small, corresponding to the low probability of tunnelling far into the Coulomb barrier. By only calculating frozen states up to a certain relative distance, we set the relative wave function to zero beyond the furthest apart clusters. If the wave function goes to zero within this relative distance then this approximation is good.

However, when considering a scattering state, the amplitude of the wave function is non-zero all the way out to infinity. To describe a scattering state correctly therefore requires the frozen configurations to be matched to the analytically known Coulomb scattering solutions for point-like charges. This matching must be performed at a relative distance between the clusters that is well outside the range of the nuclear interaction; the clusters must also be far enough apart to avoid mutual polarisation due to the Coulomb and centrifugal potentials. Using the COULCC routine from Thompson and Barnett [44][43], the Coulomb wave functions can be easily calculated for any relative distance, energy and orbital angular momentum desired, even with continuation into the complex plane. The extra effort required in describing scattering states therefore amounts to matching the microscopic antisymmetrised many-body state calculated within the FMD framework, to a one-dimensional radial wave function, which is the situation in the 'point charge world' when the clusters are far apart and the only degree of freedom is their relative distance.

The matching is performed by stipulating that beyond some relative distance, the coefficients of the FMD wave function must match those of the Coulomb wave function, this constitutes the boundary conditions. However to be able to impose these boundary conditions which are dependent on the relative distance, a method of measuring the relative distance between the clusters is required. In the 'point charge world', the relative distance between the centres of mass of the charges is an explicit degree of freedom, however in the antisymmetrised many-body world that describes the nuclear physics at small relative distances, this is not the case. When the clusters overlap to a large extent, there is no distinct cluster structure and then due to the indistinguishable nature of the nucleons the relative distance loses its meaning. However, when the clusters are brought further apart, they are distinct entities and a measure of the relative distance should be possible using an appropriate operator. The next section investigates one possible form that such an operator can take.

2.3.2. Measurement of the relative distance

The classical expression for the relative distance between the centres of mass of two clusters is:

$$\vec{X}_{12} = \frac{1}{A_1}\sum_{i\in I_1}^{A_1}\vec{x}_i - \frac{1}{A_2}\sum_{j\in I_2}^{A_2}\vec{x}_j \tag{2.44}$$

where the indices 1 and 2 refer to the cluster number, $\vec{x}_k$ is the position of particle k, A_n is the number of particles in cluster n and $i \in I_n$ means that the index i is chosen from one of the particle numbers in index set I_n.

In quantum mechanics an operator equivalent to (2.44) is required. As the nuclear system under consideration is composed of indistinguishable fermions, the operator $\vec{X}_{12}$ must be symmetric under particle permutations so that it does not scatter out of the antisymmetric part of the Hilbert space. This is achieved by the explicit symmetrisation of the equivalent operator $\underset{\sim}{\vec{X}}_{12}$:

$$\begin{aligned}
\underset{\sim}{\vec{X}}{}^{\mathrm{S}}_{12} &= \frac{1}{A!}\sum_{\text{all }\mathcal{P}}^{A!} \underset{\sim}{\mathcal{P}}\,\underset{\sim}{\vec{X}}_{12}\,\underset{\sim}{\mathcal{P}} \\
\underset{\sim}{\vec{X}}{}^{\mathrm{S}}_{12} &= \frac{1}{A!}\sum_{\text{all }\mathcal{P}}^{A!} \underset{\sim}{\mathcal{P}}\left(\frac{1}{A_1}\sum_{i\in I_1}^{A_1}\underset{\sim}{\vec{x}}(i) - \frac{1}{A_2}\sum_{j\in I_2}^{A_2}\underset{\sim}{\vec{x}}(j)\right)\underset{\sim}{\mathcal{P}}\ .
\end{aligned} \tag{2.45}$$

Using $\underset{\sim}{\mathcal{P}}\ \underset{\sim}{\vec{x}}(i)\ \underset{\sim}{\mathcal{P}} = \underset{\sim}{\vec{x}}(\mathcal{P}(i))$ one obtains:

$$\begin{aligned}
\underset{\sim}{\vec{X}}{}^{\mathrm{S}}_{12} &= \frac{1}{A!}\sum_{\text{all }\mathcal{P}}^{A!}\left(\frac{1}{A_1}\sum_{i\in I_1}^{A_1}\underset{\sim}{\vec{x}}(\mathcal{P}(i)) - \frac{1}{A_2}\sum_{j\in I_2}^{A_2}\underset{\sim}{\vec{x}}(\mathcal{P}(j))\right) \\
&= \frac{1}{A!}\left(\frac{1}{A_1}\sum_{i\in I_1}^{A_1}\sum_{\text{all }\mathcal{P}}^{A!}\underset{\sim}{\vec{x}}(\mathcal{P}(i)) - \frac{1}{A_2}\sum_{j\in I_2}^{A_2}\sum_{\text{all }\mathcal{P}}^{A!}\underset{\sim}{\vec{x}}(\mathcal{P}(j))\right)\ .
\end{aligned} \tag{2.46}$$

As $\mathcal{P}(i)$ can assume any value from 1 up to $A = A_1 + A_2$ and there are $(A-1)!$ possibilities for the permutations of the remaining $A-1$ indices, the following identity holds:

$$\frac{1}{A!}\sum_{\text{all }\mathcal{P}}^{A!}\underset{\sim}{\vec{x}}(\mathcal{P}(i)) = \frac{1}{A!}\,(A-1)!\sum_{i\in I_1\cup I_2}^{A}\underset{\sim}{\vec{x}}(i) = \frac{1}{A}\sum_{i\in I_1\cup I_2}^{A}\underset{\sim}{\vec{x}}(i) = \underset{\sim}{\vec{X}}_{\mathrm{CM}}\ . \tag{2.47}$$

This allows equation (2.46) to be written as:

$$\underset{\sim}{\vec{X}}{}^{\mathrm{S}}_{12} = \frac{1}{A}\left(\frac{1}{A_1}\sum_{i\in I_1}^{A_1}\sum_{j\in I_1\cup I_2}^{A}\underset{\sim}{\vec{x}}(j) - \frac{1}{A_2}\sum_{k\in I_2}^{A_2}\sum_{j\in I_1\cup I_2}^{A}\underset{\sim}{\vec{x}}(j)\right)\ . \tag{2.48}$$

As the first term has no i dependence and the second term no k dependence, $\frac{1}{A_1}\sum_{i\in I_1}^{A_1}\underset{\sim}{\vec{x}}_j = \frac{1}{A_2}\sum_{k\in I_2}^{A_2}\underset{\sim}{\vec{x}}_j = \vec{x}_j$, meaning that equation (2.48) can be written:

$$\underset{\sim}{\vec{X}}{}^{\mathrm{S}}_{12} = \frac{1}{A}\left(\sum_{j\in I_1\cup I_2}^{A}\underset{\sim}{\vec{x}}_j - \sum_{j\in I_1\cup I_2}^{A}\underset{\sim}{\vec{x}}_j\right) = 0\ . \tag{2.49}$$

This shows that the quantum analogue to the classical relative distance cannot be used in a quantum mechanically correct way to construct a relative distance operator for identical particles. Therefore another definition of a quantum mechanical operator that can yield a measure for the relative distance in the antisymmetrised many-body space is required. Such an operator was employed in the doctoral thesis of Alberto Cribeiro [7] and used in the framework of the collective coordinate representation (CCR).

2.3.3. Collective coordinate representation

In the asymptotic region an appropriate ansatz is that a state describing the system can be written as an antisymmetrised tensor product of a relative motion component $\left|\, \chi_{\mathrm{REL}} \right\rangle$, the intrinsic states of the two clusters $\left|\, \Psi_1 \right\rangle$ and $\left|\, \Psi_2 \right\rangle$ and the centre of mass $\left|\, \Psi_{\mathrm{CM}} \right\rangle$:

$$\left|\, \Psi^{(i)} \right\rangle \overset{r\to\infty}{\Longrightarrow} \underset{\sim}{\mathcal{A}} \left[\left|\, \chi^{(i)}_{\mathrm{REL}} \right\rangle \otimes \left|\, \Psi_1 \right\rangle \otimes \left|\, \Psi_2 \right\rangle \right] \otimes \left|\, \Psi_{\mathrm{CM}} \right\rangle \,, \tag{2.50}$$

as $\underset{\sim}{\mathcal{P}} \left|\, \Psi_{\mathrm{CM}} \right\rangle = \left|\, \Psi_{\mathrm{CM}} \right\rangle$ for all permutations. When the clusters are well separated, the antisymmetrisation of the system can logically be split into three parts as seen below in (2.54): antisymmetrisation between the particles in cluster 1 (using $\underset{\sim}{\mathcal{A}}_1$), antisymmetrisation between the particles in cluster 2 (using $\underset{\sim}{\mathcal{A}}_2$) and antisymmetrisation of the particles between the clusters (using $\underset{\sim}{\mathcal{A}}_{12}$). The antisymmetrisers $\underset{\sim}{\mathcal{A}}_1$ and $\underset{\sim}{\mathcal{A}}_2$ are defined in an analogous way to equation (2.3):

$$\underset{\sim}{\mathcal{A}}_n = \frac{1}{A_n!} \sum_{\text{all } \mathcal{P} \in I_n}^{A_n!} \mathrm{sgn}(\mathcal{P}) \underset{\sim}{\mathcal{P}} \qquad n = 1, 2 \,, \tag{2.51}$$

where $\mathcal{P}$ are permutations within the index set I_n.

$\underset{\sim}{\mathcal{A}}_{12}$ antisymmetrises between the two clusters, accounting for all permutations which only involve the exchange of particles between the clusters:

$$\underset{\sim}{\mathcal{A}}_{12} = \frac{A_1! A_2!}{A!} \sum_{\text{all } \mathcal{P}_{12}} \mathrm{sgn}(\mathcal{P}_{12}) \underset{\sim}{\mathcal{P}}_{12} \,, \tag{2.52}$$

meaning that $\mathcal{P}_{12}$ are all permutations between clusters 1 and 2, but not within each cluster. Multiplying these operators together gives the total antisymmetriser $\underset{\sim}{\mathcal{A}}$:

$$\underset{\sim}{\mathcal{A}} = \frac{A_1! A_2!}{A!} \sum_{\text{all } \mathcal{P}_{12}} \mathrm{sgn}(\mathcal{P}_{12}) \underset{\sim}{\mathcal{P}}_{12} \; \frac{1}{A_1!} \sum_{\text{all } \mathcal{P} \in I_1}^{A_1!} \mathrm{sgn}(\mathcal{P}) \underset{\sim}{\mathcal{P}} \; \frac{1}{A_2!} \sum_{\text{all } \mathcal{P}' \in I_2}^{A_2!} \mathrm{sgn}(\mathcal{P}') \underset{\sim}{\mathcal{P}}' \tag{2.53}$$

Therefore (2.50) can be rewritten in the form:

$$\left|\, \Psi^{(i)} \right\rangle \overset{r\to\infty}{\Longrightarrow} \underset{\sim}{\mathcal{A}}_{12} \left[\left|\, \chi^{(i)}_{\mathrm{REL}} \right\rangle \otimes \underset{\sim}{\mathcal{A}}_1 \left|\, \Psi_1 \right\rangle \otimes \underset{\sim}{\mathcal{A}}_2 \left|\, \Psi_2 \right\rangle \right] \otimes \left|\, \Psi_{\mathrm{CM}} \right\rangle \,, \tag{2.54}$$

If the clusters are well separated and therefore their wave functions do not overlap, then the antisymmetrisation between the clusters $\underset{\sim}{\mathcal{A}}_{12}$ is not required except if the two clusters are identical. In this case the permutation is the exchange of one whole cluster with the other. If the cluster has an even number of nucleons this permutation requires an even number of transpositions, for an odd number of nucleons an odd number of transpositions is required.

The state $\left|\, \chi_{\mathrm{REL}} \right\rangle$ describes the relative motion between the clusters that must be matched to the Coulomb wave function. The process of disentangling the relative motion from the intrinsic motion of the clusters and the centre of mass motion of the whole system is discussed in more detail in section 2.3.4.

The operator used to measure the relative distance between the clusters is A times the mean square radius of the whole system:

$$\underset{\sim}{B} = \frac{1}{A} \sum_{\substack{i,j=1 \\ i<j}}^{A} \left(\underset{\sim}{\vec{x}}(i) - \underset{\sim}{\vec{x}}(j) \right)^2 \ . \tag{2.55}$$

This can be written as the sum of three operators that act independently in the relative motion space and the intrinsic spaces of clusters 1 and 2:

$$\underset{\sim}{B} = \mu_{\mathrm{A}} \underset{\sim}{r}^2 + A_1 \underset{\sim}{R}_1^2 + A_2 \underset{\sim}{R}_2^2 \ , \tag{2.56}$$

where μ_{A} is the reduced mass number of the whole system $\frac{A_1 A_2}{A_1 + A_2}$, $\underset{\sim}{R}_1^2$ and $\underset{\sim}{R}_2^2$ measure the mean square radii of clusters 1 and 2 respectively:

$$\underset{\sim}{R}_1^2 = \frac{1}{A_1^2} \sum_{\substack{i,j \in I_1 \\ i<j}} \left(\underset{\sim}{\vec{x}}(i) - \underset{\sim}{\vec{x}}(j) \right)^2 \qquad \underset{\sim}{R}_2^2 = \frac{1}{A_2^2} \sum_{\substack{i,j \in I_2 \\ i<j}} \left(\underset{\sim}{\vec{x}}(i) - \underset{\sim}{\vec{x}}(j) \right)^2 \tag{2.57}$$

and $\underset{\sim}{r}^2$ measures the relative distance between the centres of mass of the two clusters:

$$\underset{\sim}{r}^2 = \left(\underset{\sim}{\vec{X}}_1 - \underset{\sim}{\vec{X}}_2 \right)^2 \ ; \qquad \underset{\sim}{\vec{X}}_1 = \frac{1}{A_1} \sum_{i \in I_1}^{A_1} \underset{\sim}{\vec{x}}(i) \ ; \qquad \underset{\sim}{\vec{X}}_2 = \frac{1}{A_2} \sum_{i \in I_2}^{A_2} \underset{\sim}{\vec{x}}(i) \ . \tag{2.58}$$

When the clusters are well separated, the overlap between two states of the type shown in equation (2.54) for $\left|\, \Psi_1 \right\rangle \neq \left|\, \Psi_2 \right\rangle$ is given by:

$$\begin{aligned} &\left\langle \Psi^{(i)} \,\middle|\, \Psi^{(j)} \right\rangle \\ &= \left\langle \chi_{\mathrm{REL}}^{(i)} \,\middle|\, \chi_{\mathrm{REL}}^{(j)} \right\rangle \left\langle \Psi_1 \,\middle|\, \underset{\sim}{\mathcal{A}}_1 \,\middle|\, \Psi_1 \right\rangle \left\langle \Psi_2 \,\middle|\, \underset{\sim}{\mathcal{A}}_2 \,\middle|\, \Psi_2 \right\rangle \left\langle \Psi_{\mathrm{CM}} \,\middle|\, \Psi_{\mathrm{CM}} \right\rangle \\ &= \left\langle \chi_{\mathrm{REL}}^{(i)} \,\middle|\, \chi_{\mathrm{REL}}^{(j)} \right\rangle \left\langle \Psi_1 \,\middle|\, \Psi_1 \right\rangle_a \left\langle \Psi_2 \,\middle|\, \Psi_2 \right\rangle_a \left\langle \Psi_{\mathrm{CM}} \,\middle|\, \Psi_{\mathrm{CM}} \right\rangle \ , \end{aligned} \tag{2.59}$$

where a subscript 'a' denotes that a state is antisymmetrised. Matrix elements of $\underset{\sim}{B}$ acting on well separated states of the type defined in (2.54) are given by:

$$\begin{aligned}
&\left\langle \Psi^{(i)} \,\middle|\, \underset{\sim}{B} \,\middle|\, \Psi^{(j)} \right\rangle = \\
&\qquad \mu_{\mathrm{A}} \left\langle \chi^{(i)}_{\mathrm{REL}} \,\middle|\, \underset{\sim}{r}^2 \,\middle|\, \chi^{(j)}_{\mathrm{REL}} \right\rangle \left\langle \Psi_1 \,\middle|\, \Psi_1 \right\rangle_a \left\langle \Psi_2 \,\middle|\, \Psi_2 \right\rangle_a \left\langle \Psi_{\mathrm{CM}} \,\middle|\, \Psi_{\mathrm{CM}} \right\rangle \\
&\qquad + A_1 \left\langle \chi^{(i)}_{\mathrm{REL}} \,\middle|\, \chi^{(j)}_{\mathrm{REL}} \right\rangle \left\langle \Psi_1 \,\middle|\, \underset{\sim}{R}_1^2 \,\middle|\, \Psi_1 \right\rangle_a \left\langle \Psi_2 \,\middle|\, \Psi_2 \right\rangle_a \left\langle \Psi_{\mathrm{CM}} \,\middle|\, \Psi_{\mathrm{CM}} \right\rangle \\
&\qquad + A_2 \left\langle \chi^{(i)}_{\mathrm{REL}} \,\middle|\, \chi^{(j)}_{\mathrm{REL}} \right\rangle \left\langle \Psi_1 \,\middle|\, \Psi_1 \right\rangle_a \left\langle \Psi_2 \,\middle|\, \underset{\sim}{R}_2^2 \,\middle|\, \Psi_2 \right\rangle_a \left\langle \Psi_{\mathrm{CM}} \,\middle|\, \Psi_{\mathrm{CM}} \right\rangle ,
\end{aligned} \tag{2.60}$$

which can be rearranged to give:

$$\begin{aligned}
&\frac{\left\langle \Psi^{(i)} \,\middle|\, \underset{\sim}{B} \,\middle|\, \Psi^{(j)} \right\rangle_a}{\left\langle \Psi_1 \,\middle|\, \Psi_1 \right\rangle_a \left\langle \Psi_2 \,\middle|\, \Psi_2 \right\rangle_a \left\langle \Psi_{\mathrm{CM}} \,\middle|\, \Psi_{\mathrm{CM}} \right\rangle} = \\
&\mu_{\mathrm{A}} \left\langle \chi^{(i)}_{\mathrm{REL}} \,\middle|\, \underset{\sim}{r}^2 \,\middle|\, \chi^{(j)}_{\mathrm{REL}} \right\rangle + \left(A_1 \frac{\left\langle \Psi_1 \,\middle|\, \underset{\sim}{R}_1^2 \,\middle|\, \Psi_1 \right\rangle_a}{\left\langle \Psi_1 \,\middle|\, \Psi_1 \right\rangle_a} + A_2 \frac{\left\langle \Psi_2 \,\middle|\, \underset{\sim}{R}_2^2 \,\middle|\, \Psi_2 \right\rangle_a}{\left\langle \Psi_2 \,\middle|\, \Psi_2 \right\rangle_a} \right) \left\langle \chi^{(i)}_{\mathrm{REL}} \,\middle|\, \chi^{(j)}_{\mathrm{REL}} \right\rangle .
\end{aligned} \tag{2.61}$$

This means that in the asymptotic region, the eigenvalues of $\underset{\sim}{B}$ are the eigenvalues of $\underset{\sim}{r}^2$ shifted by a constant value which depends on the mean square radii of the two clusters. To ease notation, the antisymmetrisation of and between the clusters should be assumed throughout the rest of the thesis unless explicitly referred to.

In the part of the Hilbert space where the clusters are well separated, the eigenstates of $\underset{\sim}{B}$ are denoted by:

$$\underset{\sim}{B} \, \left| B; \Psi_1 \Psi_2; i \right\rangle = b_i \, \left| B; \Psi_1 \Psi_2; i \right\rangle . \tag{2.62}$$

Using the preceding formulae it is clear that the eigenvalues of $\underset{\sim}{B}$ are easily connectible to the eigenvalues of $\underset{\sim}{r}^2$, which is what is required to effectively measure the relative distance. Their eigenstates are also the same, which allows a representation of the relative distance $\underset{\sim}{r}$ to be given by:

$$\underset{\sim}{r} = \sum_i \left| B; \Psi_1 \Psi_2; i \right\rangle r_i \left\langle B; \Psi_1 \Psi_2; i \right| , \tag{2.63}$$

with the eigenvalues:

$$r_i = r(b_i) = \sqrt{\frac{1}{\mu_{\mathrm{A}}} \big(b_i - A_1 \, R_1^2 - A_2 \, R_2^2 \big)} \; . \tag{2.64}$$

Due to this relation, the operator $\underset{\sim}{B}$ is referred to as the collective coordinate and

$\big| \, B; \Psi_1\Psi_2; i \, \big\rangle$ as the collective coordinate representation. As a shorthand notation, from now on these eigenstates will be denoted by $\big| \, B; i \, \big\rangle$ which is appropriate in this thesis as we will consider only single channel capture reactions; it should be borne in mind however that if the incoming and outgoing channels consisted of different clusters $\big| \, B; \Psi_1\Psi_2, i \, \big\rangle \neq \big| \, B; \Psi_1'\Psi_2', i \, \big\rangle$ then this notation would not be appropriate.

Diagonalising $\underset{\sim}{B}$ in the translationally and rotationally invariant many-body states defined earlier (2.36) gives:

$$\begin{aligned} \underset{\sim}{B}\big| \, B; i \, \big\rangle &= b_i \big| \, B; i \, \big\rangle \\ \big| \, B; i \, \big\rangle &= \sum_{a\in \mathrm{F}}^{n^{\mathrm{F}}} \sum_{\kappa_a=1}^{n^{(a)}} \big| \, Q^{(a)}; J^\pi M; \kappa_a \, \big\rangle \beta_i^{(a,\kappa_a)} \; . \end{aligned} \tag{2.65}$$

The measurement of the relative distance is only required and well defined in the asymptotic region, therefore the operator $\underset{\sim}{B}$ is only diagonalised in the subset of frozen states $\{\mathrm{F}\}$. In this work all the frozen states that are used are axially symmetric and hence there is only one K-projection for each Slater determinant, namely $K = J$. As can be seen from equation (2.33), this means that there is no K-mixing between these states and the sum over κ_a in equation (2.65) disappears. This eigenvalue equation can then be written in matrix form as:

$$\begin{aligned} \sum_{j\in \mathrm{F}}^{n^{\mathrm{F}}} \mathsf{B}_{ij}\beta_j^{(n)} &= b_n \sum_{j\in \mathrm{F}}^{n^{\mathrm{F}}} n_{ij}\beta_j^{(n)} \\ \sum_{j\in \mathrm{F}}^{n^{\mathrm{F}}} \mu_{\mathrm{A}} r_{ij}^2 \beta_j^{(n)} &= \big(b_n - A_1R_1^2 - A_2R_2^2\big) \sum_{j\in \mathrm{F}}^{n^{\mathrm{F}}} n_{ij}\beta_j^{(n)} \; , \end{aligned} \tag{2.66}$$

where $n_{ij} = \big\langle \, \chi_{\mathrm{REL}}^{(i)} \, \big| \, \chi_{\mathrm{REL}}^{(j)} \, \big\rangle$ and:

$$\mathsf{B}_{ij} = \frac{\big\langle \, \Psi^{(i)} \, \big| \, \underset{\sim}{B} \, \big| \, \Psi^{(j)} \, \big\rangle_a}{\big\langle \, \Psi_1 \, \big| \, \Psi_1 \, \big\rangle_a \big\langle \, \Psi_2 \, \big| \, \Psi_2 \, \big\rangle_a \big\langle \, \Psi_{\mathrm{CM}} \, \big| \, \Psi_{\mathrm{CM}} \, \big\rangle} \; . \tag{2.67}$$

Whenever an eigenvalue problem is solved in the program, a singular value decomposition is performed to ensure the stability of the process, as was shown in equation (2.29). If the singular value decomposition throws out frozen states it signifies that they are linearly dependent. This indicates that the spacing between the frozen states is too small and hence this subset of the Hilbert space is too dense, therefore the program exits. This must then be rectified by using a wider spacing between the frozen states and recalculating the matrix elements. In figure 2.7, the relative distance is plotted against the separations at which the

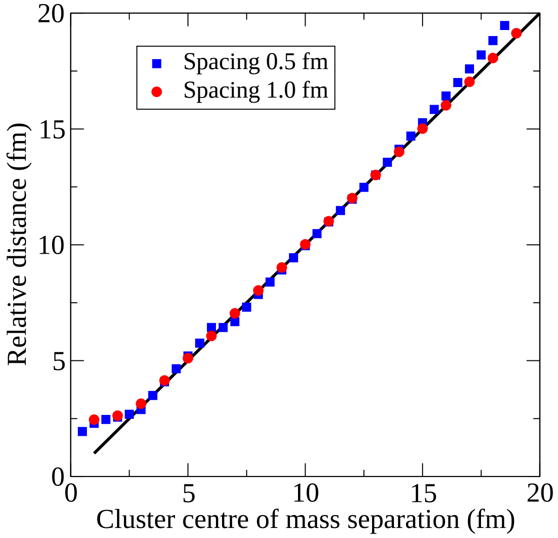

Figure 2.7.: Relative distance calculated from the eigenvalues of the relative distance operator using 2.64, for two different values of spacing of frozen states positioned from 1 - 20 fm. A line of $y = x$ (black solid) is also plotted to serve as a reference. The clusters making up the frozen states are ^{14}C and ^{4}He.

Slater determinants were placed. If the spacing between the frozen states was well chosen, then apart from at the edges of the Hilbert space, these two quantities should be equal giving points that lie on top of the black $y = x$ line. This is the case with the spacing of 1 fm, however for 0.5 fm spacing the frozen states are too densely packed and there are larger deviations from the line, around 7 fm and again from 16 fm outwards. It is not clear as to why the the deviations should again get worse in this particular case at 7 fm rather than just getting progressively worse towards the edges of the Hilbert space, but as these deviations are due to trying to invert a nearly singular overlap matrix to solve the generalised eigenvalue problem (2.65), the results are likely to be unpredictable. In any case, this is no source for concern as, in the normal run of the program, linear dependencies such as those for the 0.5 fm spacing are detected and the program exits with an error message, hence allowing for the problem to be rectified.

In the 'point charge world', which is a good description of the system when the clusters are well separated, the identity operator is given by:

$$\underset{\sim}{1} = \int_0^\infty dr \big| \, r \, \big\rangle \big\langle \, r \, \big| \tag{2.68}$$

which we approximate in our model space by:

$$\underset{\sim}{1} \approx \sum_i \Delta_i \big| \, r_i \, \big\rangle \big\langle \, r_i \, \big| \ , \tag{2.69}$$

where $r_i = r(b_i)$ and Δ_i is the spacing between the grid points:

$$\Delta_i = \frac{r_{i+1} - r_{i-1}}{2} \ . \tag{2.70}$$

An expression for the wave function $\chi(r)$ can be found by inserting this identity:

$$\big| \, \chi \, \big\rangle = \int_0^\infty dr \big| \, r \, \big\rangle \big\langle \, r \, \big| \, \chi \, \big\rangle = \int_0^\infty dr \big| \, r \, \big\rangle \chi(r) \ , \tag{2.71}$$

writing this in terms of the states at the discrete distances we have available in the 'point charge world' gives:

$$\big| \, \chi \, \big\rangle = \sum_{i=1}^{n} \Delta_i \big| \, r_i \, \big\rangle \chi(r_i) \ . \tag{2.72}$$

In the FMD many-body world, an operator can be defined which functions as a unit operator under certain restrictions:

- It must operate in the part of the Hilbert space where the two clusters are well separated.
- The clusters must not be so close to the edge of the model space that the localisation of their states is impaired.

The unit operator in the frozen subspace {F} is defined as:

$$\underset{\sim}{1}^{\mathrm{F}} = \sum_{i=1}^{n^{\mathrm{F}}} \big| \, B; i \, \big\rangle \big\langle \, B; i \, \big| \ . \tag{2.73}$$

By comparing equations (2.69) and (2.73), the two prescriptions can be equated:

$$\frac{1}{\sqrt{\Delta_i}} \big| \, B; i \, \big\rangle \mathrel{\hat{=}} \big| \, r_i \, \big\rangle \ . \tag{2.74}$$

This allows the wave functions in the two cases to be equated under the conditions given above:

$$\frac{1}{\sqrt{\Delta_i}} \big\langle \, B; i \, \big| \, \Psi \, \big\rangle \mathrel{\hat{=}} \big\langle \, r_i \, \big| \, \chi \, \big\rangle = \chi(r_i) \ . \tag{2.75}$$

This concludes a description of the method by which the antisymmetric many-body Hilbert space with its many degrees of freedom, in which the FMD states belong, can be connected to the 'point charge world' with its single degree of freedom which describes the system in the asymptotic region.

In this section we have considered the case in which the centres of mass, the relative and the intrinsic motion of the clusters could be totally separated from one another, in the next section we consider under what circumstances this is actually possible.

2.3.4. Decoupling of intrinsic cluster motion from total centre of mass and relative motion

In coordinate space representation, the Slater determinant for a system of A fermions is given by:

$$\left\langle\, \vec{x}_1 \,\right| \otimes \left\langle\, \vec{x}_2 \,\right| \otimes \cdots \otimes \left\langle\, \vec{x}_{A-1} \,\right| \otimes \left\langle\, \vec{x}_A \,\right| \underset{\sim}{\mathcal{A}} \left|\, q_1 \,\right\rangle \otimes \left|\, q_2 \,\right\rangle \otimes \cdots \otimes \left|\, q_{A-1} \,\right\rangle \otimes \left|\, q_A \,\right\rangle . \tag{2.76}$$

Representing each single-particle state by one Gaussian and applying the antisymmetriser to the kets (and hence the b_k), this can be written:

$$\begin{aligned} &\frac{1}{A!} \sum_{\text{all } \mathcal{P}} \operatorname{sgn}(\mathcal{P}) \exp\left(- \sum_{k=1}^{A} \frac{\left(\vec{x}_k - \vec{b}_{\mathcal{P}(k)} \right)^2}{2 a_{\mathcal{P}(k)}} \right) \\ &\qquad \times \left|\, \chi_{\mathcal{P}(1)} \,\right\rangle \otimes \left|\, \xi_{\mathcal{P}(1)} \,\right\rangle \otimes \cdots \otimes \left|\, \chi_{\mathcal{P}(A)} \,\right\rangle \otimes \left|\, \xi_{\mathcal{P}(A)} \,\right\rangle . \end{aligned} \tag{2.77}$$

As explained in 2.3.3, the antisymmetriser $\underset{\sim}{\mathcal{A}}$ can be split up as follows:

$$\underset{\sim}{\mathcal{A}} = \underset{\sim}{\mathcal{A}}_{12}\, \underset{\sim}{\mathcal{A}}_1\, \underset{\sim}{\mathcal{A}}_2 \,, \tag{2.78}$$

This also means that the set of Gaussians representing each of the two clusters can be written separately:

$$\begin{aligned} &\frac{A_1! A_2!}{A!} \underset{\sim}{\mathcal{A}}_{12} \frac{1}{A_1!} \sum_{\text{all } \mathcal{P} \in I_1} \operatorname{sgn}(\mathcal{P}) \exp\left(- \sum_{i \in I_1} \frac{\left(\vec{x}_i - \vec{b}_{\mathcal{P}(i)} \right)^2}{2 a_{\mathcal{P}(i)}} \right) \underset{\sim}{\mathcal{P}} \left|\, \Xi_1 \,\right\rangle \\ &\qquad \otimes \frac{1}{A_2!} \sum_{\text{all } \mathcal{P}' \in I_2} \operatorname{sgn}(\mathcal{P}') \exp\left(- \sum_{j \in I_2} \frac{\left(\vec{x}_j - \vec{b}_{\mathcal{P}'(j)} \right)^2}{2 a_{\mathcal{P}'(j)}} \right) \underset{\sim}{\mathcal{P}'} \left|\, \Xi_2 \,\right\rangle \end{aligned} \tag{2.79}$$

where $\left|\, \Xi_1 \,\right\rangle = \left|\, \chi_1 \,\right\rangle \otimes \left|\, \xi_1 \,\right\rangle \otimes \left|\, \chi_2 \,\right\rangle \otimes \left|\, \xi_2 \,\right\rangle \otimes \ldots \otimes \left|\, \chi_{A_1} \,\right\rangle \otimes \left|\, \xi_{A_1} \,\right\rangle$ (and the analogue for cluster 2). A_1 and A_2 are the particle numbers of clusters 1 and 2 respectively.

As the aim is to separate the intrinsic cluster motion, the total centre of mass and the total relative motion from each other; it is helpful to define the intrinsic coordinates and the mean parameters within a cluster with respect to its centre of mass:

$$\begin{aligned} \vec{\xi}_i &= \vec{x}_i - \vec{X}_1 \qquad & \vec{\beta}_i &= \vec{b}_i - \vec{B}_1 \qquad & i &\in I_1 \\ \vec{\xi}_j &= \vec{x}_j - \vec{X}_2 \qquad & \vec{\beta}_j &= \vec{b}_j - \vec{B}_2 \qquad & j &\in I_2 \end{aligned} \tag{2.80}$$

where $i \in I_1$ means that i is taken from index set 1 and therefore runs from 1 to A_1. The centres of mass of the clusters are given by:

$$\begin{aligned} \vec{X}_1 &= \frac{1}{A_1}\sum_{i\in I_1}\vec{x}_i \qquad & \vec{X}_2 &= \frac{1}{A_2}\sum_{j\in I_2}\vec{x}_j \\ \vec{B}_1 &= \frac{1}{A_1}\sum_{i\in I_1}\vec{b}_i \qquad & \vec{B}_2 &= \frac{1}{A_2}\sum_{j\in I_2}\vec{b}_j \end{aligned} \tag{2.81}$$

the coordinates and mean parameters for the centre of mass and relative motion of the total system are:

$$\begin{aligned} \vec{X}_{\mathrm{CM}} &= \frac{1}{A}\sum_{k\in(I_1\cup I_2)}\vec{x}_k = \frac{1}{A}\left(A_1\vec{X}_1 + A_2\vec{X}_2\right) \qquad & \vec{X}_{\mathrm{REL}} &= \vec{X}_1 - \vec{X}_2 \\ \vec{B}_{\mathrm{CM}} &= \frac{1}{A}\sum_{k\in(I_1\cup I_2)}\vec{b}_k = \frac{1}{A}\left(A_1\vec{B}_1 + A_2\vec{B}_2\right) \qquad & \vec{B}_{\mathrm{REL}} &= \vec{B}_1 - \vec{B}_2 \; . \end{aligned} \tag{2.82}$$

By construction

$$\sum_{i\in I_1}\frac{\left(\vec{\xi}_i - \vec{\beta}_i + \vec{X}_1 - \vec{B}_1\right)^2}{2a_i} = \sum_{i=1}^{A_1}\frac{(x_i - b_i)^2}{2a_i}, \tag{2.83}$$

using this (2.79) can be written:

$$\begin{aligned} &\frac{1}{A!}\underset{\sim}{\mathcal{A}}_{12}\sum_{\text{all }\mathcal{P}\in I_1}\operatorname{sgn}(\mathcal{P})\exp\left[-\sum_{i\in I_1}\frac{\left(\vec{\xi}_i - \vec{\beta}_{\mathcal{P}(i)} + \vec{X}_1 - \vec{B}_1\right)^2}{2a_{\mathcal{P}(i)}}\right]\underset{\sim}{\mathcal{P}}\big|\,\Xi_1\,\big\rangle \\ &\qquad\otimes\sum_{\text{all }\mathcal{P}'\in I_2}\operatorname{sgn}(\mathcal{P}')\exp\left[-\sum_{j\in I_2}\frac{\left(\vec{\xi}_j - \vec{\beta}_{\mathcal{P}'(j)} + \vec{X}_2 - \vec{B}_2\right)^2}{2a_{\mathcal{P}'(j)}}\right]\underset{\sim}{\mathcal{P}}'\big|\,\Xi_2\,\big\rangle \; . \end{aligned} \tag{2.84}$$

The next step is to express $\vec{X}_1$, $\vec{X}_2$, $\vec{B}_1$ and $\vec{B}_2$, in terms of $\vec{X}_{\mathrm{CM}}$, $\vec{X}_{\mathrm{REL}}$, $\vec{B}_{\mathrm{CM}}$

and $\vec{B}_{\mathrm{REL}}$ and thus to replace the collective cluster coordinates with the collective coordinates of the whole system. This can be achieved by rearranging the expressions in (2.82) to give:

$$\begin{aligned} \vec{X}_1 &= \vec{X}_{\mathrm{CM}} + \frac{A_2}{A}\vec{X}_{\mathrm{REL}} \qquad & \vec{X}_2 &= \vec{X}_{\mathrm{CM}} - \frac{A_1}{A}\vec{X}_{\mathrm{REL}} \\ \vec{B}_1 &= \vec{B}_{\mathrm{CM}} + \frac{A_2}{A}\vec{B}_{\mathrm{REL}} \qquad & \vec{B}_2 &= \vec{B}_{\mathrm{CM}} - \frac{A_1}{A}\vec{B}_{\mathrm{REL}} \ . \end{aligned} \tag{2.85}$$

Substituting these expressions into (2.84) gives:

$$\begin{aligned} &\frac{1}{A!}\,\underset{\sim}{\mathcal{A}}_{12} \sum_{\substack{\text{all } \mathcal{P}\in I_1 \\ \text{all } \mathcal{P}'\in I_2}} \operatorname{sgn}(\mathcal{P}) \operatorname{sgn}(\mathcal{P}')\, \underset{\sim}{\mathcal{P}}\big|\,\Xi_1\,\big\rangle \otimes \underset{\sim}{\mathcal{P}}'\big|\,\Xi_2\,\big\rangle \\ &\quad \exp\left[-\sum_{i\in I_1} \frac{\left[\left(\vec{\xi}_i - \vec{\beta}_{\mathcal{P}(i)}\right) + \left(\vec{X}_{\mathrm{CM}} - \vec{B}_{\mathrm{CM}}\right) + \frac{A_2}{A}\left(\vec{X}_{\mathrm{REL}} - \vec{B}_{\mathrm{REL}}\right)\right]^2}{2a_{\mathcal{P}(i)}}\right] \\ &\qquad \exp\left[-\sum_{j\in I_2} \frac{\left[\left(\vec{\xi}_j - \vec{\beta}_{\mathcal{P}'(j)}\right) + \left(\vec{X}_{\mathrm{CM}} - \vec{B}_{\mathrm{CM}}\right) - \frac{A_1}{A}\left(\vec{X}_{\mathrm{REL}} - \vec{B}_{\mathrm{REL}}\right)\right]^2}{2a_{\mathcal{P}'(j)}}\right] . \end{aligned} \tag{2.86}$$

Multiplying these terms out and grouping the resultant terms together that exhibit a coupling between the centre of mass, relative motion and cluster coordinates:

$$
\begin{aligned}
&\frac{1}{A!}\,\underset{\sim}{\mathcal{A}}_{12} \sum_{\substack{\text{all } \mathcal{P}\in I_1\\ \text{all } \mathcal{P}'\in I_2}} \operatorname{sgn}\left(\mathcal{P}\right)\operatorname{sgn}\left(\mathcal{P}'\right)\\
&\quad\exp\left[-\sum_{i\in I_1}\left(\frac{2\left(\vec{\xi}_i-\vec{\beta}_{\mathcal{P}(i)}\right)\left(\vec{X}_{\mathrm{CM}}-\vec{B}_{\mathrm{CM}}\right)+\frac{2A_2}{A}\left(\vec{\xi}_i-\vec{\beta}_{\mathcal{P}(i)}\right)\left(\vec{X}_{\mathrm{REL}}-\vec{B}_{\mathrm{REL}}\right)+\frac{2A_2}{A}\left(\vec{X}_{\mathrm{CM}}-\vec{B}_{\mathrm{CM}}\right)\left(\vec{X}_{\mathrm{REL}}-\vec{B}_{\mathrm{REL}}\right)}{2a_{\mathcal{P}(i)}}\right)\right]\\
&\quad\exp\left[-\sum_{j\in I_2}\left(\frac{2\left(\vec{\xi}_j-\vec{\beta}_{\mathcal{P}'(j)}\right)\left(\vec{X}_{\mathrm{CM}}-\vec{B}_{\mathrm{CM}}\right)-\frac{2A_1}{A}\left(\vec{\xi}_j-\vec{\beta}_{\mathcal{P}'(j)}\right)\left(\vec{X}_{\mathrm{REL}}-\vec{B}_{\mathrm{REL}}\right)-\frac{2A_1}{A}\left(\vec{X}_{\mathrm{CM}}-\vec{B}_{\mathrm{CM}}\right)\left(\vec{X}_{\mathrm{REL}}-\vec{B}_{\mathrm{REL}}\right)}{2a_{\mathcal{P}'(j)}}\right)\right]\\
&\qquad\exp\left[-\sum_{i\in I_1}\left(\frac{\left(\vec{\xi}_i-\vec{\beta}_{\mathcal{P}(i)}\right)^2+\left(\vec{X}_{\mathrm{CM}}-\vec{B}_{\mathrm{CM}}\right)^2+\frac{A_2^2}{A^2}\left(\vec{X}_{\mathrm{REL}}-\vec{B}_{\mathrm{REL}}\right)^2}{2a_{\mathcal{P}(i)}}\right)\right]\\
&\qquad\exp\left[-\sum_{j\in I_2}\left(\frac{\left(\vec{\xi}_j-\vec{\beta}_{\mathcal{P}'(j)}\right)^2+\left(\vec{X}_{\mathrm{CM}}-\vec{B}_{\mathrm{CM}}\right)^2+\frac{A_1^2}{A^2}\left(\vec{X}_{\mathrm{REL}}-\vec{B}_{\mathrm{REL}}\right)^2}{2a_{\mathcal{P}'(j)}}\right)\right]\underset{\sim}{\mathcal{P}}\big|\,\Xi_1\,\big\rangle\otimes\underset{\sim}{\mathcal{P}}'\big|\,\Xi_2\,\big\rangle\;.
\end{aligned}
\tag{2.87}
$$

There are then three possible situations that can be studied by looking at equation (2.87).

1. All the states in both clusters have an equal width a.
2. The widths of the states within each individual cluster are the same but the two clusters have different widths a_1 and a_2.
3. The widths are different.

In the first case of all equal widths, all the terms from (2.87) can be combined into one exponential term. This means that the two terms coupling $\vec{X}_{\text{CM}}$, $\vec{X}_{\text{REL}}$, $\vec{B}_{\text{CM}}$ and $\vec{B}_{\text{REL}}$ in the first two exponentials cancel each other out. Also, using equations (2.80) and (2.81):

$$\sum_{i\in I_1} \vec{\xi}_i = \sum_{i\in I_1} \left(\vec{x}_i - \vec{X}_1\right) = \sum_{i\in I_1} \left(\vec{x}_i - \frac{1}{A_1}\sum_{j\in I_1}\vec{x}_j\right) = \sum_{i\in I_1}\vec{x}_i - \sum_{j\in I_1}\vec{x}_j = 0 \quad (2.88)$$

and the same for the β_i. This means that if all the widths in one cluster are equal, the other two coupling terms also drop out of equation (2.87), leaving just the last two exponentials:

$$\frac{1}{A!}\,\underset{\sim}{\mathcal{A}}_{12} \sum_{\substack{\text{all } \mathcal{P}\in I_1 \\ \text{all } \mathcal{P}'\in I_2}} \operatorname{sgn}(\mathcal{P})\operatorname{sgn}(\mathcal{P}')\,\underset{\sim}{\mathcal{P}}\big|\,\Xi_1\,\big\rangle \otimes \underset{\sim}{\mathcal{P}}'\big|\,\Xi_2\,\big\rangle$$
$$\exp\left[-\sum_{i\in I_1}\left(\frac{\left(\vec{\xi}_i - \vec{\beta}_{\mathcal{P}(i)}\right)^2 + \left(\vec{X}_{\text{CM}} - \vec{B}_{\text{CM}}\right)^2 + \frac{A_2^2}{A^2}\left(\vec{X}_{\text{REL}} - \vec{B}_{\text{REL}}\right)^2}{2a_{\mathcal{P}(i)}}\right)\right]$$
$$\exp\left[-\sum_{j\in I_2}\left(\frac{\left(\vec{\xi}_j - \vec{\beta}_{\mathcal{P}'(j)}\right)^2 + \left(\vec{X}_{\text{CM}} - \vec{B}_{\text{CM}}\right)^2 + \frac{A_1^2}{A^2}\left(\vec{X}_{\text{REL}} - \vec{B}_{\text{REL}}\right)^2}{2a_{\mathcal{P}'(j)}}\right)\right], \quad (2.89)$$

so that there is no longer any coupling between the intrinsic relative and centre of mass coordinates. This is consistent with the ansatz used in the Resonating Group Method (RGM) and [50].

In the second case, where within each cluster all particles have the same width but the two clusters have different widths, (2.88) can still be used to remove the coupling between the intrinsic coordinates and the centre of mass and the relative motion; however, the coupling between the relative motion and the centre of mass still remains as the widths of the two clusters are different. The way to remove this coupling is to make the wave function invariant under translation. This is done by projecting (2.87) on the momentum zero eigenstate of total momentum (see equation (2.14)):

$$
\begin{aligned}
= \frac{1}{2\pi^3} \int \mathrm{d}^3X \ \exp\left(-\vec{X}\frac{\partial}{\partial \vec{X}_{\mathrm{CM}}}\right) \frac{1}{A!}\, \underset{\sim}{\mathcal{A}}_{12} \sum_{\substack{\text{all } \mathcal{P}\in I_1 \\ \text{all } \mathcal{P}'\in I_2}} \operatorname{sgn}(\mathcal{P}) \operatorname{sgn}(\mathcal{P}') \\
\exp\left[-\left(\frac{1}{a_1}+\frac{1}{a_2}\right)\frac{A_1A_2}{A}\left(\vec{X}_{\mathrm{CM}}-\vec{B}_{\mathrm{CM}}\right)\left(\vec{X}_{\mathrm{REL}}-\vec{B}_{\mathrm{REL}}\right)\right] \\
\exp\left[-\frac{1}{2a_1}\sum_{i\in I_1}\left(\vec{\xi}_i-\vec{\beta}_{\mathcal{P}(i)}\right)^2-\frac{A_1}{2a_1}\left(\vec{X}_{\mathrm{CM}}-\vec{B}_{\mathrm{CM}}\right)^2-\frac{A_1}{2a_1}\frac{A_2^2}{A^2}\left(\vec{X}_{\mathrm{REL}}-\vec{B}_{\mathrm{REL}}\right)^2\right] \\
\exp\left[-\frac{1}{2a_2}\sum_{j\in I_2}\left(\vec{\xi}_j-\vec{\beta}_{\mathcal{P}'(j)}\right)^2-\frac{A_2}{2a_2}\left(\vec{X}_{\mathrm{CM}}-\vec{B}_{\mathrm{CM}}\right)^2-\frac{A_2}{2a_2}\frac{A_1^2}{A^2}\left(\vec{X}_{\mathrm{REL}}-\vec{B}_{\mathrm{REL}}\right)^2\right] \\
\underset{\sim}{\mathcal{P}}\left|\,\Xi_1\right\rangle \otimes \underset{\sim}{\mathcal{P}}'\left|\,\Xi_2\right\rangle \ ,
\end{aligned}
\tag{2.90}
$$

where the centre of mass and relative motion dependent terms have been moved outside the sums as the width in each cluster no longer depends on the particle number.

$$
\begin{aligned}
= \frac{1}{2\pi^3} \int \mathrm{d}^3X \ \exp\left(-\vec{X}\frac{\partial}{\partial \vec{X}_{\mathrm{CM}}}\right) \frac{1}{A!}\, \underset{\sim}{\mathcal{A}}_{12} \sum_{\substack{\text{all } \mathcal{P}\in I_1 \\ \text{all } \mathcal{P}'\in I_2}} \operatorname{sgn}(\mathcal{P}) \operatorname{sgn}(\mathcal{P}') \\
\exp\left[-\left(\frac{1}{a_1}+\frac{1}{a_2}\right)\frac{A_1A_2}{A}\left(\vec{X}_{\mathrm{CM}}-\vec{B}_{\mathrm{CM}}\right)^2\left(\frac{\vec{X}_{\mathrm{REL}}-\vec{B}_{\mathrm{REL}}}{\vec{X}_{\mathrm{CM}}-\vec{B}_{\mathrm{CM}}}+\frac{A_1}{2a_1}+\frac{A_2}{2a_2}\right)\right] \\
\exp\left[-\frac{1}{2a_1}\sum_{i\in I_1}\left(\vec{\xi}_i-\vec{\beta}_{\mathcal{P}(i)}\right)^2-\frac{1}{2a_2}\sum_{j\in I_2}\left(\vec{\xi}_j-\vec{\beta}_{\mathcal{P}'(j)}\right)^2\right] \\
\exp\left[-\frac{A_1}{2a_1}\frac{A_2^2}{A^2}\left(\vec{X}_{\mathrm{REL}}-\vec{B}_{\mathrm{REL}}\right)^2-\frac{A_2}{2a_2}\frac{A_1^2}{A^2}\left(\vec{X}_{\mathrm{REL}}-\vec{B}_{\mathrm{REL}}\right)^2\right] \\
\underset{\sim}{\mathcal{P}}\left|\,\Xi_1\right\rangle \otimes \underset{\sim}{\mathcal{P}}'\left|\,\Xi_2\right\rangle \ .
\end{aligned}
\tag{2.91}
$$

The coordinate space part of this expression is now just the integral of a function 'f' of $\vec{X}_{\mathrm{CM}}$:

$$
\frac{1}{2\pi^3}\int \mathrm{d}^3X \ \exp\left(-\vec{X}\frac{\partial}{\partial \vec{X}_{\mathrm{CM}}}\right) \mathrm{f}\,(\vec{X}_{\mathrm{CM}}) = \frac{1}{2\pi^3}\int \mathrm{d}^3X \ \mathrm{f}\,(\vec{X}_{\mathrm{CM}}-\vec{X}) \tag{2.92}
$$

which is equal to a constant. Therefore for the second of the two cases listed above, namely if the widths within each cluster are the same, but the clusters' widths are different, the intrinsic, centre of mass and relative motions can still all be decoupled.

In the third case listed above with different widths for each cluster, and in general each nucleon, there can be no decoupling of equation (2.87), although the coupling can be reduced by projection as was performed above. The effect that this residual coupling has on the results for example in the S-factor is still a matter for investigation, but its effect can be observed in spurious oscillations that appear in the phase shifts, see for example the $\frac{1}{2}^{+}$ and $\frac{3}{2}+$ phase shifts in figure 4.6.

2.3.5. Imposing boundary conditions

In the FMD model space the relative wave function can only be constructed at discrete distance intervals, the spacing of which is determined by:

- The desire to describe the wave function correctly, meaning the states cannot be too far apart
- Avoiding linear dependencies between the states, meaning they cannot be too close together

as was mentioned in section 2.3.1. The requirement is therefore to solve a second order differential equation, the Schrödinger equation, on a grid. Solving the equation for two point charges on a grid would lead to there being one off-diagonal matrix element, thus requiring one extra boundary condition, in addition to specifying that the wave function be equal to zero at the origin.

$$\left|\, \Psi; J^\pi M \,\right\rangle = \sum_{a=1}^{n_{\mathrm{IN}}} \sum_{\kappa_a=1}^{n_{\mathrm{G}a}} \psi_{a\kappa_a} \left|\, Q^{(a)}; J^\pi M \kappa_a \,\right\rangle + \sum_{b=n_{\mathrm{IN}+1}}^{n_{\mathrm{IN}}+n_{\mathrm{BC}}} \sum_{\kappa_b=1}^{n_{\mathrm{G}a}} \psi_{b\kappa_b} \left|\, Q^{(b)}; J^\pi M \kappa_b \,\right\rangle \tag{2.93}$$

Imposing boundary conditions requires the connection of the many-body nuclear system, with its many degrees of freedom, to the asymptotic 'point charge world' which is the correct description when the two nuclei are a large distance apart and the relative distance is the only degree of freedom. The two required boundary conditions are normally that the wave function must go to zero at the origin and that the logarithmic derivative of the wave function $\frac{u'(r)}{u(r)}$, where $u'(r) = \frac{du(r)}{dr}$, matches the Coulomb wave function at a chosen matching point outside the range of the nuclear potential.

In FMD however there is the added complication that the basis states are not orthogonal. This causes the Hamiltonian to connect frozen states in which the clusters are positioned at different relative distances. This effect can be seen by the non-negligible off-diagonal matrix elements of the Hamiltonian and overlap matrices. A plot of the value of the matrix elements of a cut across the Hamiltonian matrix at the matching point of 13 fm is shown in figure 2.8. In this

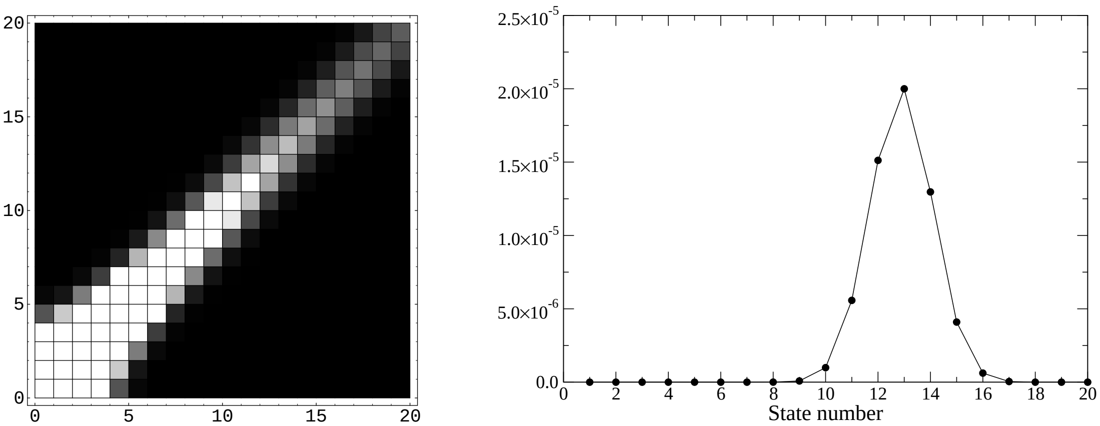

Figure 2.8.: On the left is shown a density plot of the absolute values of the matrix elements of the Hamiltonian, with the lighter colours corresponding to higher values. On the right is a cut across the matrix elements of the Hamiltonian for the 13^{th} state, showing that the peak is built of about 8 points meaning that there are 4 off-diagonal matrix elements. The line is merely meant as a guide to the eye.

case the state number and matching point coincide as only frozen states were used and they were spaced apart in 1 fm intervals, consequently the 13^{th} state has the largest matrix element in the cut. In the code the number of boundary conditions required is determined by counting how many states build the peak, the boundaries of the peak are determined by requiring the matrix elements at either edge of the peak in the cut to be the first states to drop to $\frac{1}{100}^{th}$ of the peak value. On this basis the peak consists of 8 states, therefore there are 4 off-diagonal matrix elements and hence this is the number of boundary conditions that would be used.

The fact that the Hamiltonian and overlap matrices have this band diagonal structure shows why the deviation of the relative distance measure at the edges of the Hilbert space for the 1.0 fm spacing in figure 2.7 is not a problem. If the matching point is sensibly chosen and the Hilbert space has enough frozen states to properly localise the state then it is only the n_{BC} states to either side of the matching point that must have a good relative distance representation, as beyond that the matrix elements go to zero.

Matching at a single point would lose the coupling between these four states beyond the matching point that the overlap and Hamiltonian matrices connect to, and therefore the interior and exterior wave functions would not be properly joined. To perform the matching correctly it is necessary to match the wave functions at as many points as there are non-negligible off-diagonal matrix elements in the Hamiltonian as demonstrated above, so as not to lose the aforementioned couplings. Equivalently, rather than matching the wave functions at a number of relative distances, the same number of derivatives of the wave functions can be matched at a single relative distance. This principle is illuminated by the following equation:

$$\frac{\left\langle B;i \,\middle|\, \left[\underset{\sim}{H}^{\mathrm{F}} , \underset{\sim}{B}^{\mathrm{F}}\right]^{s} \,\middle|\, \Psi; J^{\pi}M \right\rangle}{\left\langle B;i \,\middle|\, \Psi; J^{\pi}M \right\rangle} \overset{!}{=} \frac{\left\langle r_i \,\middle|\, \left[\frac{1}{2\mu}\left(-\frac{d^2}{dr^2}+\frac{\ell(\ell+1)}{r^2}\right)+\frac{Z_1Z_2e^2}{r} , b(r_i)\right]^{s} \,\middle|\, u \right\rangle}{\left\langle r_i \,\middle|\, u \right\rangle} \qquad s = 1, \ldots, n_{\mathrm{BC}} \, . \tag{2.94}$$

The left hand side gives the derivative of the many-body FMD wave function from the commutator of the relative distance operator and the Hamiltonian in the frozen subspace. The right hand side gives the derivative of the Coulomb wave function at relative distances r_i corresponding to the i^{th} eigenvalue of the $\underset{\sim}{B}$ operator b_i. Taking up to the ${n_{\mathrm{BC}}}^{th}$ power of these commutators supplies the n_{BC} linearly independent equations required to perform the matching.

As already mentioned, the distance at which matching should be performed must be sensibly chosen. This is important because the matching point must not be too close, meaning it must be outside the range of the nuclear potential and polarisation by a strong Coulomb field. However it must also not be too far out as the edge of the Hilbert space, just beyond the last frozen state, must not curtail the localisation of the state at the matching point. Examples of these two eventualities, as well as a good choice of matching point, are illustrated in figure 2.9. It can be clearly seen from figure 2.9 that the only case out of the three shown in which the localised state is properly localised is if the matching point is chosen to be 13 fm. In the case of a 5 fm matching point and an 18 fm matching point, the localisation of the state is obviously hampered due to the edge of the model space preventing the required overlaps from being available. The localisation in the case of 5 fm is not as bad as that for 18 fm, however, it must be borne in mind that there are other severe problems with perform the matching at such a small relative distance. The whole previous discussion about the collective coordinate representation and the measure of the relative distance relied on the clusters being well separated, for a relative distance of 5 fm, the ^{14}C and ^{4}He clusters considered in the figure will already have a non-negligible overlap. Therefore although the localisation of the state does not look too bad, 5 fm would also not be a good choice of matching point.

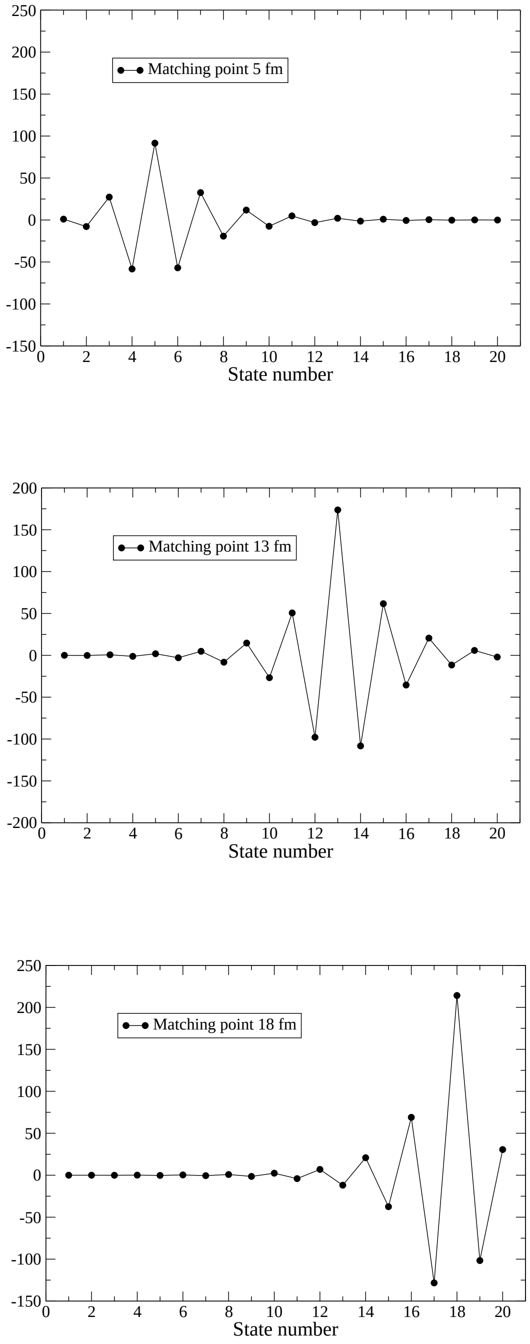

Figure 2.9.: The eigenstate of the relative distance operator, a state localised in the relative distance. The model space extends to clusters whose centres of mass are separated by 20 fm. System is ^{14}C and ^{4}He. The lines are just meant as guides for the eye.

Derivatives of the wave function in the FMD model space

If the matching point is sensibly chosen, at the matching point and beyond the clusters no longer overlap. This allows the Hamiltonian and $\underset{\sim}{B}$ operator to be decomposed as follows:

$$\underset{\sim}{H}^{\mathrm{F}} = \underset{\sim}{H}_{\mathrm{REL}} + \underset{\sim}{H}_1 + \underset{\sim}{H}_2 \qquad \underset{\sim}{B}^{\mathrm{F}} = \underset{\sim}{B}_{\mathrm{REL}} + \underset{\sim}{B}_1 + \underset{\sim}{B}_2 \tag{2.95}$$

$\underset{\sim}{H}_1$ and $\underset{\sim}{H}_2$ are the intrinsic Hamiltonians of the separate clusters. $\underset{\sim}{H}_{\mathrm{REL}}$ is the Hamiltonian of the relative motion, which is composed of a kinetic energy and a potential energy component:

$$\underset{\sim}{H}_{\mathrm{REL}} = \underset{\sim}{T}_{\mathrm{REL}} + \underset{\sim}{V}_{\mathrm{REL}} \ . \tag{2.96}$$

Outside the range of the nuclear interaction the only forces acting on the clusters are the Coulomb and the centrifugal force. As they have no momentum dependence $[\underset{\sim}{V}_{\mathrm{REL}}, \underset{\sim}{B}_{\mathrm{REL}}] = 0$. Therefore using equation (2.95), the relative "velocity" $\dot{\underset{\sim}{B}}^{\mathrm{F}}$ is given by:

$$\dot{\underset{\sim}{B}}^{\mathrm{F}} = i[\underset{\sim}{H}^{\mathrm{F}}, \underset{\sim}{B}^{\mathrm{F}}] = i\left([\underset{\sim}{T}_{\mathrm{REL}}, \underset{\sim}{B}_{\mathrm{REL}}] + [\underset{\sim}{H}_1, \underset{\sim}{B}_1] + [\underset{\sim}{H}_2, \underset{\sim}{B}_2]\right) \tag{2.97}$$

As long as $\dot{\underset{\sim}{B}}^{\mathrm{F}}$ is being calculated for the frozen states, whose intrinsic degrees of freedom are frozen, the square radii of the clusters cannot change with time and hence:

$$\left\langle\, \Psi_1 \,\middle|\, [\underset{\sim}{H}_1, \underset{\sim}{B}_1] \,\middle|\, \Psi_1 \,\right\rangle = \left\langle\, \Psi_2 \,\middle|\, [\underset{\sim}{H}_2, \underset{\sim}{B}_2] \,\middle|\, \Psi_2 \,\right\rangle = 0 \ . \tag{2.98}$$

Thus when calculating $\dot{\underset{\sim}{B}}^{\mathrm{F}}$ in the frozen subspace, which is what will be done throughout this work, using (2.64) equation (2.97) can be written:

$$\dot{\underset{\sim}{B}}^{\mathrm{F}} = i[\underset{\sim}{H}^{\mathrm{F}}, \underset{\sim}{B}^{\mathrm{F}}] = i\mu_{\mathrm{A}}[\underset{\sim}{H}^{\mathrm{F}}, \underset{\sim}{r}^2] = \mu_{\mathrm{A}}\dot{\underset{\sim}{r}^2} \tag{2.99}$$

and the contributions from the clusters' intrinsic degrees of freedom vanish because they are stationary in time. Higher derivatives of $\dot{\underset{\sim}{B}}^{\mathrm{F}}$ are simply given by:

$$\left(\dot{\underset{\sim}{B}}^{\mathrm{F}}\right)^s = i^s[\underset{\sim}{H}^{\mathrm{F}}, \underset{\sim}{B}^{\mathrm{F}}]^s \qquad s = 1, \ldots, n_{\mathrm{BC}} \tag{2.100}$$

or in matrix representation by:

$$\dot{\mathsf{B}} = i\left(\mathsf{H}^{\mathrm{F}} \cdot \mathsf{O}^{\mathrm{F}} \cdot \mathsf{B} - \mathsf{B} \cdot \mathsf{O}^{\mathrm{F}} \cdot \mathsf{H}^{\mathrm{F}}\right) \qquad \left(\dot{\mathsf{B}}\right)^s = i^s\, \dot{\mathsf{B}} \cdot \left(\mathsf{O}^{\mathrm{F}} \cdot \dot{\mathsf{B}}\right)^{(s-1)} \tag{2.101}$$

where the overlap matrix O^{F} is required because the FMD basis states are not orthogonal. The situation is actually somewhat more complicated as $\dot{\underset{\sim}{B}}$ and its powers are calculated in the subspace of frozen states as seen from equation (2.101), however the scattering state $\big|\, k; J^\pi M \,\big\rangle$ is defined in the full space including the interaction states as well as the frozen states. To resolve this, a projection operator can be defined which projects operators onto the space spanned by the frozen states:

$$\underset{\sim}{1}^{\mathrm{F}} = \sum_{\substack{a\in\mathrm{F}\\ b\in\mathrm{F}}}^{n_{\mathrm{F}}} \big|\, Q^{(a)}; J^\pi M\; K{=}J \,\big\rangle O_{ab} \big\langle\, Q^{(b)}; J^\pi M\; K{=}J \,\big| \,, \tag{2.102}$$

this is nothing but the identity operator in the non-orthogonal basis spanned by the frozen states. Using the aforementioned projector with an arbitrary operator $\underset{\sim}{A}$:

$$\begin{aligned}\underset{\sim}{A}^{\mathrm{F}} &= \sum_{\substack{a\in\mathrm{F}\\ b\in\mathrm{F}}}^{n_{\mathrm{F}}} \sum_{\substack{c\in\mathrm{F}\\ d\in\mathrm{F}}}^{n_{\mathrm{F}}} \big|\, Q^{(a)}; K \,\big\rangle O_{ab} \big\langle\, Q^{(b)}; K \,\big|\, \underset{\sim}{A} \,\big|\, Q^{(c)}; K \,\big\rangle O_{cd} \big\langle\, Q^{(d)}; K \,\big| \\ &= \sum_{\substack{a\in\mathrm{F}\\ b\in\mathrm{F}}}^{n_{\mathrm{F}}} \sum_{\substack{c\in\mathrm{F}\\ d\in\mathrm{F}}}^{n_{\mathrm{F}}} \big|\, Q^{(a)}; K \,\big\rangle O_{ab} A_{bc} O_{cd} \big\langle\, Q^{(d)}; K \,\big| \,,\end{aligned} \tag{2.103}$$

gives the operator in the frozen subspace. This method will be required in matching the FMD many-body world to the 'point charge world'. The boundary condition equation that must be satisfied to complete the matching to the Coulomb wave function is therefore given by:

$$\frac{\big\langle\, B; j \,\big|\, i[\underset{\sim}{H}^{\mathrm{F}}, \underset{\sim}{B}^{\mathrm{F}}]^s \,\big|\, k; J^\pi M \,\big\rangle}{\big\langle\, B; j \,\big|\, k; J^\pi M \,\big\rangle} = \mu_{\mathrm{A}}^s \frac{\big\langle\, r_j \,\big|\, i[\underset{\sim}{H}, \underset{\sim}{r}^2]^s \,\big|\, u; k\, \ell \,\big\rangle}{\big\langle\, r_j \,\big|\, u; k\, \ell \,\big\rangle} \,, \tag{2.104}$$

where $u(r_j) = \big\langle\, r_j \,\big|\, u; k\, \ell \,\big\rangle$ is the Coulomb wave function at the relative distance given by using equation (2.64) on the j^{th} eigenvalue of $\underset{\sim}{B}$. The factor of μ_{A}^s comes from equation (2.64).

To perform the matching, a method to calculate the commutators $[\underset{\sim}{H}, \underset{\sim}{r}^2]^s$ must be devised. This method is straightforward but lengthy and is therefore presented in appendix A.1.

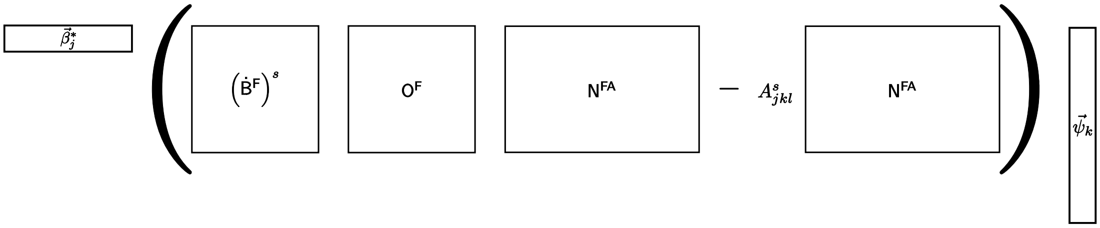

Figure 2.10.: Graphical representation of equation (2.109). The matrices show how the overlap matrix N^{FA} connects the smaller frozen space to the larger space including the interaction states.

Matching the internal and external wave functions

The equation for the matching is (2.104), which can be rearranged to give:

$$\begin{aligned} \frac{\langle B; j \,|\, i[\underset{\sim}{H}^{\mathrm{F}}, \underset{\sim}{B}^{\mathrm{F}}]^s \,|\, k; J^\pi M \rangle}{\langle B; j \,|\, k; J^\pi M \rangle} &= \mu^s_{\mathrm{A}} \frac{\langle r_j \,|\, i[\underset{\sim}{H}, \underset{\sim}{r}^2]^s \,|\, u; k\,\ell \rangle}{\langle r_j \,|\, u; k\,\ell \rangle} := A^s_{jk\ell} \\ \langle B; j \,|\, \left(\dot{\underset{\sim}{B}}^{\mathrm{F}}\right)^s \,|\, k; J^\pi M \rangle &= A^s_{jk\ell} \langle B; j \,|\, k; J^\pi M \rangle \end{aligned} \tag{2.105}$$

Expanding $\langle B; j \,|$ and $|\, k; J^\pi M \rangle$ in the basis states from (2.36) gives:

$$\begin{aligned} &\langle B; j \,|\, \left(\dot{\underset{\sim}{B}}^{\mathrm{F}}\right)^s \,|\, k; J^\pi M \rangle \\ &\quad = \sum_{a\in \mathrm{F}}^{n_{\mathrm{F}}} \sum_{b \in \mathrm{All}}^{n} \sum_{\kappa_b=1}^{n_{\mathrm{G}_b}} \beta^{(a)*}_j \langle Q^{(a)}; J^\pi M\ K{=}J \,|\, \left(\dot{\underset{\sim}{B}}^{\mathrm{F}}\right)^s \,|\, Q^{(b)}; J^\pi M \kappa_b \rangle \psi^{(b)}_{k\kappa_b} \,. \end{aligned} \tag{2.106}$$

$\dot{\underset{\sim}{B}}^{\mathrm{F}}$ operates only on the frozen states, but the scattering state $|\, k; J^\pi M \rangle$ is defined in both the interaction and frozen space, therefore the projector from (2.102) is inserted between $\dot{\underset{\sim}{B}}^{\mathrm{F}}$ and the scattering state:

$$\begin{aligned} &\langle B; j \,|\, \left(\dot{\underset{\sim}{B}}^{\mathrm{F}}\right)^s \,|\, k; J^\pi M \rangle \\ &\quad = \sum_{a,b,c\in \mathrm{F}}^{n_{\mathrm{F}}} \sum_{d \in \mathrm{All}}^{n} \sum_{\kappa_d=1}^{n_{\mathrm{G}_d}} \beta^{(a)*}_j \langle Q^{(a)}; J^\pi M\ K{=}J \,|\, \left(\dot{\underset{\sim}{B}}^{\mathrm{F}}\right)^s \,|\, Q^{(b)}; J^\pi M\ K{=}J \rangle \\ &\qquad\qquad \times O^{\mathrm{F}}_{bc} \langle Q^{(c)}; J^\pi M\ K{=}J \,|\, Q^{(d)}; J^\pi M \kappa_d \rangle \psi^{(d)}_{k\kappa_d} \,. \end{aligned} \tag{2.107}$$

Going through the same process for the right hand side of (2.105) gives:

$$
\begin{aligned}
&A^s_{jk\ell}\big\langle\, B; j \,\big|\, k; J^\pi M \,\big\rangle \\
&\quad = A^s_{jk\ell} \sum_{a\in\mathrm{F}}^{n_\mathrm{F}} \sum_{b\in\mathrm{All}}^{n} \sum_{\kappa_b=1}^{n_{\mathrm{G}_b}} \beta_j^{(a)*} \big\langle\, Q^{(a)}; J^\pi M\ K{=}J \,\big|\, \Big(\dot{\underset{\sim}{B}}^{\mathrm{F}}\Big)^s \,\big|\, Q^{(b)}; J^\pi M \kappa_b \,\big\rangle \psi^{(b)}_{k\kappa_b} \\
&\qquad = A^s_{jk\ell} \sum_{a,b,c\in\mathrm{F}}^{n_\mathrm{F}} \sum_{d\in\mathrm{All}}^{n} \sum_{\kappa_d=1}^{n_{\mathrm{G}_d}} \beta_j^{(a)*} \big\langle\, Q^{(a)}; J^\pi M\ K{=}J \,\big|\, \Big(\dot{\underset{\sim}{B}}^{\mathrm{F}}\Big)^s \,\big|\, Q^{(b)}; J^\pi M\ K{=}J \,\big\rangle \\
&\qquad\qquad\qquad\qquad \times O^{\mathrm{F}}_{bc} \big\langle\, Q^{(c)}; J^\pi M\ K{=}J \,\big|\, Q^{(d)}; J^\pi M \kappa_d \,\big\rangle \psi^{(d)}_{k\kappa_d}\ .
\end{aligned}
\tag{2.108}
$$

Thus (2.105) can be written in matrix form as:

$$
\vec{\beta}_j^{\dagger} \left(\left(\dot{\mathsf{B}}^{\mathsf{F}} \right)^s \cdot \mathsf{O}^{\mathsf{F}} \cdot \mathsf{N}^{\mathsf{FA}} - A^s_{jk\ell} \mathsf{N}^{\mathsf{FA}} \right) \vec{\psi}_k = 0 \qquad s = 1, \ldots, n_{\mathrm{BC}}\ , \tag{2.109}
$$

where $\mathsf{N}^{\mathsf{FA}} = \big\{ \big\langle\, Q^{(a)}; J^\pi M\ K{=}J \,\big|\, Q^{(b)}; J^\pi M \kappa_b \,\big\rangle \big\}$ which is the overlap between the frozen basis states and the set of all frozen and interaction states (F=Frozen, A=All). A more vivid depiction of equation (2.109) is given in figure 2.10 where boxes are used to represent the vectors and matrices from (2.109).

Equation (2.109) is a set of n_{BC} linearly independent equations, each one corresponding to a power of s. These n_{BC} linear equations form an under-complete set which enable n_{BC} coefficients outside the matching point to be expressed in terms of the n_{IN} ones inside using equation (2.93). If an example with $n_{\mathrm{BC}} = 4$ is taken, then Equation (2.109) gives a matrix of the form:

$$
\left(\begin{array}{cccc|ccc|cc}
c_{11} & c_{12} & \cdots & c_{1n_{\mathrm{IN}}} & c_{1n_{\mathrm{IN}}+1}\psi_{n_{\mathrm{IN}}+1} & \cdots & c_{1n_{\mathrm{IN}}+n_{\mathrm{BC}}} & \cdots & c_{1n_{\mathrm{G}}} \\
c_{21} & c_{22} & \cdots & c_{2n_{\mathrm{IN}}} & c_{2n_{\mathrm{IN}}+1}\psi_{n_{\mathrm{IN}}+1} & \cdots & c_{2n_{\mathrm{IN}}+n_{\mathrm{BC}}} & \cdots & c_{2n_{\mathrm{G}}} \\
c_{31} & c_{32} & \cdots & c_{3n_{\mathrm{IN}}} & c_{3n_{\mathrm{IN}}+1}\psi_{n_{\mathrm{IN}}+1} & \cdots & c_{3n_{\mathrm{IN}}+n_{\mathrm{BC}}} & \cdots & c_{3n_{\mathrm{G}}} \\
c_{41} & c_{42} & \cdots & c_{4n_{\mathrm{IN}}} & c_{4n_{\mathrm{IN}}+1}\psi_{n_{\mathrm{IN}}+1} & \cdots & c_{4n_{\mathrm{IN}}+n_{\mathrm{BC}}} & \cdots & c_{4n_{\mathrm{G}}}
\end{array} \right)
\left(\begin{array}{c}
\psi_1 \\ \psi_2 \\ \vdots \\ \psi_{n_{\mathrm{IN}}} \\ \hline \psi_{n_{\mathrm{IN}}+1} \\ \vdots \\ \psi_{n_{\mathrm{IN}}+n_{\mathrm{BC}}} \\ \hline \vdots \\ \psi_{n_{\mathrm{G}}}
\end{array} \right) = 0
\tag{2.110}
$$

where the part between the vertical bars contains the coefficients related to the boundary condition states, for this example four boundary conditions have been chosen and hence the part between the bars forms a 4 × 4 submatrix. By a series of linear operations consisting of multiplying and subtracting rows from one another, this system of equations can be rearranged into the form:

$$\left(\begin{array}{cccc|cccc|cc} d_{11} & d_{12} & \dots & d_{1n_{\mathrm{IN}}} & 1 & 0 & 0 & 0 & \dots & d_{1n_{\mathrm{G}}} \\ d_{21} & d_{22} & \dots & d_{2n_{\mathrm{IN}}} & 0 & 1 & 0 & 0 & \dots & d_{2n_{\mathrm{G}}} \\ d_{31} & d_{32} & \dots & d_{3n_{\mathrm{IN}}} & 0 & 0 & 1 & 0 & \dots & d_{3n_{\mathrm{G}}} \\ d_{41} & d_{42} & \dots & d_{4n_{\mathrm{IN}}} & 0 & 0 & 0 & 1 & \dots & d_{4n_{\mathrm{G}}} \end{array}\right) \left(\begin{array}{c} \psi_1 \\ \psi_2 \\ \vdots \\ \psi_{n_{\mathrm{IN}}} \\ \hline \psi_{n_{\mathrm{IN}}+1} \\ \vdots \\ \psi_{n_{\mathrm{IN}}+n_{\mathrm{BC}}} \\ \hline \vdots \\ \psi_{n_{\mathrm{G}}} \end{array}\right) = 0 \quad (2.111)$$

By simply moving this central block of the matrix to the other side of the equation, each line gives an expression for one of the $\psi_{n_{\mathrm{IN}+1}}$ up to $\psi_{n_{\mathrm{IN}}+n_{\mathrm{BC}}}$.

$$\begin{pmatrix} -d_{11} & -d_{12} & \dots & -d_{1n_{\mathrm{IN}}} & -d_{1n_{\mathrm{IN}}+n_{\mathrm{BC}}+1} & \dots & -d_{1n_{\mathrm{G}}} \\ -d_{21} & -d_{22} & \dots & -d_{2n_{\mathrm{IN}}} & -d_{1n_{\mathrm{IN}}+n_{\mathrm{BC}}+1} & \dots & -d_{2n_{\mathrm{G}}} \\ -d_{31} & -d_{32} & \dots & -d_{3n_{\mathrm{IN}}} & -d_{1n_{\mathrm{IN}}+n_{\mathrm{BC}}+1} & \dots & -d_{3n_{\mathrm{G}}} \\ -d_{41} & -d_{42} & \dots & -d_{4n_{\mathrm{IN}}} & -d_{1n_{\mathrm{IN}}+n_{\mathrm{BC}}+1} & \dots & -d_{4n_{\mathrm{G}}} \end{pmatrix} \begin{pmatrix} \psi_1 \\ \psi_2 \\ \vdots \\ \psi_{n_{\mathrm{IN}}} \\ \psi_{n_{\mathrm{IN}}+n_{\mathrm{BC}}+1} \\ \vdots \\ \psi_{n_{\mathrm{G}}} \end{pmatrix} = \begin{pmatrix} \psi_{n_{\mathrm{IN}}+1} \\ \psi_{n_{\mathrm{IN}}+2} \\ \psi_{n_{\mathrm{IN}}+3} \\ \psi_{n_{\mathrm{IN}}+n_{\mathrm{BC}}} \end{pmatrix}$$

(2.112)

The first matrix on the left of equation (2.112) therefore serves as a transformation matrix to give the n_{BC} coefficients of the wave function outside the matching point using those inside. This matrix is denoted by S and the relation can be written much more concisely as:

$$\sum_{j=1}^{n_{\mathrm{IN}}} \mathsf{S}_{ij}\psi_j + \sum_{k=n_{\mathrm{IN}}+n_{\mathrm{BC}}+1}^{n_{\mathrm{G}}} \mathsf{S}_{ik}\psi_k = \psi_{n_{\mathrm{IN}}+i} \qquad i = 1, \dots, n_{\mathrm{BC}}\ . \quad (2.113)$$

In the last sections methods for calculating both $\left(\underset{\sim}{\dot{B}}\right)^s$ and $A^s_{jk\ell}$ were derived and hence using S, the boundary conditions can now be imposed on the Hamiltonian and overlap matrices. This will then enable an eigenvalue problem with the modified Hamiltonian and overlap matrices to be solved that will have the boundary conditions built into it.

Imposing the boundary conditions on the Hamiltonian and overlap matrices forms a new eigenvalue problem given by:

$$\sum_{j=1}^{n_{\mathrm{IN}}}\left(\mathsf{H}_{ij}+\sum_{k=n_{\mathrm{IN}}+1}^{n_{\mathrm{IN}}+n_{\mathrm{BC}}}\mathsf{H}_{ik}\mathsf{S}_{kj}\right)\psi_j = E\sum_{j=1}^{n_{\mathrm{IN}}}\left(\mathsf{N}_{ij}+\sum_{k=n_{\mathrm{IN}}+1}^{n_{\mathrm{IN}}+n_{\mathrm{BC}}}\mathsf{N}_{ik}\mathsf{S}_{kj}\right)\psi_j \quad i=1,\ldots,n_{\mathrm{IN}}$$

$$\Rightarrow \mathsf{H}_{\mathrm{BC}}\,\vec{\psi} = E\,\mathsf{N}_{\mathrm{BC}}\,\vec{\psi}\,. \tag{2.114}$$

Solving this eigenvalue problem then delivers the eigenvectors $\vec{\psi}$ appropriate to whatever boundary conditions were imposed. In our case, the aim is to describe three different physical scenarios which each have different boundary conditions, these are covered in the next subsection.

2.3.6. Boundary conditions for different physical scenarios

The boundary conditions of course depend on the physical situation that is to be described, in terms of the previous section, this corresponds to changing the values of the $A^s_{jk\ell}$ in (2.109).

The three physical situations are:

- Bound states
- Resonant states
- Non-resonant states

Bound states

In the case of bound states, the energy of the state lies below the threshold for particle emission. This means that the wave function of the state penetrates some distance into the Coulomb (and centrifugal for $\ell \neq 0$) barrier and goes to zero at some point under this barrier. As the energy E is negative with respect to the threshold for particle emission, $k = \sqrt{-2\mu E}$ and the time-independent Schrödinger equation (A.12) is accordingly modified and now reads:

$$\frac{d^2}{d\rho^2}\,u(\rho) = \left(\frac{\ell\,(\ell+1)}{\rho^2}+\frac{2\eta}{\rho}+1\right)u(\rho)\,. \tag{2.115}$$

The two independent functions that solve this equation are known as the Whittaker functions [1]:

$$u(\rho) = AW_{-\eta,\ell+1/2}(2\rho)/\rho \tag{2.116}$$

where A is a constant. Whittaker functions of the first kind diverge at infinity, therefore in the description of bound states the second kind that tends to zero at infinity is the appropriate one. However, the second kind of Whittaker function diverges at the origin. This highlights the fact that the bound state wave function is only equivalent to the Whittaker function in the asymptotic region where the nuclear potential is zero and only the Coulomb and centrifugal forces contribute to the potential. This was a requirement in writing the Hamiltonian in the form of (A.1) which was then used to derive (A.12). The attractive part of the nuclear interaction causes the bound state wave function to be bent over and diverge from the Whittaker function at small distances, as is illustrated schematically by the red dashed line in figure 2.11.

An often used approximation in finding the bound states of a nucleus is the so-called bound state approximation, this simply means that a bound state is described up to some distance by the states spanning the model space, beyond that the wave function is by construction set to zero as there are no more states. As the total probability density must remain equal to unity due to normalisation, this effectively squeezes some of the density back into the interaction region and hence deforms the wave function in this region. If the amplitude of the wave function at the edge of the model space is small in comparison to that in the interaction region this is a good approximation as the deformation will be small in comparison to the overall amplitude. However, the Coulomb potential tends to zero very slowly with distance as it is proportional to $\frac{1}{r}$. This allows the wave function of a bound state located at an energy close to the particle emission threshold to tunnel to very large distances whilst remaining under the Coulomb barrier. There are obviously computational limits to how large the model space can be made, in this situation the wave function will still have sizeable coefficients at the edge of the model space. Thus the bound state approximation is no longer valid as the deformation to the wave function in the interaction region becomes too great. To resolve this, the wave function in the interaction region found using FMD must be matched to the Whittaker function to describe its tail correctly.

In this thesis the bound state approximation is used in the description of the bound states. However, in the future it should be simple to implement a procedure similar to that for finding the resonant states to make use of the appropriate Whittaker function in describing sub-threshold resonances and the tails of bound states in general.

Resonant states

A resonant state is an excited metastable state of a nucleus located above the threshold for particle emission. In capture reactions, it is formed by the fusion of a projectile and a target nucleus that have the correct relative kinetic energy and quantum numbers to form the resonant state in the compound nucleus. This resonant state lives for a certain time, which is inversely proportional to the resonance width, and then decays by emitting a photon into a state of lower energy.

One widely used method for describing narrow resonances was developed by Gamow to explain α-decay in heavy nuclei [17]. This process required a quantum mechanical explanation as in a classical picture the α-particle is too strongly bound by the deep potential well of the parent nucleus and therefore can never escape to decay. Gamow was able to show using a model potential that there was a finite probability for the α-particle to tunnel through the Coulomb barrier and be emitted from the parent nucleus. Gamow's method starts from the point when the resonance is formed and then describes the time evolution of the system. Over time, the probability flux that is initially contained within the range of the nuclear potential slowly leaks, corresponding to the probability that the resonant state might decay. The crucial point is the assumption that for a narrow resonance, the wave function can be written as:

$$u_\ell(r,t) \approx u_\ell(r) \exp\left(-\frac{\Gamma}{2}t - iE_{\mathrm{R}}t\right) = u_\ell(r) \exp\left(-izt\right) , \tag{2.117}$$

where E_{R} is the resonance energy, Γ is its width and z is the complex eigenvalue found from solving the Schrödinger equation with the appropriate boundary conditions. This corresponds to the leakage rate ($\frac{\text{flux}}{\text{density inside}}$) being constant. If the resonance is narrow the flux will be small, and the hypothesis from equation (2.117) that the wave function is essentially stationary over time apart from a gradual decrease in the amplitude, should be a good approximation.

The radial part of the time-dependent Schrödinger equation for an orbital angular momentum ℓ is:

$$\left(-\frac{\partial^2}{\partial r^2} + \frac{\ell(\ell+1)}{r^2} + V_C(r) + V_N(r)\right) u_\ell(r,t) = i2\mu \frac{\partial}{\partial t} u_\ell(r,t) , \tag{2.118}$$

where $V_C(r)$ and $V_N(r)$ are the Coulomb and nuclear potentials respectively. From this the continuity equation:

$$\frac{1}{\mu} \operatorname{Im}\left\{ u_\ell^*(R,t) \frac{\partial u_\ell}{\partial r}(R,t) \right\} = -\frac{d}{dt} \int_0^R dr \, |u_\ell(r,t)|^2 \tag{2.119}$$

can be obtained. This expresses the fact that the rate of decrease of probability density inside a surface at radius R must be equal to the probability flux through the same surface. The initial condition of a narrow resonance can be approximated as a very lightly bound state, which will solve a real eigenvalue problem and deliver a real energy. If the potential well is made slightly shallower, there will be a small probability for the particles to tunnel out of the well and the eigenvalue problem and eigenvalue will become complex. At the resonance energy a large increase in the cross section is often observed and the phase shift changes rapidly, as can be seen for example in figure 4.3.

After a short time interval the time-dependent solution of (2.118) will come to a steady state and the shape of the wave function inside the barrier will remain virtually unchanged with its amplitude slowly decreasing as a small steady flux leaks out through the barrier. The flux beyond the barrier rises exponentially up to a point where it drops to zero. The exponential rise is caused by the flow rate being highest when the density inside is greatest, which is at time zero when the flux begins to leak out. As the density inside decreases, so does the flow rate out through the barrier, in accordance with equation (2.119). This is consistent with the leakage rate being constant. The cutoff in the flux beyond the barrier occurs at the distance equal to the initial flow velocity multiplied by the time elapsed, as this is the furthest point the wave can have propagated in the elapsed time.

In the case of a narrow resonance, the flow of the probability through the barrier is slow and the shape of the wave function therefore remains effectively constant inside. Hence the decay rate:

$$\Gamma_\ell = \frac{\frac{1}{\mu}\,\mathrm{Im}\left\{u_\ell^*(R,t)\frac{\partial u_\ell}{\partial r}(R,t)\right\}}{\int_0^R dr\; |u_\ell(r,t)|^2} = \frac{\text{flux through surface at R}}{\text{probability to be inside}} \tag{2.120}$$

can be well approximated as being time-independent. The FMD model can be used to calculate the appropriate state inside the barrier, this FMD state can then be matched to the appropriate boundary conditions as described in section 2.3.5. From the last paragraph it is clear that a purely outgoing wave gives the correct boundary conditions for Gamow's method, a purely outgoing Coulomb wave function is given by:

$$u_\ell(\eta,\rho) = G_\ell(\eta,\rho) + iF_\ell(\eta,\rho)\ , \tag{2.121}$$

where F_ℓ and G_ℓ are the regular and irregular (or logarithmic) Coulomb functions, respectively [1].

Solving the eigenvalue problem (2.114) with the FMD wave function matched to a purely outgoing Coulomb wave function will deliver n_{IN} complex eigenvalues. Somehow we need to iterate over the energy to find the fixed point(s) in the complex energy plane. However as we have no a priori knowledge of where the fixed points should lie, unless there is existing experimental data, there is a question of how to proceed. The method adopted is to always take the eigenvalue closest in the complex plane to the previous step as the next input in calculating the Coulomb coefficients $A^s_{k\ell j}$ and thereby the boundary conditions. Although there is no obvious physical reason to suggest that this is the best or most efficient method for locating the fixed points, it has the advantage that the iteration will proceed along the smoothest possible path and by the nature of the method, the step size should tend to decrease (unless all eigenvalues diverge from one another), meaning that the iteration tends to converge resulting in one of the fixed points being located. The fixed points are the eigenstates of the modified Hamiltonian that solve the Schrödinger equation with the correct boundary conditions of a purely outgoing wave and are therefore the solutions that we seek. The value of a fixed point on the complex plane can be written as $z = E_{\mathrm{R}} - i\Gamma/2$. The eigenvector ($\psi$ from (2.114)) is the Gamow vector that describes the resonance state.

The Coulomb wave functions F and G from equation (2.121) are uniquely determined by: the relative angular momentum of the system ℓ, the Sommerfeld parameter η and $\rho = kr$. The Sommerfeld parameter is given by $\eta = \mu\frac{Z_1 Z_2 e^2}{k}$ and the wave number $k = \sqrt{2\mu E}$ with μ the reduced mass of the system and E the relative kinetic energy of the clusters. An angular momentum of interest is chosen and a starting energy E and the matching point discussed in section 2.3.5, these quantities uniquely determine the form of the outgoing Coulomb wave. As the Gamow method is only appropriate for narrow resonances, it makes sense to select a starting energy close to, or located on, the real axis.

As shown in the next chapter, the solutions that are found are robust and therefore the method of procedure towards them is of little importance to the final result, excluding the possibility of missing a solution altogether. However, this possibility can easily be ruled out because the calculations proceed quickly enough that a grid of starting points can be constructed so as to verify the results.

Non-resonant states

In the case of non-resonant reactions the energy spectrum for the colliding nuclei is continuous as there is no well defined energy window within which they must interact in order to fuse. The equation to be solved in this case is (A.12). The asymptotic behaviour of the scattering state must be that of a superposition of an incoming and outgoing wave, the presence of the nuclear potential causes the outgoing wave to be shifted by a phase δ_ℓ. Therefore the FMD state must be matched to the Coulomb scattering state given by:

$$\begin{aligned} u_\ell(\eta,\rho) &= G_\ell(\eta,\rho) - iF_\ell(\eta,\rho) - e^{2i\delta_\ell}\left(G_\ell(\eta,\rho) + iF_\ell(\eta,\rho)\right) \\ &= I_\ell(\eta,\rho) - e^{2i\delta_\ell}\, O_\ell(\eta,\rho)\ , \end{aligned} \tag{2.122}$$

where $I_\ell(\eta,\rho)$ and $O_\ell(\eta,\rho)$ are the incoming and outgoing wave respectively, δ_ℓ is the nuclear phase shift and η is the Sommerfeld parameter given by $\eta = \mu\frac{Z_1 Z_2\, \alpha}{k}$, where α is the fine structure constant.

Looking at (2.122) it is clear that for a phase shift of zero, $u_\ell(\eta,\rho) = -2iF_\ell(\eta,\rho)$. However, at low energies $\rho = kr$ decreases, the irregular solution $G_\ell(\eta,\rho)$ increases rapidly (it is infinite at $\rho = 0$) and the regular solution $F_\ell(\eta, \rho)$ tends to zero. If equation (2.122) is then used to find the wave function for small phase shifts it can lead to numerical problems because $G_\ell(\eta, \rho)$ is so much greater than $F_\ell(\eta, \rho)$ that (2.122) will give a value that is numerically zero. To avoid this, (2.122) is rearranged using trigonometric identities and employed in the code in the following form:

$$u_\ell(\eta, \rho) = -2i \left[F_\ell(\eta, \rho) + (G_\ell(\eta, \rho) + iF_\ell(\eta, \rho)) e^{i\delta_\ell} \sin(\delta_\ell) \right] \ . \tag{2.123}$$

This equation is numerically more stable than (2.122) for the combination of low scattering energies and phase shifts close to zero.

In contrast to the resonant states of the last subsection, the required energy of the scattering state is known, however the correct phase shift is not, nor is the form of the scattering state. Altering the phase shift changes $A^s_{jk\ell}$ in equation (2.109), meaning that solving (2.114) yields a different scattering state $\vec{\psi}$. However, until the correct phase shift is found, the scattering state $\vec{\psi}$ will not satisfy equation (2.114) for the required energy E. Therefore the phase shift is iterated over until a scattering state is found that makes (2.114) consistent. To be more precise, in the code this is actually treated as a minimisation problem. From solving (2.114), n_{IN} eigenvalues E and eigenvectors $\vec{\psi}$ are obtained, the eigenvalue that is closest to the required scattering energy and its corresponding eigenvector are returned to a minimisation routine. The minimisation routine then varies the phase shift in an optimal way in order to minimise the difference between the closest eigenvalue returned by solving (2.114) and the required scattering energy.

The implementation of the Brent routine from Numerical Recipes [15] is used to perform the minimisation. Looking at equation (2.122), it can be seen that as $I_\ell(\eta, \rho)$ and $O_\ell(\eta, \rho)$ do not depend on δ_ℓ, the Coulomb scattering solution $u_\ell(\eta, \rho)$ for a particular η, ρ and ℓ is a periodic function with a period of π (as the outgoing solution $O_\ell(\eta, \rho)$ must be non-zero to describe a scattered wave). This simplifies the minimisation problem as the limits between which the minimum must be sought are known.

2.4. Calculating capture cross sections

The main nuclear physics input in the study of astrophysical reactions is the cross section for a reaction to occur across a range of energies. Most quantities of astrophysical interest for stellar evolution and element nucleosynthesis require knowledge of the reaction rate per particle pair $\langle \sigma v \rangle$ [35], which depends on the cross section $\sigma(E)$:

$$\langle \sigma v \rangle = \left(\frac{8}{\pi \mu} \right)^{\frac{1}{2}} \frac{1}{(kT)^{\frac{3}{2}}} \int_0^\infty \sigma(E) E \exp\left(-\frac{E}{kT} \right) dE \ , \tag{2.124}$$

where μ is the reduced mass, E is the relative kinetic energy in the centre of mass frame and T is the temperature.

The contributions to astrophysical radiative capture reactions mediated by the strong nuclear force can generally be divided into three types:

- Non-resonant
- Resonant
- Subthreshold resonances

Not all of these will have a significant contribution in every astrophysical scenario and reaction and often there will be overlap and interference of contributions from more than one of the above. It is the job of nuclear physics to quantitatively assess the contribution that each of them makes to a particular reaction rate. The non-resonant component is relevant for all the reactions considered in this thesis and hence the theory and method behind it will be covered here.

2.4.1. Calculation of non-resonant contribution

As stated in the introduction, the typical temperature in a stellar burning environment is between 10^7 and 10^9 K, corresponding to a peak in the distribution of the kinetic energy of the nuclei at approximately 1 to 100 keV. Depending on the charges of the nuclei involved, this often means that the colliding nuclei must tunnel a long way through the Coulomb barrier to fuse. Reactions for which the classical turning point is much greater than the nuclear radius are termed peripheral reactions [27]. In this type of reaction, which is common in astrophysics, the tunnelling probability falls off exponentially as the energy decreases. Therefore the cross section for capture also drops off rapidly below the Coulomb barrier, as can be seen in figure 4.7. As one of the aims of theoretical astrophysics is to extrapolate to astrophysical energies which are so low they cannot presently be attained in the laboratory, the S-factor is defined so as to suppress the energy dependence of the rapidly changing cross section and hence allow more reliable extrapolation to astrophysical energies. It is defined by:

$$S(E) = \sigma(E) E e^{2\pi\eta} \ , \tag{2.125}$$

Using this definition, equation (2.124) can be rewritten in the form:

$$\langle \sigma v \rangle = \left(\frac{8}{\pi \mu} \right)^{\frac{1}{2}} \frac{1}{(kT)^{\frac{3}{2}}} \int_0^\infty S(E) \exp \left(-\frac{E}{kT} - \sqrt{\frac{E_G}{E}} \right) dE \, , \tag{2.126}$$

where E_G is the Gamow energy which is given by:

$$E_G = 2\mu \left(\pi e^2 Z_1 Z_2 \right)^2 = (2\pi\eta)^2 \, E \, . \tag{2.127}$$

As for non-resonant reactions the S-factor by construction varies smoothly with energy, the energy dependence of the reaction rate is determined primarily by the exponential term in equation (2.126). The two terms in the exponential highlight the two competing elements in the reaction rate. The thermal distribution of the nuclei involved in the reactions is described by the Maxwell-Boltzmann distribution: $\exp -\frac{E}{kT}$, meaning that the number of nuclei at high energies drops off exponentially. The probability of penetration through the Coulomb barrier increases exponentially with energy, this leads to the second term. The Maxwell-Boltzmann distribution has a peak at $E = kT$, however the effect of the Coulomb barrier penetration is to shift the peak in the integrand of equation (2.126) to an energy that is generally much greater than kT, which is known as the Gamow peak. This greatly reduces the limits of the integration in equation (2.126) that are required to calculate the reaction rate to a reasonable degree of accuracy.

In the present description of non-resonant capture reactions using FMD, two clusters in their ground states impinge on one another with a certain relative kinetic energy E and orbital angular momentum ℓ, they fuse to form a compound nucleus and decay to a bound state in this compound nucleus via the emission of a γ-ray. Therefore the required nuclear physics input is the scattering state, the bound state and the transition operator. This enables the calculation of the relevant transition matrix element which, aside from phase space and normalisation factors, determines the cross section.

Once a scattering state with the appropriate boundary conditions at the scattering energy is found by the method outlined in section 2.3.6, this state can be used as the initial state in the calculation of a capture reaction. The bound states in the compound nucleus can also be calculated within the FMD framework by multiconfiguration calculations in the bound state approximation as described in 2.1.4 and 2.3.6.

Extending the FMD wave function

As mentioned above, in astrophysical scenarios the energy is often so low that the scattering wave function must tunnel a very long way through the Coulomb barrier into the interaction region, the bound state in the compound nucleus also

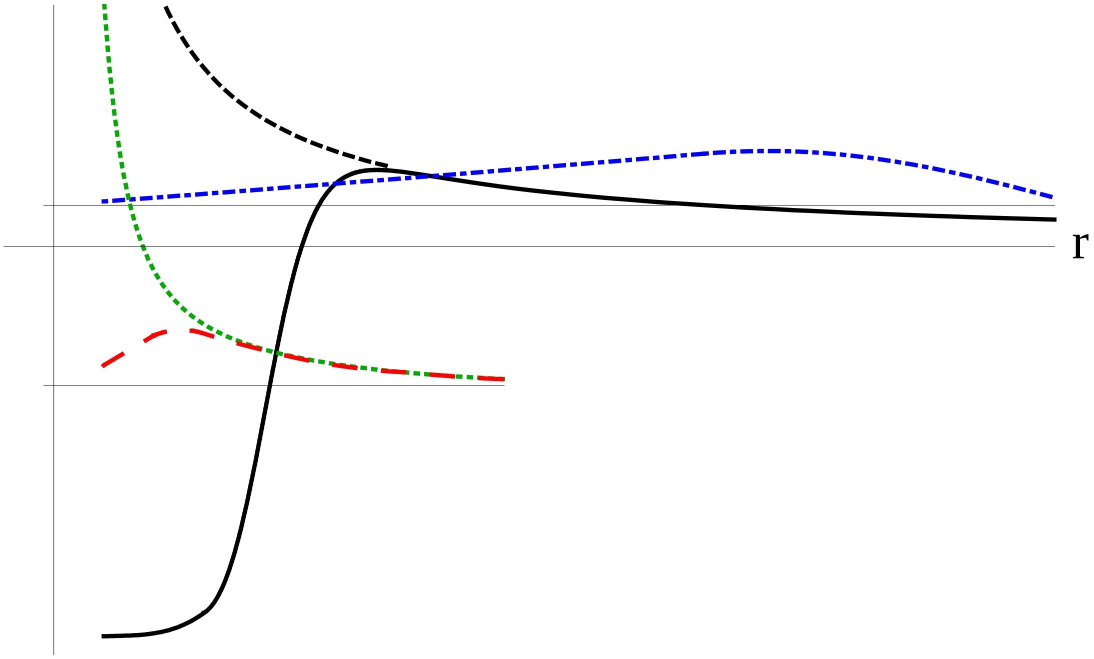

Figure 2.11.: A schematic representation of the total potential (solid black line) with the Coulomb plus centrifugal potential contribution shown by the black dashed line. The scattering state (blue dot-dashed line) is shown tunnelling in through the Coulomb barrier. The bound state (red long dashed line) is shown tunnelling into the Coulomb barrier from the inside and the continuation of the Whittaker function of the second kind is shown by the green dotted line.

tunnels out to some distance under the Coulomb barrier; a schematic representation of this is shown in figure 2.11. This results in the maximum in the transition matrix element, and therefore the major contribution to the radiative capture cross section, being determined by the bound and scattering states at relative distances much greater than the nuclear radius.

To describe capture reactions at low energies as accurately as possible, the FMD wave function should therefore be extended out as far as possible in the available model space by supplementing the n_{IN} coefficients of the wave function $\vec{\psi}_k$ that can be calculated by diagonalising the modified eigenvalue problem (2.114). It is the scattering state, not the scattering wave function that enters into the calculation of the transition matrix element and hence the cross section (equation (2.140)). However, it is the FMD and Coulomb wave functions that must match outside the range of the nuclear interaction. Hence a prescription is required for obtaining the relevant FMD scattering state coefficients from the Coulomb wave function.

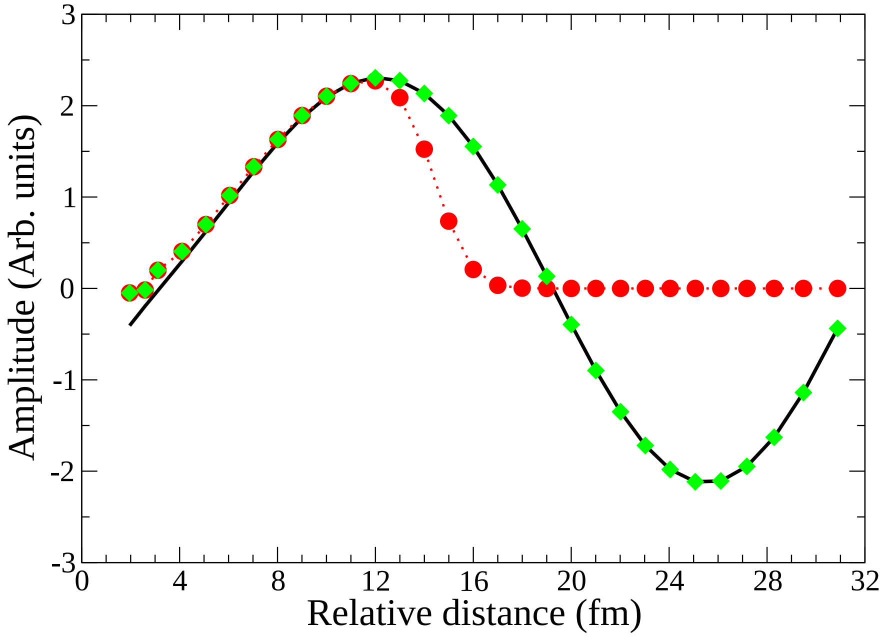

Figure 2.12.: The FMD and Coulomb scattering wave functions for ^{3}He, ^{4}He scattering in the $\frac{1}{2}^+$ channel. The red dotted line with circles includes just the first 11 coefficients from solving (2.114) and the green diamonds include all 31 coefficients chosen so as to match the Coulomb wave function (black solid line).

From equation (2.109) in the last section, the first n_{IN} coefficients $\vec{\psi}_k$ of the FMD wave function can be calculated. These coefficients are chosen such that when the FMD wave function is calculated, beyond the range of the nuclear potential, it will match the Coulomb wave function. However it is vital to remember that the FMD basis is non-orthogonal, therefore the FMD wave function given in equation (2.75) is given in matrix form as:

$$\frac{1}{\sqrt{\Delta_i}} \left\langle B; i \,\middle|\, k; J^\pi M \alpha \right\rangle = \frac{1}{\sqrt{\Delta_i}} \vec{\beta}_i^\dagger \, \mathsf{N}^{\mathsf{FA}} \, \vec{k}_\alpha^{J^\pi M} \qquad i \in \{\mathrm{F}\} \; . \tag{2.128}$$

The non-orthogonality requires the overlap matrix N^{FA} to connect the frozen subspace spanned by the eigenvectors of the $\underset{\sim}{B}$ operator with coefficients $\vec{\beta}_i^\dagger$ to the full model space spanned by the scattering states with coefficients $\vec{k}_\alpha^{J^\pi M}$, as seen in the second term of figure 2.10.

In figure 2.12 the wave function with two different subsets of the coefficients of the FMD wave function can be seen for illustrative purposes. If only the first 11 $\vec{k}_\alpha^{J^\pi M}$ coefficients obtained from solving (2.114) are used in calculating the wave function, the red circles are obtained. These are the coefficients that weight the Slater determinants to give the scattering solution, and as the frozen states are ordered according to increasing relative distance between the clusters, it is reasonable that the Coulomb wave function is only well reproduced at the smaller relative distances. However, as was alluded to in the last paragraph, the wave function does not go to zero sharply. This is because the non-orthogonality of the FMD basis means that the overlap matrix N^{FA} connects more than just the first 11 eigenstates of the relative distance operator $\underset{\sim}{B}$ with the 11 non-zero coefficients of the scattering state. In fact it can be seen that it takes about six more points in the relative distance for the wave function to go to zero. This is the number of relative distance eigenstates beyond the matching point that the overlap matrix connects with the last non-zero coefficient of the scattering state. Consequently this is the number of boundary conditions that would be chosen in this case, and for exactly this reason, as was discussed in section 2.3.5.

By using the fact that the FMD and Coulomb wave functions must match beyond the range of the nuclear interaction the rest of the coefficients out to the edge of the model space can be obtained, as will be explained shortly. This leads to the green diamonds that give an FMD wave function that matches the Coulomb wave function right out to the edge of the model space.

Another important point to note from figure 2.12 is that at the edges of the model space the eigenvalues of the $\underset{\sim}{B}$ operator transformed using equation (2.64) start to differ more and more from the relative distances between the centres of mass of the clusters, which is why the first point in figure 2.12 is not located at 1 fm and the last is not at 30 fm. This is due to the fact that at small distances, the relative distance measure fails conceptually, as stated earlier, due to the clusters starting to overlap. At the outer edge of the model space, the state is not properly localised due to there being no more states beyond 30 fm to give the overlaps and hence localise the state properly as was shown in figure 2.9. A plot of the relative distance against the position in which the Slater determinants were placed which illustrates this point is shown in figure 2.13.

The next step in the fitting procedure allows for the extension of the wave function out to the edge of the Hilbert space. Beyond the range of the nuclear interaction, the FMD wave function must match the Coulomb wave function with the appropriate values of ρ, η and ℓ:

$$\begin{aligned} \frac{1}{\sqrt{\Delta_i}} \left\langle B; i \,\middle|\, k; J^\pi M \right\rangle &\overset{!}{=} \left\langle r_i \,\middle|\, u; k\ell \right\rangle \\ \left| B; i \right\rangle &= \sum_{a\alpha \in \mathrm{INT}} \left| Q^{(a)}; \alpha \right\rangle \beta_i^{(a,\alpha)} + \sum_{b \in F} \left| Q^{(b)}; K \right\rangle \beta_i^{(b)} \,, \end{aligned} \tag{2.129}$$

where the $J^\pi M$ quantum numbers of the basis states have been omitted because they are the same throughout the set of equations. All the coefficients $\beta^{(a,\alpha)}$ in

1	1.96
2	2.59
3	3.11
4	4.10
5	5.08
6	6.05
7	7.03
8	8.02
9	9.01
10	10.0
11	11.1
12	12.0
13	13.0
14	14.0
15	15.0

16	16.0
17	17.0
18	18.0
19	19.0
20	20.0
21	21.0
22	22.0
23	23.0
24	24.0
25	25.1
26	26.1
27	27.2
28	28.3
29	29.5
30	30.9

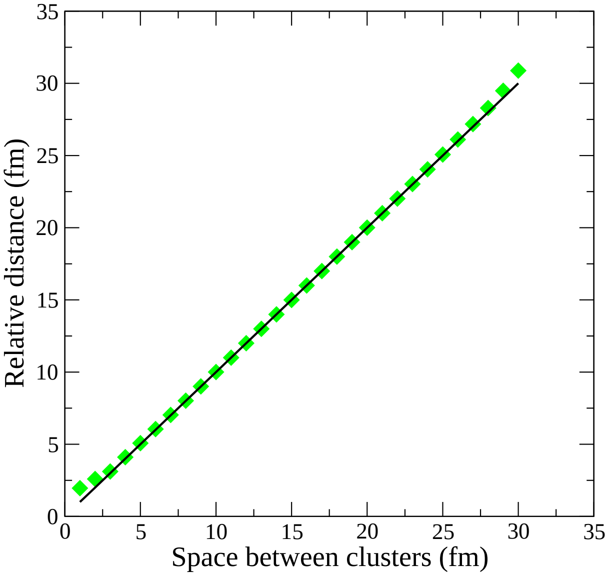

Figure 2.13.: Plot of the relative distance between the ^{3}He and ^{4}He clusters from figure 2.12 against the separations at which the Slater determinants were placed. The solid line is y=x for comparison, the green diamonds are the relative distances. The data from the plot are given in the table to the left.

the first sum of the above equation are zero as the relative distance is only defined for the frozen states, therefore in calculating the wave function only the second term needs to be included.

The scattering state can be split into a part to be kept fixed which is affected by the nuclear interaction, and a part to be fitted so that the FMD wave function calculated from it will match the Coulomb wave function. It is therefore written as:

$$\left| \, k; J^\pi M \, \right\rangle = \sum_{a\alpha \in \mathrm{FIX}}^{n_{\mathrm{FIX}}} \left| \, Q^{(a)}; \alpha \, \right\rangle k^{(a,\alpha)} + \sum_{c\gamma \in \mathrm{FIT}}^{n_{\mathrm{FIT}}} \left| \, Q^{(c)}; \gamma \, \right\rangle k^{(c,\gamma)} \tag{2.130}$$

the definitions of the sets are illustrated in figure 2.14. To exemplify this, in the example of the fitting procedure shown in figure 2.12, n_{FIX} was chosen to be 11, n_{FIT} was chosen to be 20 and n_{BIN} was chosen to be 3. The goal then is to calculate the coefficients $k^{(c,\gamma)}$ of the last sum. To calculate each of these coefficients the value of the Coulomb wave function at the relevant relative distance must be calculated and then from it the required coefficients of the FMD wave function can be calculated. As the FMD wave function is given in matrix form by (2.128), it should be simple to just apply the inverse of this to the Coulomb wave function

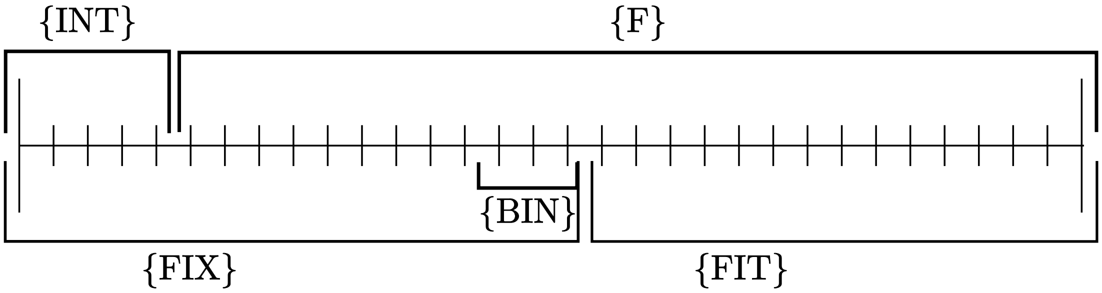

Figure 2.14.: Each coefficient is shown as a vertical line crossing the horizontal, sets of coefficients are bracketed by the name of the set that they belong to.

to give the required coefficients:

$$\begin{aligned} \frac{1}{\sqrt{\Delta_i}}\, \vec{\beta}_i^{\dagger}\, \mathsf{N}^{\mathsf{FA}}\, \vec{k} &\overset{?}{=} u_\ell^i(\eta,\rho) \qquad\qquad i \in \{\text{FIT}\} \\ \Rightarrow \qquad \vec{k} &\overset{?}{=} \left(\frac{1}{\sqrt{\Delta_i}}\, \vec{\beta}_i^{\dagger}\, \mathsf{N}^{\mathsf{FA}}\right)^{-1} u_\ell^i(\eta,\rho)\ . \end{aligned} \tag{2.131}$$

However, again as a consequence of the non-orthogonality of the FMD basis, to calculate each of the coefficients for $\alpha \in$ FIT the contribution to the Coulomb wave function from the fixed coefficients must also be included:

$$\begin{aligned} \vec{k}_i = \left(\frac{1}{\sqrt{\Delta_i}}\, \vec{\beta}_i^{\dagger}\, \mathsf{N}^{\mathsf{FA}}\right)^{-1} &\left(u_\ell^j(\eta,\rho) - \frac{1}{\sqrt{\Delta_j}}\, \vec{\beta}_j^{\dagger}\, \mathsf{N}^{\mathsf{FA}}\right) \\ &i \in \{\text{FIT}\}\ ; \quad j \in \{\text{BIN} \cup \text{FIT}\}\ . \end{aligned} \tag{2.132}$$

hence {BIN} includes the last few of the fixed states (n_{BIN}) that have some overlap with the first of the fitted ones, as illustrated in figure 2.14. These $\vec{k}_i$ are the fitted coefficients, so when they are combined with the fixed coefficients they provide the scattering state coefficients which give the FMD wave function out to the edge of the model space, as is shown by the green diamonds in figure 2.12.

Normalising the incoming flux

To enable the comparison of calculations and measurements of the capture cross section, there has to be some kind of agreement as to the normalisation of the incoming flux $\vec{J}$, which is normally set to unity. In experiment this corresponds to dividing the measured cross section by the number of incident particles. As all the clusters considered in this thesis are eigenstates of the total angular momentum operator $\underset{\sim}{J}^2$, the potential felt by each cluster due to the other one is spherically symmetric. For uncharged clusters, the centrifugal component falls off quickly enough ($\frac{1}{r^2}$) that the scattering wave function can be given as the sum of an incoming plane wave and a phase shifted outgoing plane wave. To normalise the flux of the incoming plane wave, a factor of $\frac{1}{\sqrt{\vec{v}}}$, where $\vec{v}$ is the velocity of the wave packet, is multiplied onto the wave function:

$$\vec{J} = \frac{1}{\mu}\,\mathrm{Im}\left\{\Psi^* \underset{\sim}{\vec{\nabla}}\,\Psi\right\} = \frac{1}{\mu}\,\mathrm{Im}\left\{e^{-i\vec{k}\vec{r}}\,\underset{\sim}{\vec{\nabla}}\,e^{i\vec{k}\vec{r}}\right\} = \frac{\vec{k}}{\mu} = \vec{v} \tag{2.133}$$

this factor then ensures that the total flux $\vec{J}$ including all partial waves is normalised to unity. The Coulomb force does not decrease so quickly, but as the flux is determined at infinite relative distance where the Coulomb force is also zero, the same normalisation can also be used for charged nuclei.

The Coulomb scattering wave function is given by:

$$I_\ell(\eta,\rho) = G_\ell(\eta,\rho) - iF_\ell(\eta,\rho); \quad O_\ell(\eta,\rho) = G_\ell(\eta,\rho) + iF_\ell(\eta,\rho) \tag{2.134}$$

as stated earlier (2.122). In the program the scattering state is calculated for each partial wave. Decomposing the incoming plane wave into partial waves and multiplying by the aforementioned normalisation factor of $\frac{1}{\sqrt{\vec{v}}}$ gives the incoming wave function as the Coulomb scattering solution with unit flux in the z-direction:

$$\begin{aligned}
\left\langle\, B; i \,\middle|\, k; J^\pi M \,\right\rangle &\overset{!}{=} \left\langle\, r_i \,\middle|\, u; k\ell \,\right\rangle \\
&= \frac{1}{\sqrt{v}} \sum_\ell \sqrt{\pi}\sqrt{2\ell+1}\, i^{\ell+1} \frac{e^{i\kappa_\ell}}{k} \left(I_\ell(\eta,\rho) - e^{2i\delta_\ell} O_\ell(\eta,\rho)\right) \frac{Y_\ell^0(\hat{r})}{r_i} \\
I_\ell(\eta,\rho) &= G_\ell(\eta,\rho) - iF_\ell(\eta,\rho)\,; \quad O_\ell(\eta,\rho) = G_\ell(\eta,\rho) + iF_\ell(\eta,\rho) \\
G_\ell(\eta,\rho) &\overset{r\to\infty}{\Longrightarrow} \cos\left(\rho - \tfrac{1}{2}\ell\pi - \eta\ln(2\rho) + \kappa_\ell\right) \\
F_\ell(\eta,\rho) &\overset{r\to\infty}{\Longrightarrow} \sin\left(\rho - \tfrac{1}{2}\ell\pi - \eta\ln(2\rho) + \kappa_\ell\right)\ ,
\end{aligned} \tag{2.135}$$

where $\rho = kr$ and κ_ℓ is the phase shift due to the Coulomb potential [25][43], as opposed to that due to the nuclear potential which is denoted by δ_ℓ.

Equation (2.135) therefore gives the required normalisation factor for the FMD scattering state to ensure that the total incoming flux will be unity:

$$\frac{1}{\sqrt{v}}\sqrt{\pi}\sqrt{2\ell+1}\, i^{\ell+1}\frac{e^{i\kappa_\ell}}{k}\left|\, k; J^\pi M \,\right\rangle = \sqrt{\frac{\mu\pi(2\ell+1)}{k^3}}\; i^{\ell+1} e^{i\kappa_\ell}\left|\, k; J^\pi M \,\right\rangle\,. \tag{2.136}$$

However, as the cross section requires the absolute square of the transition matrix element (see (2.140)), in calculating the cross section, S-factor and reaction rate the factors $i^{\ell+1}$ and $e^{i\sigma_\ell}$ will disappear.

Electromagnetic transition operators

With the flux of the scattering state now normalised to unity, the scattering state is uniquely defined. The last requirement can now be tackled, which is to calculate the allowed multipole transitions between the scattering and bound states, both of which have been calculated using the FMD model.

As the astrophysical environments considered in this thesis provide so little energy for reactions to occur, the relevant multipole transitions are limited to electric dipole (E1), electric quadrupole (E2) and magnetic dipole (M1) transitions, higher order transitions will not make significant contributions to the cross section. For the same reason, a photon emitted in one of the radiative capture reactions considered here will not have an energy greater than $\approx$ 10 MeV, this corresponds to a photon wavelength of: $\frac{2\pi\hbar c}{E_\gamma} = 177$ fm, which is far greater than any nuclear radius. This allows the electric and magnetic transition operators to be used in a form consistent with the long wavelength limit [52].

The electric Q^λ_μ and magnetic M^λ_μ multipole operators of order λ are given by [52]:

$$\begin{aligned}
Q^\lambda_\mu &= \sum_{i=1}^{A} e(i) r_i^\lambda Y^\lambda_\mu(\theta_i,\phi_i) \\
M^\lambda_\mu &= \sum_{i=1}^{A} \left(g_s(i)\vec{s}_i + g_l(i)\frac{2\vec{l}_i}{\lambda+1} \right) \cdot \vec{\nabla}_i \left(r_i^\lambda Y^\lambda_\mu(\theta_i,\phi_i) \right) \qquad (2.137) \\
\text{for protons: } e(i) &= 1e\,; \quad g_l(i) = 1\mu_\mathrm{N}\,; \quad g_s(i) = 5.586\mu_\mathrm{N} \\
\text{for neutrons: } e(i) &= 0\,; \quad g_l(i) = 0\,; \quad g_s(i) = -3.826\mu_\mathrm{N}\ ,
\end{aligned}$$

where e is the elementary charge and μ_N is the nuclear magneton.

The states that can be connected using these operators are given by the following selection rules:

$$\begin{aligned}
&\text{Electric:} \qquad \pi_i = \pi_f(-1)^\ell \qquad\qquad \vec{J}_i = \vec{J}_f + \vec{\ell} \\
&\text{Magnetic:} \qquad \pi_i = \pi_f(-1)^\ell + 1 \qquad \vec{J}_i = \vec{J}_f + \vec{\ell}
\end{aligned} \qquad (2.138)$$

As it is not always possible, especially for nuclei beyond the p-shell, to describe the whole of the energy spectrum of the compound nucleus within a tractable model space, it is important to be able to determine which are the most important transitions for the reaction under consideration so that the model space can be optimised to those states. Looking at the cross section for each channel provides the best way of doing this. The total radiative capture cross section for two clusters with spin I_1 and I_2 fusing and forming a state with total angular momentum J_f thereby emitting electromagnetic radiation in the form of a γ-ray with multipolarity λ and wave vector k is given by [5]:

$$\begin{aligned}\sigma =&8\pi\frac{\lambda+1}{\lambda\left((2\lambda+1))!!\right)^2}k_\gamma^{2\lambda+1}\frac{1}{(2I_1+1)\,(2I_2+1)}\\ &\sum_{\ell=0}^{\infty}\sum_{M_{I_1}=-I_1}^{I_1}\sum_{M_{I_2}=-I_2}^{I_2}\sum_{\mu=-\lambda}^{\lambda}\sum_{M_f=-J_f}^{J_f}\left|\left\langle J_f,M_f\,\middle|\,O_\mu^\lambda\,\middle|\,\Psi,\ell,0;I_1,M_{I_1};I_2M_{I_2}\right\rangle\right|^2\ ,\end{aligned} \tag{2.139}$$

where M_ℓ is zero because the incoming wave propagates along the z-axis and the general scattering state forming the ket in the matrix element is normalised. Using reduced matrix elements and the properties of the Clebsch-Gordan coefficients, this can be rewritten as:

$$\begin{aligned}\sigma(E) = 8\pi&\frac{\lambda+1}{\lambda\left((2\lambda+1))!!\right)^2}k_\gamma^{2\lambda+1}\frac{1}{(2I_1+1)\,(2I_2+1)}\\ &\sum_{\ell=0}^{\infty}\sum_{I}\sum_{J_i}\frac{1}{2\ell+1}\left|\left\langle J_f\,\middle\|\,O^\lambda\,\middle\|\,\Psi,(\ell I)J_i\right\rangle\right|^2\ ,\end{aligned} \tag{2.140}$$

see section A.2 for the derivation of this.

A point worthy of note is that as all the systems considered in this thesis have at most one cluster with an intrinsic spin and that spin has a maximum value of $\frac{1}{2}$, the tensor force cannot connect different values of ℓ, consequently ℓ is a good quantum number in the scattering state and hence it appears in the matrix element in equation (2.140). In general this is not true as if the spin of even just one of the clusters is greater than $\frac{1}{2}$, the tensor force can mix states with different values of ℓ and consequently it is no longer a good quantum number in the scattering state.

3. Testing the Model

3.1. Gamow vectors

In figure 3.1 the points on the iteration path to find resonances are shown. These fixed points in the complex plane are each complex eigenvalues corresponding to the eigenvectors that are solutions of the modified eigenvalue problem (2.114). The starting points for each run of the iteration are the diamonds shown along the real axis at starting energies from 0.1 to 10 MeV in steps of 0.1 MeV. The Hilbert space for these results is composed of thirty frozen states positioned from 1 - 30 fm on a regular grid and a state produced by minimisation after projection on negative parity, which helps to represent the interaction region better.

As can be seen in the figure, from each starting point the next step in the iteration jumps to a point somewhere off the real axis, the points within each run of the iteration being joined with a line to show their association to one another. Dependent on the starting point, after a relatively small number of iterations, a fixed point is reached. For the starting energies shown in the figure, there are four distinct fixed points that are found. In figure 3.2, just the four converged results are shown for comparison to figure 3.1. All the fixed points apart from one in this case are far too wide to represent resonances really and certainly too wide to be described properly by the Gamow method. The one at just below 3 MeV however matches well to the first $\frac{7}{2}^-$ resonance in ^{7}Be.

There is now the question of where there are four solutions found which must all solve the eigenvalue problem, what do the other three much wider 'resonances', or more accurately fixed points as they are so wide, represent. It could be considered that these are not really fixed points, but somehow dependent on the starting point, as in figure 3.1 all the starting points were chosen on the real axis. To remove this possibility, a calculation was done, this time for the 4^+ channel in ^{18}O; as can be seen in figure 3.3 three fixed points were found. The one of these at 4.75 MeV with a width of 5.9 MeV was observed to move around when the value of the matching point was altered. There a grid of points was constructed around this fixed point to test the hypothesis above and an iteration was started from each point on the grid. The result of this can be seen in figure 3.4. Each point on the starting grid is marked by the blue circles, each of these iterations proceeds along one of the paths of red dots. The black dots show the iteration points coming in from below as in the zoomed out version shown in 3.3. This

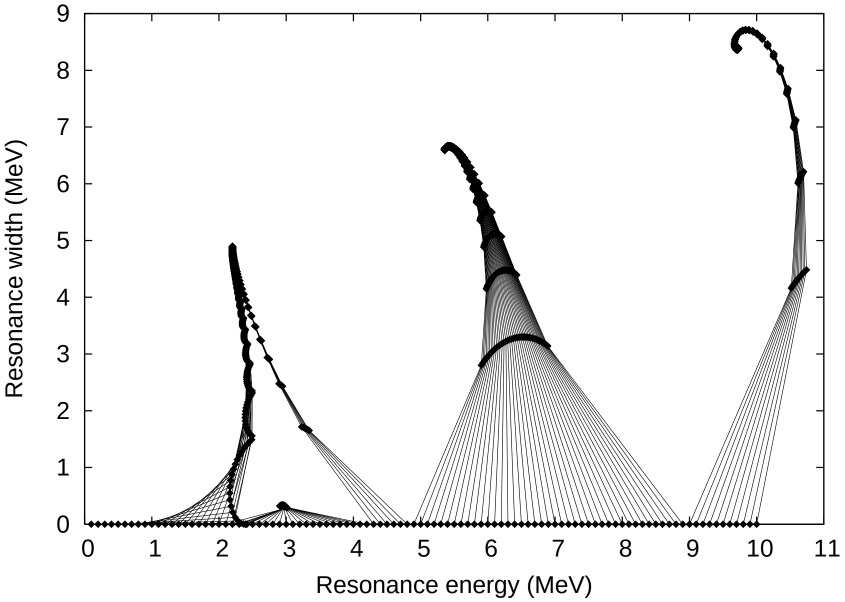

Figure 3.1.: Plot of points along iteration path in searching for resonance energy and width using Gamow states for $\frac{7}{2}^{-}$ resonance in ^{7}Be.

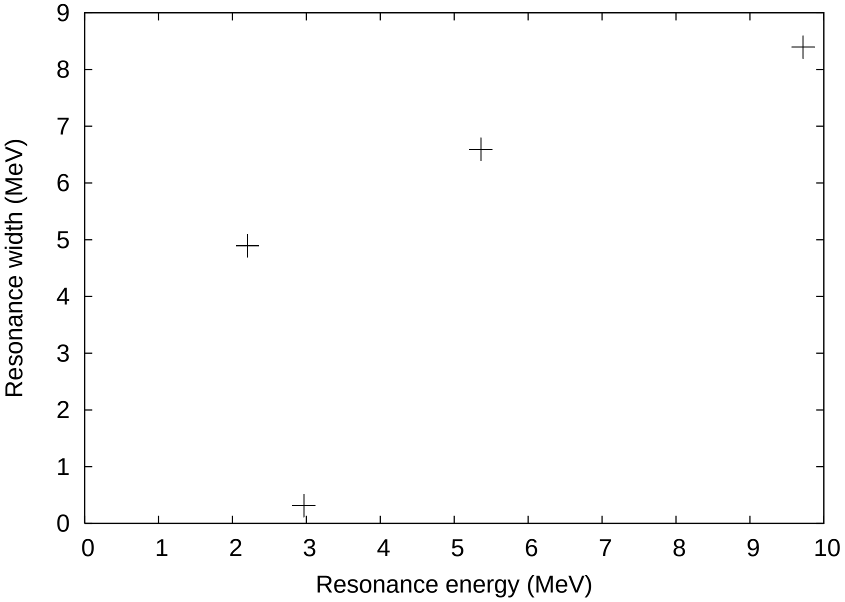

Figure 3.2.: Exactly the same as figure 3.1 but showing only converged results in searching for resonance energy and width using Gamow states.

shows that this, and probably the other fixed points with large width, really are fixed points.

Another possibility is that they represent real 'resonances', but they are so wide, that neither experiment nor our theory would expect to be able to reproduce them, even if they existed in nature. In cases where the distinction is not so clear cut as to which resonances are artefacts and which represent real states, the only method that has so far been devised to distinguish between the two cases is by varying either the matching point or the number of boundary conditions. For a real resonance, its parameters should be independent of these parameters, providing they are chosen within sensible limits, so a variation of the result due to a variation in these parameters may well point to spurious resonances. The small variation that will occur even for a 'real' resonances also provides probably the best estimate for the error of our theoretical method. In figure 3.5 everything is exactly as it was for figure 3.3 (it corresponds to the 10 fm points), except now only converged results are shown. However rather than just for one matching point as was done in figure 3.3, now matching points from 7 to 17 fm are taken. It can be seen that there is a group of points clustered tightly around 4.5 MeV resonance energy that correspond to a 'real' resonance, then there are the other two that can also be seen in figure 3.5, where the result is strongly dependent on the matching point, with the result moving in an arc with the matching point for the result which the grid was placed round in figure 3.4.

These tests have shown that these points are fixed points, but do not correspond to resonances. The question therefore remains, what do they represent? As the energy input in each step of the iteration alters the boundary conditions, this is a non-linear system, therefore there is no a priori way to determine the number of solutions. Mathematically there seems to be no objection to these extra fixed points, they also solve the equations; however, physically they do not correspond to resonances. This is not of great concern because, as demonstrated above, we have a way of distinguishing between real resonances and the other mathematical artefacts.

Variations for a 'real' resonance can be seen for the 3^- channel in ^{18}O in figure 3.6. Excluding the points that correspond to matching at 8 and 9 fm, which is justified as they will have too much overlap with the interaction region where the clusters are overlapping, the results vary by 2.4 keV in the resonance energy and by 15 eV in the width. This is quite a large percentage variation in the width but the resonance energy variation is pretty small. However it must be remembered that for very narrow resonances such as this the difference in the commutators in equation (2.105) must still be calculated and this may lead to certain numerical inaccuracies which may be responsible for this large relative error in the resonance width.

There is another way to test the resonance parameters. Once the scattering state

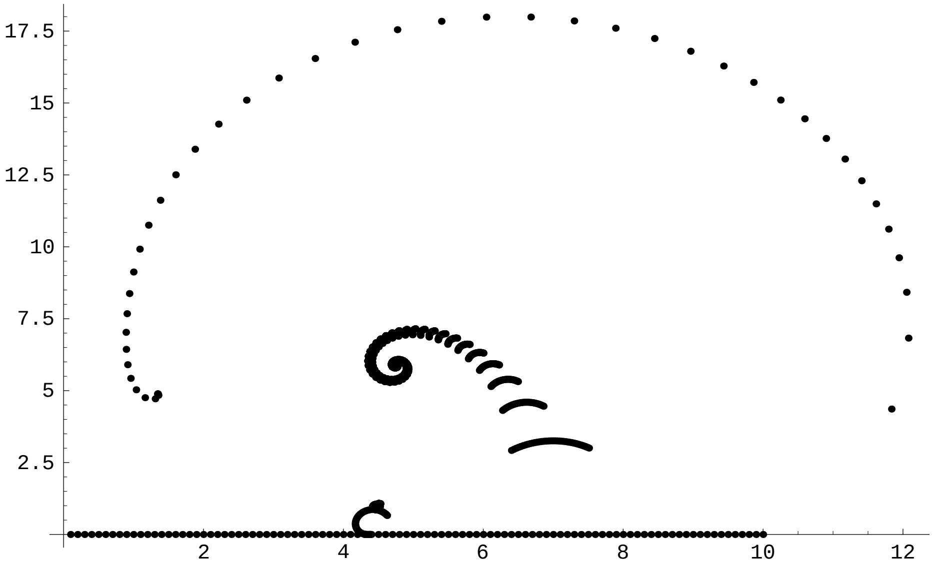

Figure 3.3.: Iteration plot for the 4^+ channel in ^{18}O with a matching point of 10 fm. Resonance energy in MeV shown along the x-axis, resonance width in MeV along the y-axis.

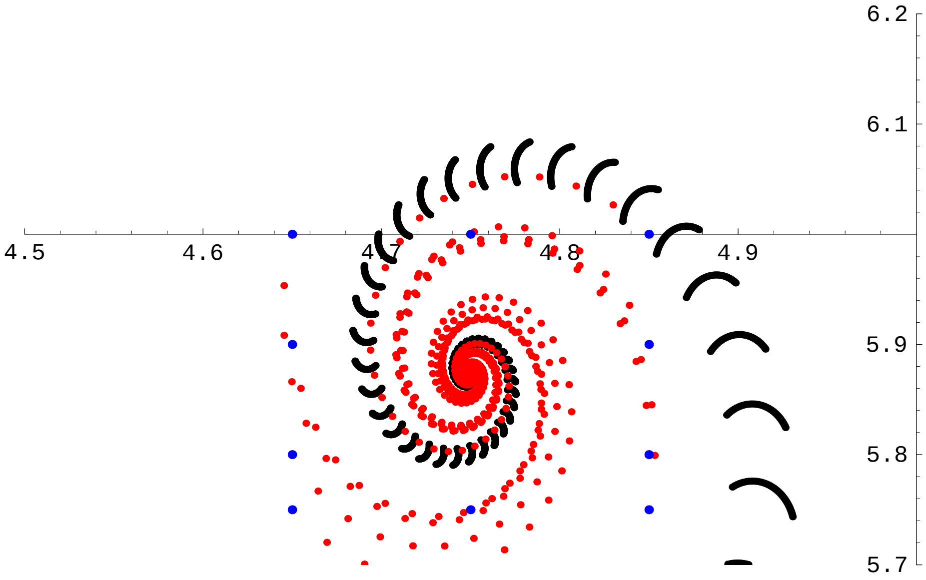

Figure 3.4.: Testing fixed points in iteration plot for the 4^+ channel in ^{18}O, resonance energy in MeV shown along the x-axis, resonance width in MeV along the y-axis. Shown is enlarged section of figure 3.3 with grid of starting points added.

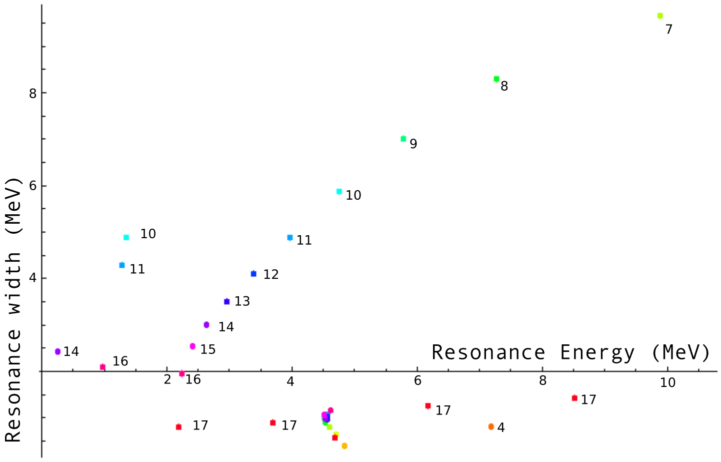

Figure 3.5.: Looking at the 4^+ channel in ^{18}O, as in figures 3.3 and 3.4, however now matching point is being changed and just the converged results are being tracked.

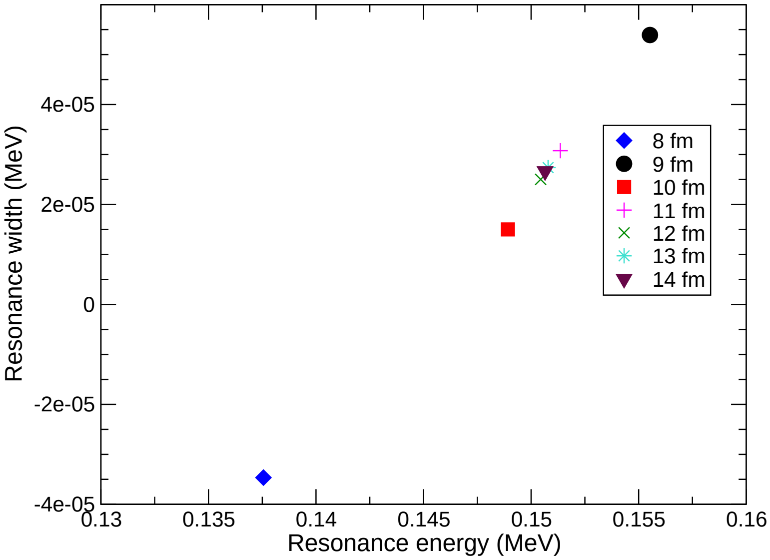

Figure 3.6.: Seeing how the resonance energy and width vary when the matching point is altered for the 3^- channel in ^{18}O.

is found, it is known that it is an eigenstate both of the Hamiltonian with the boundary conditions included and the original Hamiltonian. Therefore:

$$\frac{\vec{\beta}_i \cdot \mathsf{N}^{\mathsf{FA}} \cdot \mathsf{O} \cdot \mathsf{H} \cdot \vec{k}}{\vec{\beta}_i \cdot \mathsf{N}^{\mathsf{FA}} \cdot \vec{k}} = z \, \frac{\vec{\beta}_i \cdot \mathsf{N}^{\mathsf{FA}} \cdot \vec{k}}{\vec{\beta}_i \cdot \mathsf{N}^{\mathsf{FA}} \cdot \vec{k}} = z \qquad i = \text{matching point} \; , \tag{3.1}$$

where z is the complex eigenvalue that comes from the Hamiltonian acting on the scattering state and the rest of the objects in the equation are defined in section 2.4.1. This gives a check therefore on the stability of solving the eigenvalue problem including the boundary conditions, equation (2.114). This seems to work very well in general, results agree on the 1% level, except in the case of very narrow resonances. These problems could be due to both methods becoming numerically unstable due to calculating the commutators in equation (2.105) for very small values of the wave function at the matching point; as the amplitude of the wave function asymptotically becomes vanishingly small as the resonance width tends to zero.

3.2. Comparison of FMD and Coulomb wave functions

At the low energies relevant for a lot of astrophysical scenarios, the scattering state faces a very extended Coulomb and centrifugal barrier (for $\ell \neq 0$) through which it must pass to reach the range of the attractive nuclear interaction. Consequently, for non-resonant channels, the amplitude of the scattering state is very small within the attractive part of the potential. When considering capture reactions this often means that the transition matrix element is largest at a point somewhere beneath the Coulomb barrier, often well outside the range of the nuclear interaction. As our aim is to be able to calculate the cross section for the capture reaction to take place using the FMD states to describe both the bound and scattering waves; all the coefficients of the scattering state must be known so as to give the best possible description of the state at large relative distances.

The first n_{IN} coefficients of the FMD scattering state are calculated by solving equation (2.114) to find the coefficients $\vec{\psi}$. To get a good representation of the wave function out to a relative distance corresponding to the edge of the model space, the procedure explained in section 2.4 can be adopted. This extends the coefficients of the scattering state firstly by another n_{BC} elements using the inverse of the matching procedure from equation (2.113). Then, by using the fact that the FMD wave function should match the Coulomb wave function asymptotically, the coefficients out to the edge of the model space can be obtained from equation (2.132). This gives the best possible description of the scattering state for a particular model space as this means that the contributions from every Slater determinant within the model space are taken into account.

The effect of these procedures on the form of the wave function has been thoroughly tested and in this section a few graphical examples of the FMD wave function at different steps in the procedure are shown. The wave function can only be determined at discrete points determined by the eigenvalues of the $\underset{\sim}{B}$ operator, these are the points shown in the figures; the lines joining them are merely to guide the eye. Figures 3.7, 3.8, 3.9 and 3.10 are for the scattering of ^{3}He and ^{4}He at an energy of 2.0 MeV in the $\frac{7}{2}^-$ channel. The clusters are in their ground states of $\frac{1}{2}^+$ and 0^+ respectively, coupled to an orbital angular momentum of $3\hbar\omega$. Figure 3.11 is for the same system and channel, but at a scattering energy of 3.06 MeV where a $\frac{7}{2}^-$ resonant state in ^{7}Be is located.

The FMD scattering wave function is given by equation (2.131). If just the first n_{IN} coefficients of the scattering state are taken to contribute to the wave function, its form is as shown in figure 3.7.

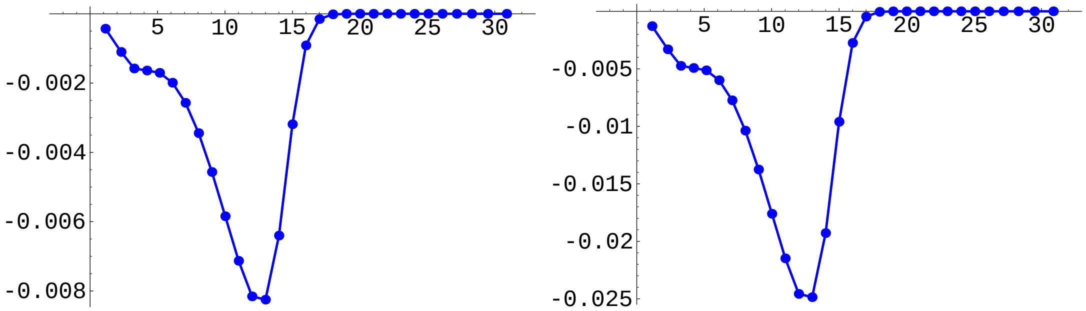

Figure 3.7.: ^{3}He(^{4}He,^{4}He)^{3}He elastic scattering at an energy of 2.0 MeV in the $\frac{7}{2}^-$ channel. On the left is shown the real part of the wave function, on the right the imaginary part. In both, only the contributions from the first n_{IN} coefficients of the scattering state are included.

Once the contributions from the n_{BC} boundary condition states are included, the wave function is extended as shown in figure 3.8.

The scale of the scattering state is arbitrary as it is not yet normalised, so in the next step it is scaled by a phase so as to match the Coulomb wave function. In figure 3.9, the FMD and Coulomb wave functions are plotted together. At very small relative distances they are not expected to match one another as the Coulomb wave function is calculated for two point charges which is not an accurate description when the clusters start to overlap. As can be seen from the figure, the wave functions then match well up to the point where the coefficients for the FMD wave function run out.

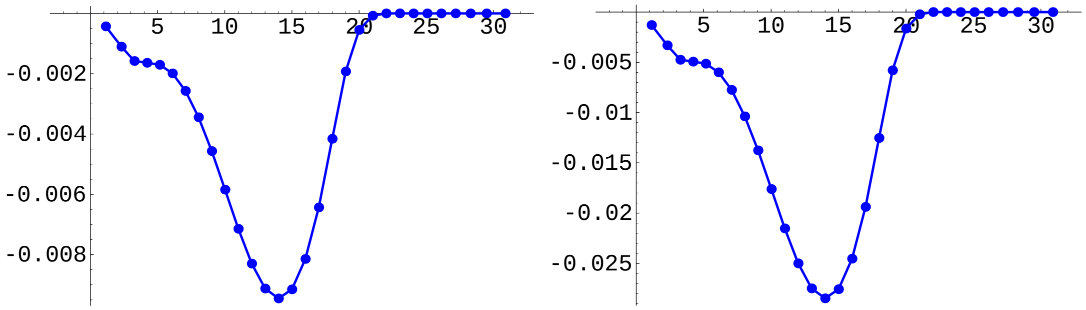

Figure 3.8.: ^{3}He(^{4}He,^{4}He)^{3}He elastic scattering at an energy of 2.0 MeV in the $\frac{7}{2}^-$ channel. On the left is shown the real part of the wave function, on the right the imaginary part. n_{BC} additional coefficients have been added to the description of the scattering state by performing the inverse process to equation (2.113) using the transformation provided therein by the S matrix.

Finally, the condition that the FMD wave function should match the Coulomb wave function asymptotically leads to figure 3.10. Here it can be seen that the FMD wave function has the appropriate asymptotic behaviour of two point charges.

In the last few figures the case for a scattering state at an energy where there was no resonance was shown. The wave function had only a low amplitude at small relative distances, corresponding to the fact that there was only a small probability for the two clusters to penetrate the Coulomb barrier and fuse. If however the compound system has a resonance at the scattering energy with the appropriate quantum numbers, then the probability for fusion is much higher and therefore the amplitude of the wave function in the interior region is also much higher. This can be seen if exactly the same system is taken as before, but the scattering energy is now increased to 3 MeV, where there is a resonance in the $\frac{7}{2}^-$ channel. The plots of the wave functions are shown in figure 3.11. As can be seen, the amplitude of the wave function below 5 fm is much higher than that in figure 3.10.

The narrower the resonance, the more pronounced this effect is, as the width of the resonance is inversely proportional to its lifetime and the longer the lifetime of the resonance the greater the probability for fusion. In figure 3.12 the FMD and Coulomb wave functions for ^{14}C(^{4}He,^{4}He)^{14}C scattering in the 3^- channel at a centre of mass energy of 150 keV are shown. This corresponds to a 3^- resonant state in ^{18}O with a calculated width of 27 eV.

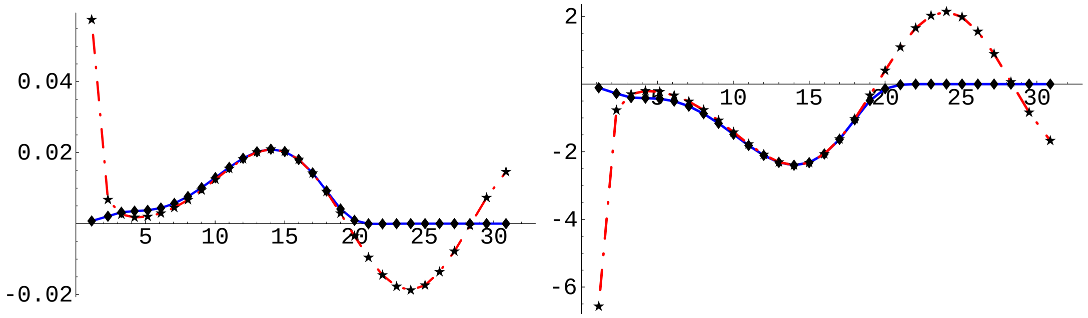

Figure 3.9.: ^{3}He(^{4}He,^{4}He)^{3}He elastic scattering at an energy of 2.0 MeV in the $\frac{7}{2}^-$ channel. On the left is shown the real part of the wave functions, on the right the imaginary part. The FMD wave function (blue solid lines marked with diamonds) is not normalised and therefore we are free to apply a phase to it to scale it to match the Coulomb wave function (red dot-dashed line marked with stars).

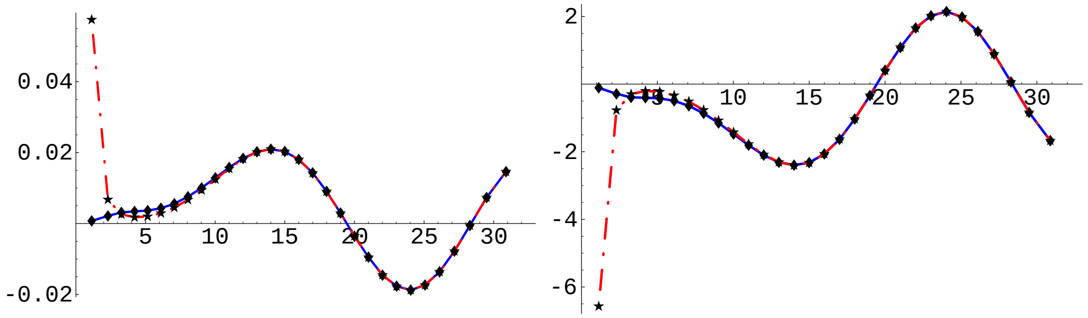

Figure 3.10.: ^{3}He(^{4}He,^{4}He)^{3}He elastic scattering at an energy of 2.0 MeV in the $\frac{7}{2}^-$ channel. On the left is shown the real part of the wave function, on the right the imaginary part. The last coefficients of the FMD scattering state are obtained from the requirement that the FMD wave function (blue solid lines marked with diamonds) and the Coulomb wave function (red dot-dashed line marked with stars) should match asymptotically.

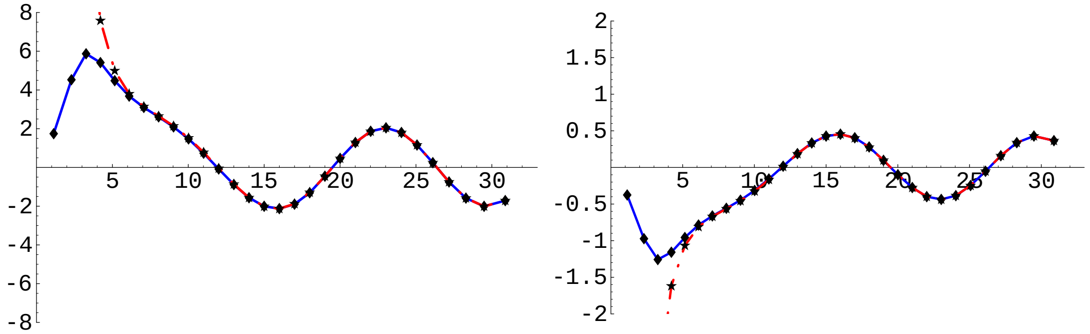

Figure 3.11.: ^{3}He(^{4}He,^{4}He)^{3}He elastic scattering at an energy of 3.06 MeV in the $\frac{7}{2}^{-}$ channel. On the left is shown the real part of the wave function, on the right the imaginary part. For this narrow resonance (calculated width of 353 keV), a large amplitude is found for the wave function inside the range of the nuclear interaction, in comparison to the wave function off-resonance for the same system which as in figure 3.10.

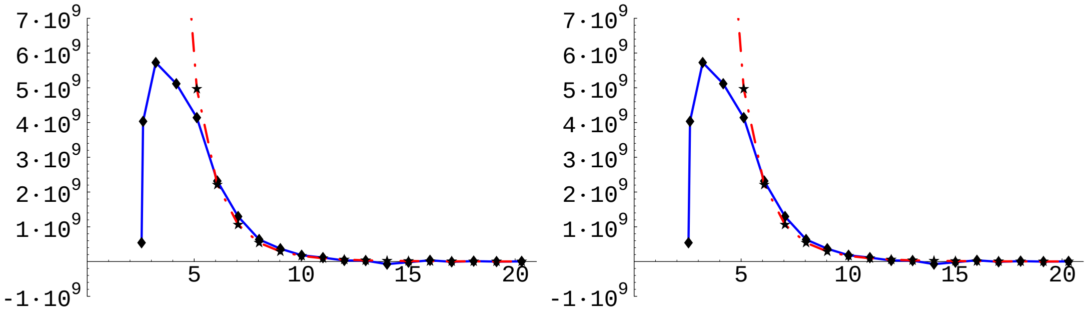

Figure 3.12.: ^{14}C(^{4}He,^{4}He)^{14}C elastic scattering at an energy of 0.15 MeV in the 3^{-} channel. On the left is shown the real part of the wave function, on the right the imaginary part. For a very narrow resonance (calculated width of 27 eV) the amplitude of the wave function in the interior region compared to that in the exterior region is even more pronounced than in figure 3.11.

4. Results

The results in this chapter are split up into sections relating to the reaction under consideration. Due to the current limitations of the method, there are certain restrictions on the reactions that can be calculated:

- Single channel calculation: therefore the ground state of the clusters should be well separated in energy from any of their excited states so that there is no significant mixing within states with a different cluster nature in the compound nucleus.
- Single projection: due to the computing time required. Therefore reactions such as $^{12}\mathrm{C}(\alpha,\gamma)^{16}\mathrm{O}$ cannot be calculated as the 2^+ state in $^{12}\mathrm{C}$ is known to make an important contribution to the cross section in the astrophysical energy regime.
- Frozen states: require axially symmetric systems for the frozen states due to the computing time required. Therefore at least one of the nuclei involved in the reaction must have a ground state with zero spin. Then if the other cluster has spin, it can without loss of generality be oriented such that it points along the symmetry axis between them.
- Tensor force: in the way that the code is presently implemented, the spin of one cluster has to be zero otherwise the tensor force could mix channels with different orbital angular momenta and the boundary conditions would then have to match each FMD wave function separately to the Coulomb wave function with the correct ℓ.

The final aim of these calculations is to arrive at values for the S-factors of astrophysical radiative capture reactions. But a lot can be learnt along the way by considering other observables that can be used to check how well the model and model space describe nature. Some of these quantities are calculated and discussed in the results that follow, namely: the energy spectrum of the compound nucleus in the reaction, the ground state energies of the clusters and, where data exists, phase shifts to test the accuracy of the scattering states both resonant and non-resonant.

4.1. $^3\mathrm{He}(\alpha,\gamma)^7\mathrm{Be}$

This reaction rate is required in two different astrophysical regimes and consequently in two different temperature and therefore energy ranges. The first is in the hydrogen burning phase of solar mass main sequence stars, the second is for big bang nucleosynthesis [35].

The PPII and PPIII chains in stellar hydrogen burning both have $^3\mathrm{He}(\alpha,\gamma)^7\mathrm{Be}$ as the initial reaction and although between them they provide only about 14% of the total solar energy production, the rest being provided by the PPI chain; electron capture on ^{7}Be and the β^+-decay of ^{8}B between them produce practically all of the high-energy solar neutrinos. Although the solar neutrino problem now appears to have been solved by neutrino oscillations, a knowledge of the abundance of ^{7}Be and hence the neutrino flux produced in the correct energy range can provide stringent tests of the standard solar model.

The amount of ^{7}Be produced in the early universe is of great interest in primordial ^{7}Li abundances because ^{7}Be undergoes β^--decay with a half-life of about 53 days making it an important part of one of the production paths for ^{7}Li. Being able to narrow the errors in the abundance of ^{7}Li in the early universe allows constraints to be placed on cosmological theories.

4.1.1. One Gaussian per nucleon

Using the standard AV18 interaction, with the FMD correction mentioned in section 2.2 included, ^{4}He and ^{3}He clusters were formed and minimised separately, their energies and charge radii are shown in comparison to experimental results in table 4.1 alongside "V_{UCOM}". Using these clusters, frozen states at relative distances from 1 to 30 fm in steps of 1 fm were constructed. A multiconfiguration calculation of the bound states of ^{7}Be was made, first with just the frozen states

1 Gaussian per nucleon FMD using AV18	charge radius (fm)		E_0 (MeV)	
	^{4}He	^{3}He	^{4}He	^{3}He
V_{UCOM}	1.639	1.769	-27.864	-6.011
V_{UCOM} LS tuned	1.640	1.770	-27.689	-5.926
V_{UCOM} threshold tuned	1.598	1.770	-28.196	-6.087
Experiment [46][47]	1.671 ± 0.014	1.976 ± 0.015	-28.296	-7.718

Table 4.1.: Mass radii and ground state energies for ^{4}He and ^{3}He clusters calculated using one Gaussian per nucleon and the AV18 interaction with the normal FMD correction (top row) and then with two different tunings of this correction.

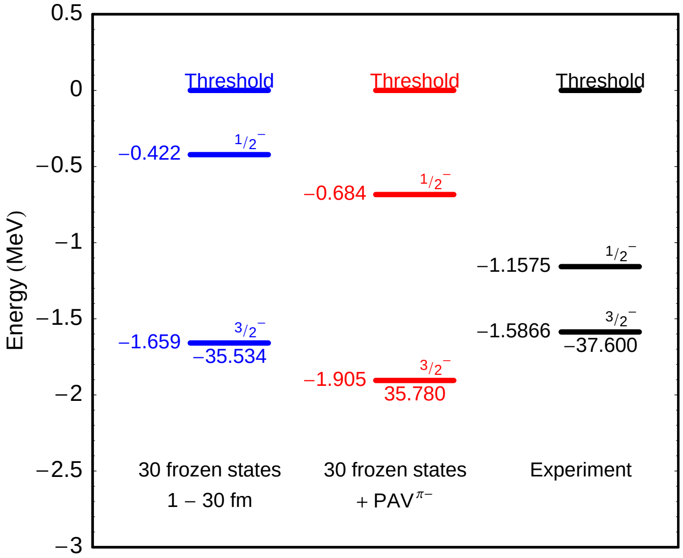

Figure 4.1.: The energy spectrum for the bound states in ^{7}Be where energies to the left of each level are shown relative to the particle emission threshold in each case and the actual ground state energies are shown below the relevant levels. The results were calculated using the AV18 interaction with the full FMD correction, 30 frozen states placed at relative distances from 1 to 30 fm in steps of 1 fm (blue levels) and then including a PAV$^{\pi-}$ state (red levels). Experimental data taken from [45].

and then using the same frozen states but also including a state minimised under the constraint of having negative parity (PAV$^{\pi-}$); this gave the results in figure 4.1[1].

The levels in figure 4.1 are plotted relative to the threshold for particle emission, as are all the spectra that are presented in this thesis. The reason for this is that in a non-resonant reaction such as this one the energy of the bound states relative to the particle emission threshold is the important quantity rather than the absolute energy scale of the levels. This is because at astrophysical energies the Coulomb repulsion keeps the nuclei at relative distances much greater than the nuclear radius. Therefore it is the asymptotic part of the bound state wave function that enters into the cross section with an exponential dependence. Also, the energy of the emitted γ-ray is proportional to the energy of the final bound state relative to the threshold plus the scattering energy, and this quantity enters into the phase space factor in the cross section (2.140). These two factors together mean that the bound states must be more accurately reproduced to have any hope

---

[1] Thanks to Mark Caprio for the LevelScheme package for Mathematica with which these spectra were produced [4].

of calculating meaningful values for the cross section and S-factor.

The description of the clusters cannot be improved whilst still using only 1 Gaussian per nucleon as they must be in their ground state. Therefore improving the model space would shift the absolute ground state energy of the compound nucleus down, but would also shift it down with respect to the threshold because the threshold energy would remain unchanged. Looking at figure 4.1 this is not what is required. In fact this effect can be seen already in the figure when the $\mathrm{PAV}^{\pi-}$ state is added to the model space.

One thing that can be done is to tune the phenomenological FMD correction that was made to $\mathrm{V}_{\mathrm{UCOM}}$ (section 2.2). Fine-tuning the FMD correction to the correlators in $\mathrm{V}_{\mathrm{UCOM}}$ does not correspond to just fitting the interaction to get the correct S-factor out. It also does not affect how ab-initio the approach is, as we are only correcting the phenomenological FMD correction to the $\mathrm{V}_{\mathrm{UCOM}}$ interaction. It is tuning the one part of the model that is phenomenological due to the lack of three-body forces and missing parts of the tensor force as described in section 2.2.

Fine-tuning the FMD correction to $\mathrm{V}_{\mathrm{UCOM}}$ changes the bound state energies relative to the threshold and hence alters the energy of the emitted γ-ray and thereby its wave number, k_γ in equation (2.140). As can be seen from this equation, the cross section for dipole transitions has a k_γ^3 dependence and for quadrupole transitions a k_γ^5 dependence. If there is an increase in k_γ due to a bound state moving down in energy, this phase space factor will lead to an increase in the cross section. However, the bound state is then deeper in the potential well and hence has a larger Coulomb barrier to overcome, therefore its tail will have a lower amplitude than before at any chosen point under the Coulomb barrier. This will cause the transition matrix element to become smaller and as the cross section depends on the square of the transition matrix element, this will lead to a decrease in the cross section which will compete with the increase caused by the phase space factor.

The interplay of these two effects means that fine-tuning the FMD correction is more a method to correct for three and higher-body forces lacking in the interaction, rather than a parameter that can be tuned to obtain the correct cross section. Fine-tuning the interaction also of course alters the energies of the clusters and therefore the threshold energy. Therefore the whole calculation including recalculating the matrix elements must be, and is, repeated with the new interaction used throughout to be consistent. However if the changes to the interaction are small then changes to the cluster properties should also be small and indeed this can be seen to be the case here by comparing the rows in table 4.1.

Using the same model spaces as in figure 4.1 but with the LS tuned interaction, gives the blue and red spectra in figure 4.2. If the interaction is tuned to also

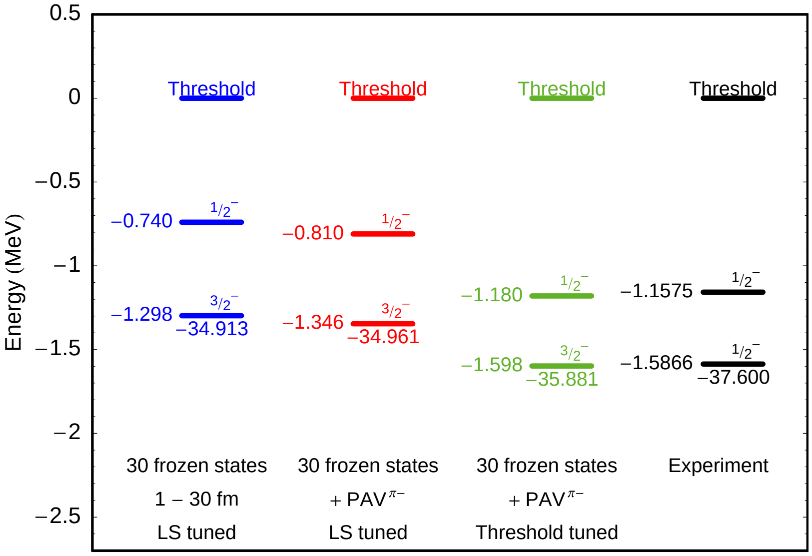

Figure 4.2.: Energy spectra for the bound states in ^{7}Be calculated using different tunings of the AV18 interaction. Results calculated using 30 frozen states placed at relative distances from 1 to 30 fm in steps of 1 fm (blue levels) and then including a PAV$^{\pi-}$ state (red levels). Tuning the interaction to obtain the correct binding energies relative to the threshold gives the green spectrum. The experimental data are taken from [45].

ensure that the energy gap between the threshold and bound states is as close as possible to experiment then the green spectrum is obtained, results using this tuning of the interaction will be denoted by “threshold tuned”. As can be seen from figure 4.2, the fine-tuning of the interaction has lead to a marked improvement in the splitting between the two bound states. Tuning the FMD correction to the interaction with respect to the threshold is then successful in reproducing the experimental bound state energies with respect to the threshold. However in absolute terms, there is still ≈ 1.7 MeV lacking in binding energy. Looking at table 4.1, this is how much the ^{3}He cluster is lacking in binding energy. Therefore, if the description of the ^{3}He could be improved it would give extra leeway for improvement of the model space describing the ^{7}Be bound states, both without increasing the energy gap to the threshold and with more physical motivation than having to tune the interaction. This improvement would have to be done in such a way that the ^{3}He remained axially symmetric, so that this property could be exploited to reduce the computing time for the matrix elements. Another point to notice from table 4.1 is that the ^{3}He charge radius is too small even though the nucleus is underbound, this needs to be investigated further.

Both of the goals mentioned above could possibly be achieved by using a superposition of Slater determinants that were simply scaled in radius. They would

1 Gaussian per nucleon FMD using AV18	E_R (MeV)		Γ (MeV)	
	$\frac{7}{2}^-$	$\frac{5}{2}^-$	$\frac{7}{2}^-$	$\frac{5}{2}^-$
$\mathrm{V}_{\mathrm{UCOM}}$ LS tuned	4.17	5.14	1.05	2.52
$\mathrm{V}_{\mathrm{UCOM}}$ threshold tuned	4.08	4.84	0.99	2.01
Experiment [45]	2.98 ± 0.05	5.14 ± 0.10	0.175 ± 0.007	1.2

Table 4.2.: The energies E_R and widths Γ of the two lowest energy resonances in ^{7}Be, with $J^\pi = \frac{7}{2}^-$ and $\frac{5}{2}^-$. The two different tunings of the interaction shown in figure 4.2 are compared with experimental results.

then remain axially symmetric providing that their spins were all aligned along the symmetry axis between the clusters. This will be investigated in the future.

Resonance energies and widths can also be calculated using the Gamow vector method, this was performed for the lowest two resonances in ^{7}Be and gave the results shown in table 4.2.

As can be seen from table 4.2, tuning the interaction to reproduce the bound state energies relative to the threshold does not necessarily lead to the resonance parameters being properly reproduced. This inability to accurately reproduce the resonance parameters could also in part be due to the poor representation of the ^{3}He nucleus as these are known to be 'pure' ^{3}He, ^{4}He resonances [45]. Although the resonance energy of the $\frac{5}{2}^-$ state is perfectly reproduced by the LS tuned interaction looking at the large overestimate of the resonance width, (over twice the experimental value), this seems to be a coincidence rather than meaning that the resonance is correctly described.

The nuclear phase shifts for these two resonances provided by the two tunings of the interaction are shown in figures 4.3 and 4.4. The agreement between the phase shift method and Gamow method for obtaining resonance parameters has been established by Timo Milosic [26] and Alberto Cribeiro [7] therefore it is no surprise that the same features are apparent in both the phase shifts and the Gamow vector results shown in table 4.2. Both of the resonances' calculated widths are too large and the splitting between the two levels is too small. Hence either the spin orbit splitting between the levels is too small or the model space just does not describe the resonances (especially the $\frac{7}{2}^-$) well enough.

There is a second $\frac{7}{2}^-$ resonance at an energy of about 4.5 MeV above the threshold; interference with this state may well explain the rise in the experimental phase shift around this region. The state has an additional decay channel into ^{6}Li+p [45], this channel is not included in the FMD model space as coupled channel calculations cannot be performed at present, hence its contribution is not seen in the FMD phase shifts.

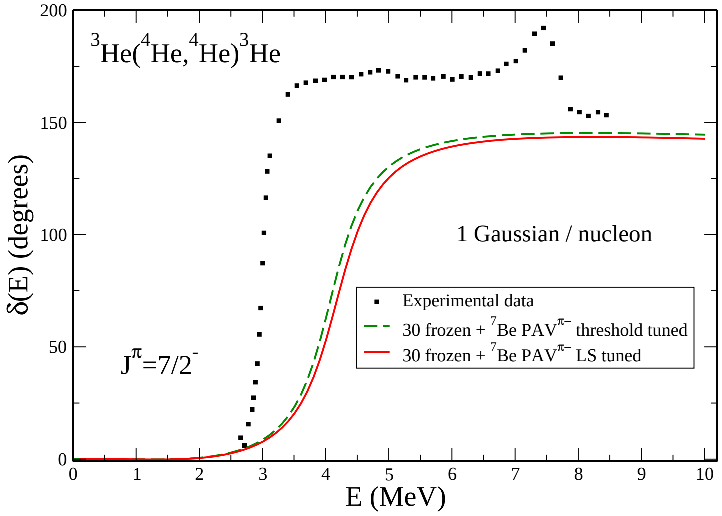

Figure 4.3.: The nuclear phase shifts are plotted against scattering energies for the $\frac{7}{2}^{-}$ channel for $^{3}\mathrm{He}(\alpha,\alpha)^{3}\mathrm{He}$ elastic scattering, described with 1 Gaussian per nucleon, for the two tunings of the interaction discussed previously. Experimental data extracted from [42]. Points taken every 0.1 MeV, so the line is just joining the points.

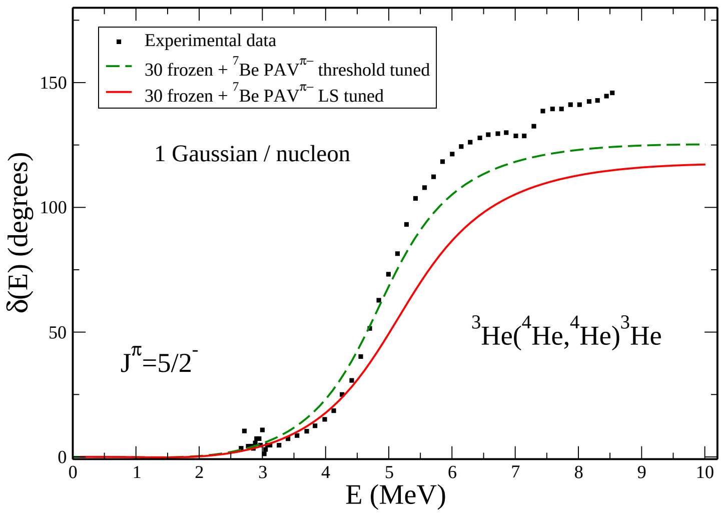

Figure 4.4.: The nuclear phase shifts are plotted against scattering energies for the $\frac{5}{2}^{-}$ channel for $^{3}\mathrm{He}(\alpha,\alpha)^{3}\mathrm{He}$ elastic scattering described with 1 Gaussian per nucleon, for the two tunings of the interaction discussed previously. Experimental data extracted from [42].

In figure 4.5, the non-resonant phase shifts for the LS tuned interaction using the same model space are compared to experiment. Through electric dipole (E1) transitions these scattering states give by far the largest contribution to the radiative capture cross section.

In figure 4.7, the cross section for the radiative capture reaction: $^3\mathrm{He}(\alpha,\gamma)^7\mathrm{Be}$ is shown. At a maximum the difference in the cross section between the two results is more than a factor of 100. This requires more investigation to discover more about the differences between the scattering and bound states in each case.

As can be seen from figure 4.7, in both cases the cross section changes very rapidly at astrophysically small energies, with such a drastic energy dependence in the energy range of interest it is almost impossible to make useful comparisons to experimental data or between different theoretical models. Therefore the astrophysical S-factor is an essential tool in making these comparisons and also in trying to extrapolate experimental data and theoretical models to zero energy. Before we go on to calculate the S-factor, we will first try to improve the matching to the phase shift data by using two Gaussians per nucleon.

4.1.2. Two Gaussians per nucleon

As already mentioned, a first attempt at improving the description of the clusters can be made by using two Gaussians to describe each nucleon, the multiconfiguration calculation can then repeated for the new cluster states and $\mathrm{PAV}^{\pi-}$ state. The same LS tuned interaction and an interaction tuned to the new threshold were used, the second of these will be referred to from now on as "threshold tuned G2".

Looking at table 4.3, there is an improvement over the one Gaussian description especially in the charge radius of the ^{3}He, this is not surprising as the second Gaussian is much wider than the first after minimisation of the single particle parameters and can therefore better describe the diffuse tail of the density for the relatively weakly bound ^{3}He nucleus. However there is still over an MeV of binding energy missing from the ^{3}He cluster, this will be investigated in the future by using multiple Slater determinants to describe the nucleus.

If we now consider the non-resonant phase shifts, shown in figure 4.6, and compare them to those calculated with one Gaussian per nucleon from figure 4.5, the agreement with the experimental data is slightly worse. In all cases the agreement with the data at higher energies seems to deteriorate, the data for the $\frac{3}{2}^+$ and $\frac{5}{2}^+$ channels seem to have some problems with interference from other channels, however on average the phase shifts seem to lie around zero degrees across the whole energy range.

In figure 4.8 the total S-factor for each interaction and model space is plotted

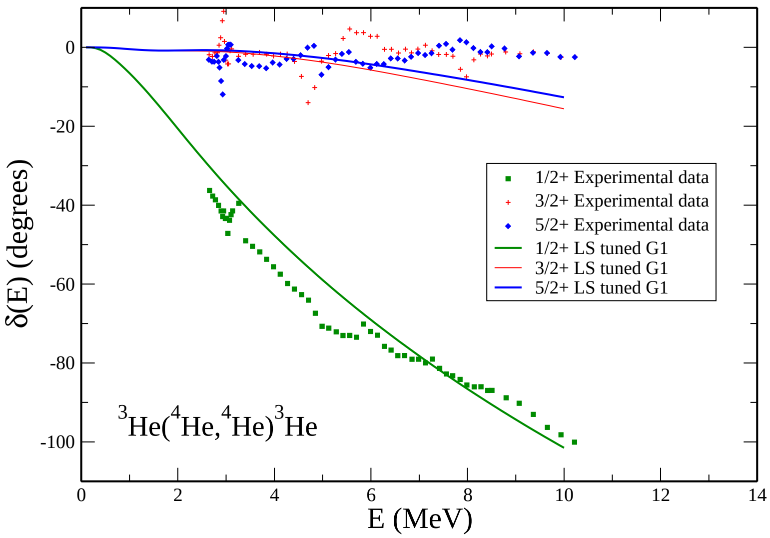

Figure 4.5.: Phase shifts for the non-resonant channels in ^{3}He$(\alpha,\alpha)^3$He elastic scattering with one Gaussian per nucleon for the LS tuned interaction.

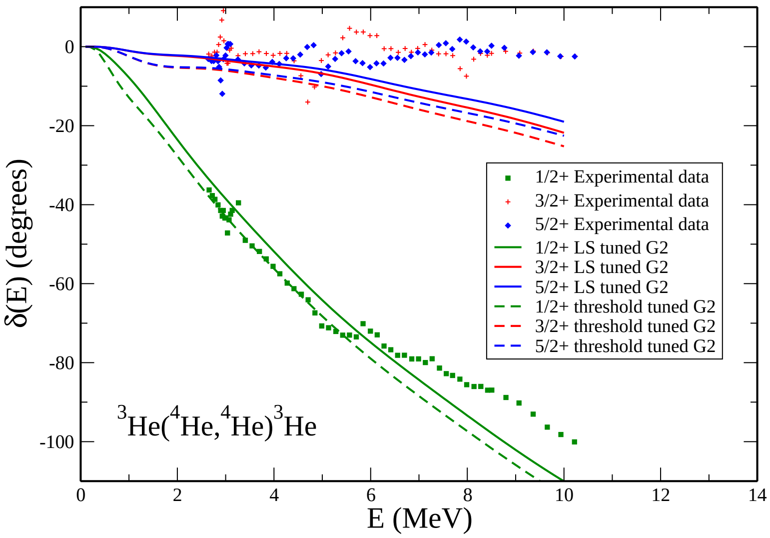

Figure 4.6.: Phase shifts for non-resonant channels for ^{3}He$(\alpha,\alpha)^3$He elastic scattering with two Gaussians per nucleon and employing the LS tuned interaction as well as the threshold tuned G2 interaction.

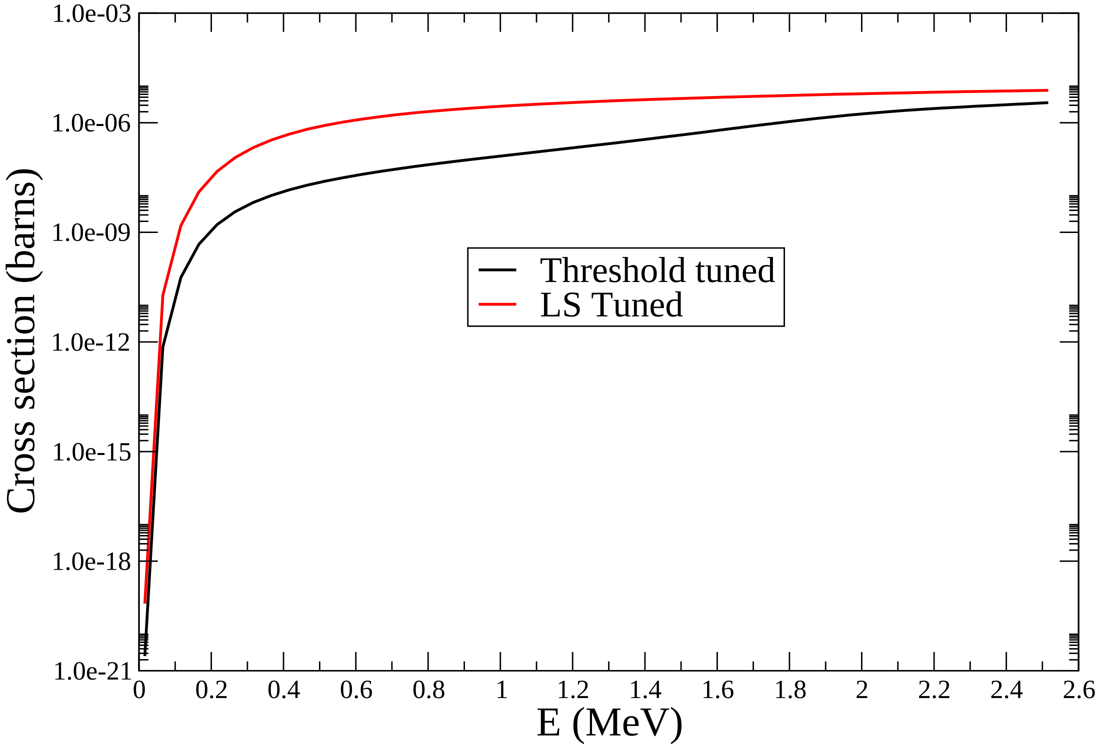

Figure 4.7.: Cross section for the radiative capture reaction: $^3\mathrm{He}(\alpha,\gamma)^7\mathrm{Be}$, using 1 Gaussian per nucleon, for two different tunings of the FMD correction to the $\mathrm{V}_{\mathrm{UCOM}}$ potential.

against the current body of experimental data. For each case the sum of the S-factors from all the five possible E1 tranistions is shown: $\frac{5}{2}^+ \to \frac{3}{2}^-$, $\frac{3}{2}^+ \to \frac{3}{2}^-$, $\frac{3}{2}^+ \to \frac{1}{2}^-$, $\frac{1}{2}^+ \to \frac{3}{2}^-$ and $\frac{1}{2}^+ \to \frac{1}{2}^-$. Also included in figure 4.8 is a plot of the S-factor with frozen states up to 45 fm included in the otherwise same model space and with the same LS tuned interaction as before, this is labelled as “LS tuned d1-45”. This was done to demonstrate that the main part of the transition matrix element is already included in a model space up to 30 fm, hence there is only a difference of about 30 eV barn in the zero-energy S-factor between the two model spaces. This small difference is probably due to the bound state approximation being used rather than matching to the Whittaker function which causes the wave function to go to zero rather than a finite albeit small value at the edge of the model space. The matching to the Whittaker function should be implemented to give the correct slope of the S-factor at very low energies and hence allow for correct extrapolation to deduce $S(0)$, the S-factor at zero energy. This comparison was only performed in the 1 Gaussian per nucleon calculation due to the more than doubling of the number of matrix elements that are required to be calculated in the larger model space (c.f. 46×46 and 31×31). As the vast majority of the computational effort for these calculations is spent in calculating

2 Gaussians per nucleon FMD using AV18	charge radius (fm)		E_0 (MeV)	
	^{4}He	^{3}He	^{4}He	^{3}He
V_{UCOM} LS tuned	1.688	1.882	-28.332	-6.686
V_{UCOM} threshold tuned G2	1.688	1.882	-27.882	-6.526
Experiment [46][47]	1.671 ± 0.014	1.976 ± 0.015	-28.296	-7.718

Table 4.3.: Mass radii and ground state energies for ^{4}He and ^{3}He clusters calculated using two Gaussians per nucleon and the AV18 interaction with two tunings of the FMD correction.

the matrix elements, it seemed unnecessary to repeat the larger model space calculation also in the two Gaussians per nucleon case.

The fact that the calculated S-factor in the case of the "Threshold tuned" results in 4.8 is higher than for the "LS tuned" ones can be explained in the following way. From figure 4.1 it can be seen that the bound states are lower for the "Threshold tuned" interactions, therefore the energy of the emitted γ-ray will be higher. As the cross section goes as E_γ^3 for dipole transitions, even a small difference will sharply increase the cross section at a particular scattering energy and hence the S-factor.

The S-factor in all cases is consistently too high, this requires further investigation, but at the moment, the main inaccuracy in our description of the capture reaction is in the description of the ^{3}He cluster. The next step to improve the calculation will be to describe this cluster with a superposition of Slater determinants whose radii are scaled, hopefully this will lead to the gap between the threshold and bound states being better reproduced without recourse to tuning the interaction and hence possibly to a better estimation of the S-factor. It would also be more than possible to add to the part of the model space describing the compound nucleus ^{7}Be as this is effectively done by just the PAV$^{\pi-}$ state in all these calculations, as well as a small contribution from the first couple of frozen states. This would be even more sensible if the description of the clusters were improved as mentioned above, as it is important to keep the quality of the description of both the compound nucleus and the asymptotic states somewhat on an equal footing for the consistency of the approach to be preserved.

This should however already be regarded as an excellent result; with a totally microscopic and unified nuclear many-body method, with no free parameters apart from a small adjustment to a phenomenological correction in the interaction, the S-factor is calculable in a small set of very simple FMD many-body states to well within a factor of two of the latest experimental results.

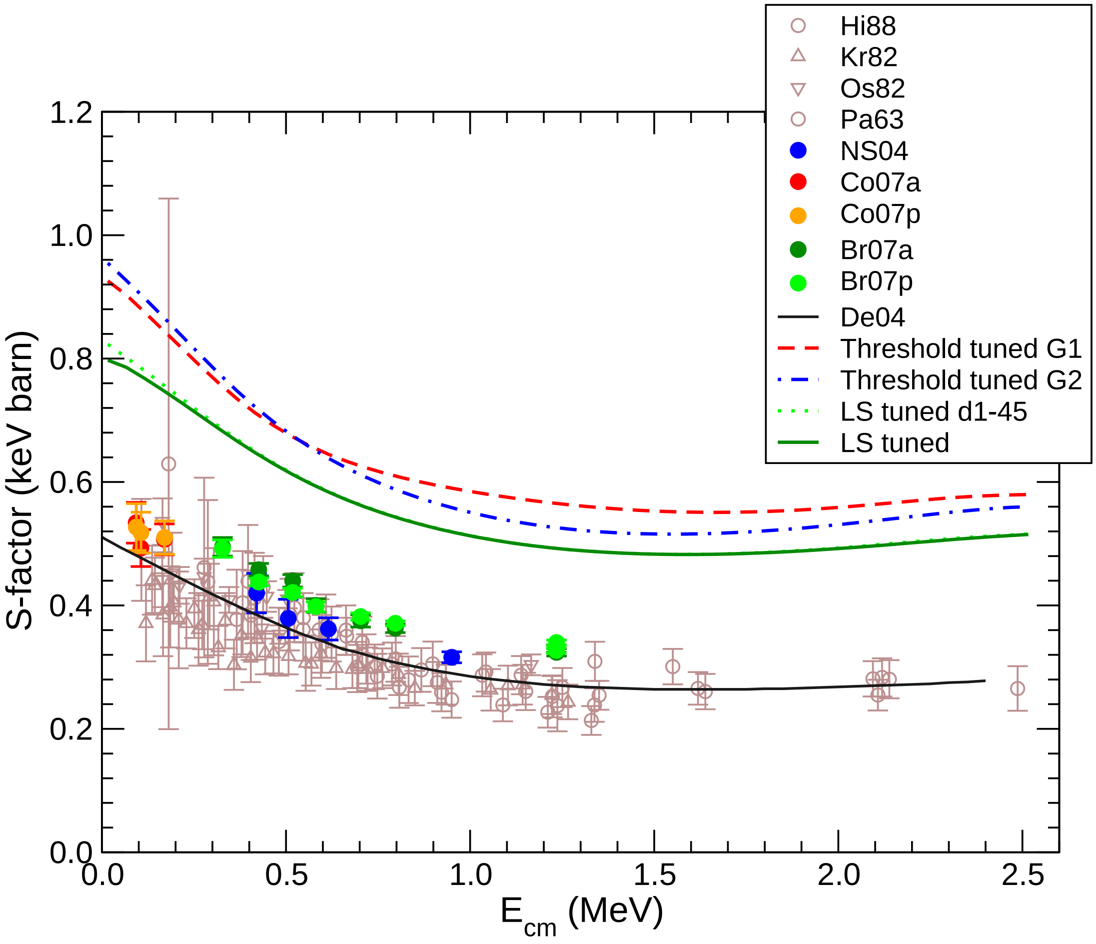

Figure 4.8.: The total S-factor for ^{3}He$(\alpha,\gamma)^7$Be for the aforementioned different model spaces and interactions plotted against the currently available experimental data. Hi88:[20], Kr82:[24], Os82:[32], Pa63:[33], NS04:[41], Co07a & Co07p:[6], Br07a & Br07p:[2], and De04:[8].

4.2. ^{14}C$(\alpha,\gamma)^{18}$O

It is thought that the chain of reactions ^{14}N$(e^-,\gamma)^{14}$C$(\alpha,\gamma)^{18}$O, or NCO chain as it is often called, could be important to determine the onset of a helium flash in the core of a red giant star. Therefore this reaction rate has a number of consequences that can be observed directly in observational astronomy, as it affects the core mass at the time of the onset of the helium flash and this in turn affects the luminosity of the star. This reaction can also take place under highly degenerate conditions in white dwarf stars.

As always, the first step in performing these calculations is to decide on what should be included in the model space. In this case, twenty frozen states at regular spacings from 1 to 20 fm were constructed from minimised ^{14}C and ^{4}He clusters. The description of the compound ^{18}O nucleus is much more complex than that of ^{7}Be because the bound state spectrum is far more complicated. Due to the 11 extra nucleons, the large amount of extra computing time this entails also means that the states chosen to be part of the model space must be carefully selected to ensure that they bring something new to the model space.

In the end 7 extra interaction states were decided upon to add to the 20 frozen states and form the model space for this calculation. They were obtained by minimising the many-body state under different constraints some with and some without parity projection during minimisation. Cuts through their single particle densities in the yz plane represented in coordinate space are shown in figure 4.9. These seven states were selected by requiring that they had less than a 95% overlap with any of the states already selected, with the frozen states being included by default as they are required to describe the asymptotic scattering behaviour. They were also chosen in each case to try and improve the description of a particular state in the compound nucleus, states which were believed to be important in the description of the capture reaction.

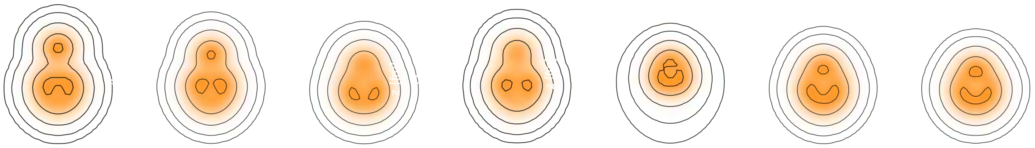

Figure 4.9.: Single particle densities of interaction states used in the calculation of the $^{14}\mathrm{C}(\alpha,\gamma)^{18}\mathrm{O}$ radiative capture reaction.

As can be seen from figure 4.9, there is a wide variety of states embodied in these 7 chosen ones; from very compact shapes to states in which the compound nucleus has almost dissolved and cluster structure is almost resolvable.

Using this model space the spectrum of the ^{18}O nucleus was calculated using the bound state approximation and is displayed in figure 4.10. If only the frozen states are included in the model space then the only bound state found is a 0^+ state. Adding the 7 additional interaction states enriches the bound state spectrum considerably, as expected. However at least in the bound state approximation, the seven additional states have little effect on the states above the threshold because these as scattering states clearly have much more overlap with the asymptotic frozen states. In table 4.2 the energies and widths of the resonance channels are calculated using Gamow vectors for the channels found above the threshold in the bound state approximation. They are all very similar to what was found in the bound state approximation, apart from the 4^+ state. This is unsurprising as they are very narrow resonances fairly near to the particle emission threshold, which makes them prime candidates to be approximated by

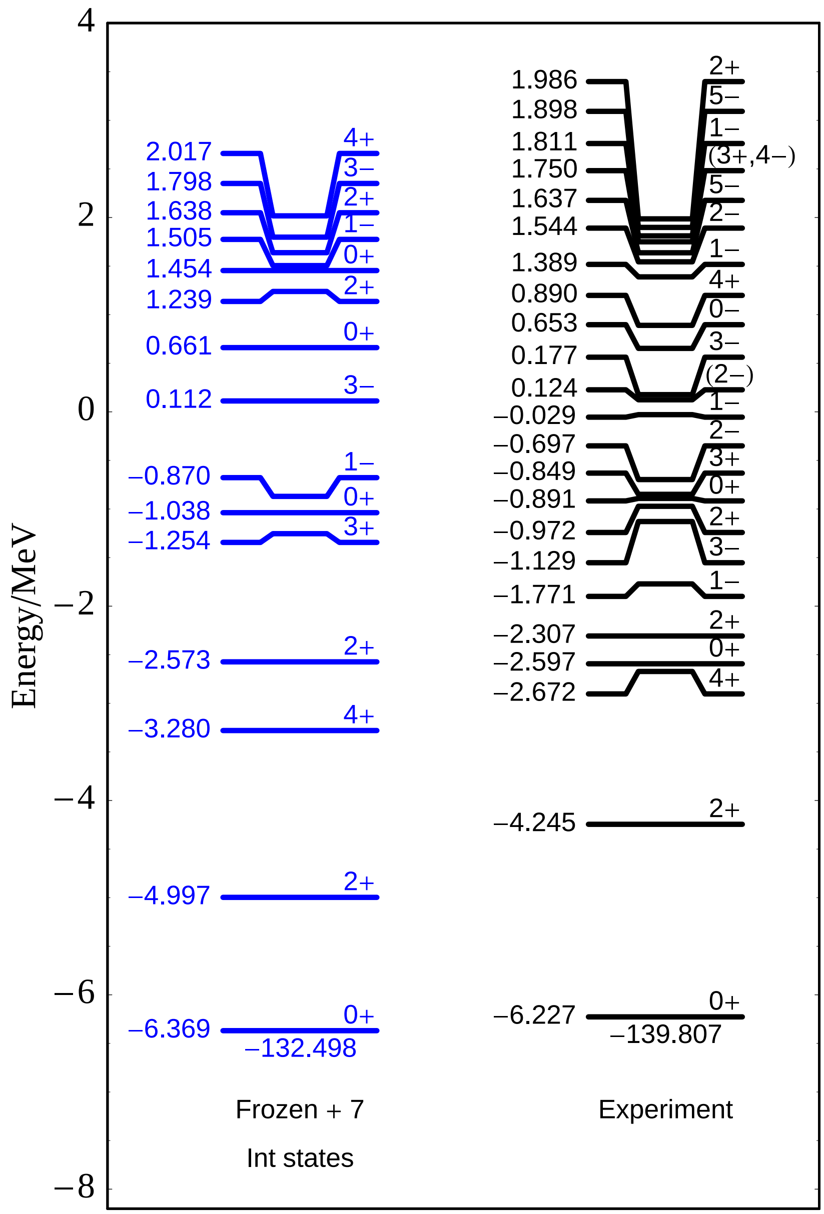

Figure 4.10.: Above: calculation of the spectrum of ^{18}O using the bound state approximation with 20 frozen states from 1 - 20 fm and including 7 interaction states. Below: resonance parameters for the states found above the threshold using the FMD model space.

J^π	3_1^-	0_3^+	2_3^+	4_2^+
E_R (MeV)	0.151	0.669	1.279	3.88
Γ (keV)	0.027	0.064	3.9	320

bound states. The 4^+ state is not so near to the threshold and also not as narrow as the others. However as this state is so far off the experimental value it is not clear if the experimental 4^+ resonance, which is thought to be important in big bang nucleosynthesis, is in our model space; or, if the observed resonance is another higher energy state found in experiment. There is a 4^+ state found in experiment at 4.068 ± 0.014 MeV above the threshold with a width of less than 50 keV. If it is this higher energy state that is seen in our model space it is at far too high energy even to be of interest in big bang nucleosynthesis and can therefore be disregarded at present.

For a relatively simple model space, the agreement with experiment is rather good aside from the overbinding of the ground state band. This overbinding has been observed in previous microscopic studies of the ^{18}O system (see [16] and [9]). The other major discrepancies between theory and experiment are the fact that there is no 0^+ state near to the experimental energy of the 0_2^+ (starting to number at 1). This either means that the 0_3^+ state that is seen as a resonance in our calculation is in fact the experimental bound 0_2^+ state very badly represented and the 0_2^+ state in our model space is the experimental 0_3^+ state which it lies close to in energy. Or the calculated ordering of the levels is correct but the energies are too high by about 1.5 MeV in both cases. Funck and Langanke [16] who have made a detailed GCM calculation of the structure of ^{18}O commented that none of the microscopic studies at the time had found the experimentally observed 0_3^+ state in their calculations. However they could not include the same variety of compact shapes that is possible using FMD with its non-orthogonal basis. They also comment that this state is known to have mainly a $(2s)^2$ configuration of the two excess neutrons outside the core. This configuration has a large overlap with one of the 7 states that was selected, for exactly this reason, to be used in the FMD model space. All of this would suggest that the first suggestion of the two above is more likely to be correct. It will have to be investigated in future how to go about better representing the experimentally observed 0_2^+ state in our model space. This is a bit of a drawback for the moment in the calculation of the S-factor as Funck and Langanke [16] claim that this state makes a large contribution to the direct capture cross section.

As an interesting aside, the rate calculated in [16] has been used in calculating implications to astrophysical environments [48] [18]. The largest unknown throughout the calculation is the α-width Γ_α of the 3_2^- resonance near to the threshold as this has not been measured. In [16] Γ_α is taken to be 2.87×10^{-18} MeV then the argument is used that the resonance strength $\omega\gamma = (2J+1)\frac{\Gamma_\alpha \Gamma_\gamma}{\Gamma_{tot}}$ is determined solely by Γ_α as this will be much smaller than Γ_γ, giving $\omega\gamma = 7\Gamma_\alpha$. However if Γ_α were actually to be closer to the value of 27 eV as found in our calculations and shown in 4.2, then assuming a total Γ_γ width of the order of eV for all possible γ-transitions [35], then $\omega\gamma \approx (2J+1)\frac{10^{-5}\times10^{-6}}{11^{-5}} \approx 10^{-7}$ MeV. This is as opposed to the figure of 2.1×10^{-17} MeV that was used in [16]. This is an enormous correction and may well point to a problem in the calculation of very small resonance widths using the method outlined here. This could be due to the commutators calculated in the matching to the Coulomb wave functions involving very small numbers and hence causing numerical problems. Indeed the method described at the end of the chapter 3 does not agree on this width, it gives a much higher value, which points to numerical problems. More investigations need to be conducted to see if this width can be calculated by a more robust method as it could have important astrophysical consequences especially in the onset of helium flashes in white dwarves.

Proceeding with the current model space, the S-factor can be calculated for electric dipole (E1), quadrupole (E2) and magnetic dipole (M1) transitions, higher order multipoles being negligible at astrophysical energies.

The transitions that are available in our chosen model space for a 0^+ initial scattering state are: via the E1 transition the clusters can be captured into the 1^-_1 bound state or via the E2 transition into either the 2^+_1 or 2^+_2 bound state; there being no available 1^+ bound state to capture to via an M1 transition. In our model space, as discussed above, there is a 0^+_3 state that does not appear in the experimental spectrum. The method described above for calculating the non-resonant scattering cross section works very well in reactions such as $^3\mathrm{He}(\alpha,\gamma)^7\mathrm{Be}$ where there is no resonance in the same channel within the energy range of interest. However when there is a resonance present as is the case for the 0^+ channel in this case, the S-factor has behaviour as shown in figure 4.11. Hence the non-resonant cross section, the 1^-_1 part of which could be important at low energies, is totally drowned out by the spurious resonance. This obviously makes the calculation of a separate non-resonant cross section including this channel impossible without some extrapolation of the non-resonant contribution that can be seen from about 8 MeV upwards in figure 4.11.

The S-factors for all the channels have been plotted to much higher energy (10 MeV) than needed in astrophysical scenarios. This is to show the resonance tails that influence the S-factor over a large energy range, upon viewing only a small part of the energy range the effect of these tails is not so obvious. Looking at the situation for an incoming state with $\mathrm{J}^\pi = 1^-$ shown in figure 4.12, the influence of the tail of the sub-threshold 1^- resonance seen in figure 4.10 on the S-factor can be seen, again making it difficult to determine a non-resonant contribution. Similar effects due to resonance states are exhibited by the S-factors plotted in figures 4.13, 4.14 and 4.2. It does seem that the 1^- incoming channel has a large non-resonant contribution at low energies leading to the relatively flat S-factor in figure 4.12, of the order of 100s of keV barn, as opposed to other channels which seem to be of the order of 0.1 - 1 keV barn. This would fit with the idea that the s- and p- scattering waves should dominate in accordance with the lower centrifugal barrier they must traverse in comparison to higher ℓ-values. However even this channel seems to have some resonant influence around 6 MeV and it is not clear exactly how this affects the S-factor at lower energies.

By penetration arguments alone, the 0^+ incoming channel should have a comparable if not larger non-resonant contribution than the 1^- state. Yet the lower part of figure 4.11 seems to show the largest contribution, a $0^+ \rightarrow 1_1^-$ transition, as having a non-resonant S-factor of only ≈ 0.2 keV barn. There are then two E2 transitions to the 2_1^+ and 2_2^+ states, but the non-resonant S-factors for these final states are a factor of 100 or so smaller than for the 1_1^- final state. Therefore the 0^+ incoming channel seems to contribute far less than the 1^- channel to the total non-resonant S-factor. One reason for this is probably that the chosen FMD model space is missing the 2_3^+ state claimed in [16] to have strong α-clustering. This state, if present in the model space, might give a large E2 contribution to the non-resonant S-factor and hence make the 0^+ and 1^- incoming channels' contributions comparable in size.

It might be possible to exclude some multipoles by grouping the data according to the multipole of the transition. Therefore in figures 4.15, 4.16 and 4.17 the S-factor for each of the multipoles considered in these calculations is plotted.

Looking at these plots, although the E1 transitions do seem in general to have higher S-factors for the non-resonant part of each channel in the energy range of astrophysical interest, the non-resonant contribution to the cross section is swamped by the contributions from resonances, making it unclear what can and cannot be reasonably excluded.

One solution to the problem of separating the different components would be to not separate them and to calculate a total reaction rate per particle pair. Then to approximate the resonant states as is done for example in [16] and to subtract their contribution from the total reaction rate. The non-resonant contribution from channels with spurious resonances such as the 0_3^+ would have to be extrapolated through to zero energy to remove the spurious resonant contribution. This will be studied further in the future.

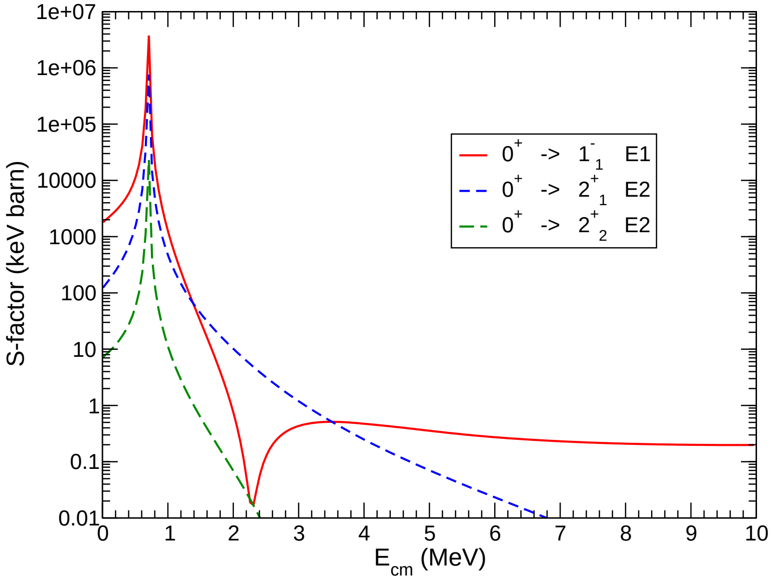

Figure 4.11.: S-factor for $^{14}C(\alpha,\gamma)^{18}O$ showing the possible radiative capture channels open to a 0^+ incoming state in the FMD model space. Plotted above on a logarithmic scale to show the resonant contributions due to the spurious 0^+_3 state appearing in the FMD model space and below the same plot magnified on the y-axis to show the non-resonant contributions visible at higher energies.

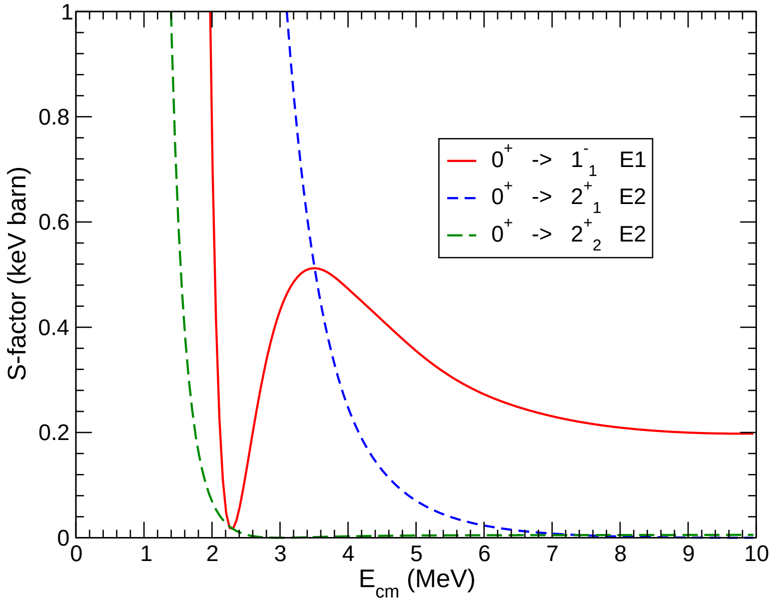

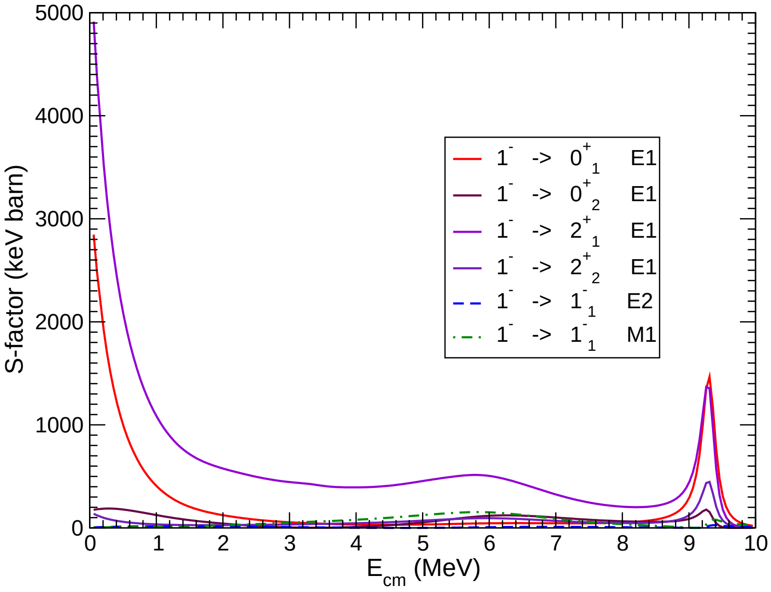

Figure 4.12.: Above: S-factor for ^{14}C(α,γ)^{18}O showing the possible radiative capture channels open to a 1^- incoming state in the chosen FMD model space. Below: the same but for a 4^+ incoming state.

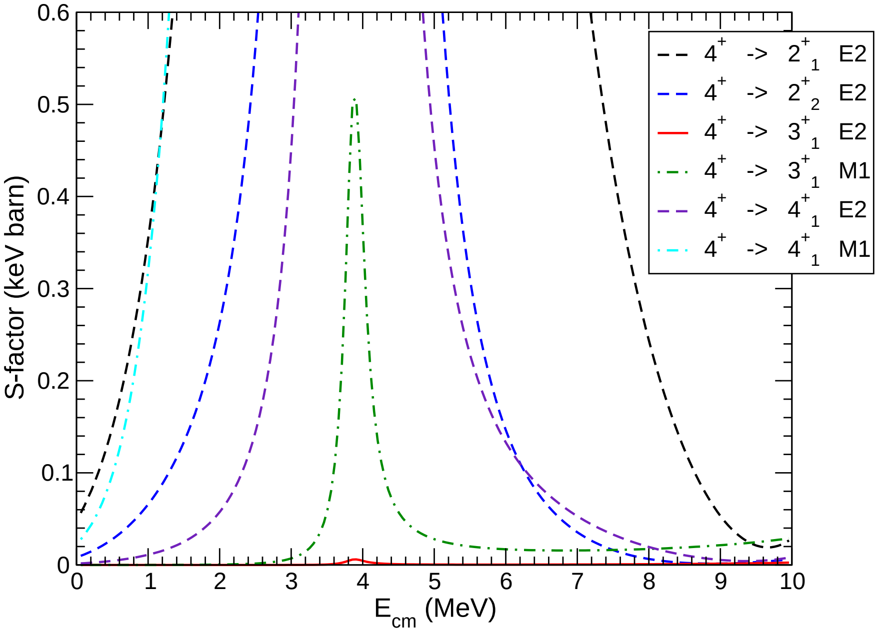

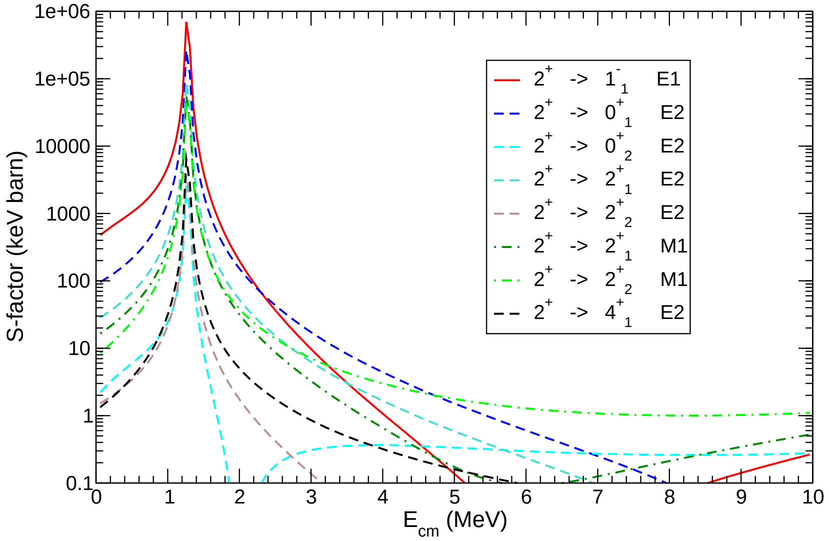

Figure 4.13.: S-factor for ^{14}C$(\alpha,\gamma)^{18}$O showing the possible radiative capture channels open to a 2^+ incoming state in the chosen FMD model space. Plotted above on a logarithmic scale to show the resonant contributions due to the 2^+_3 state appearing in the FMD model space and below the same plot magnified on the y-axis to show the non-resonant contributions.

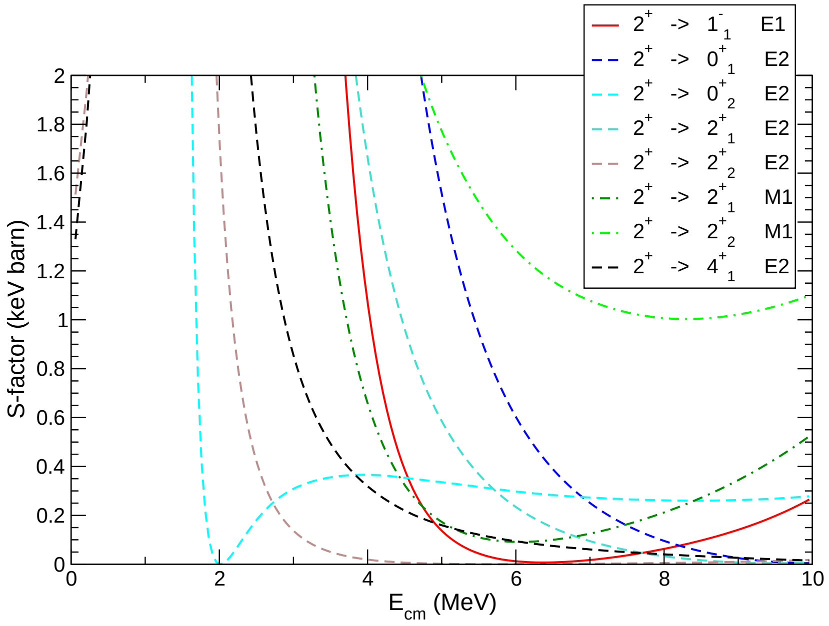

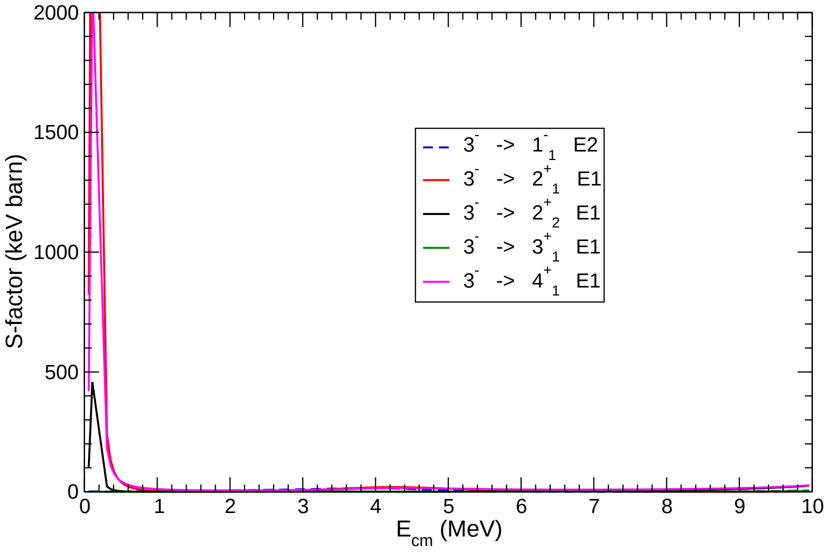

Figure 4.14.: S-factor for $^{14}\mathrm{C}(\alpha,\gamma)^{18}\mathrm{O}$ showing the possible radiative capture channels open to a 3^- incoming state in the chosen FMD model space. Plotted above on a logarithmic scale to show the resonant contributions due to the spurious 0^+_3 state appearing in the FMD model space and below the same plot magnified on the y-axis to show the non-resonant contributions.

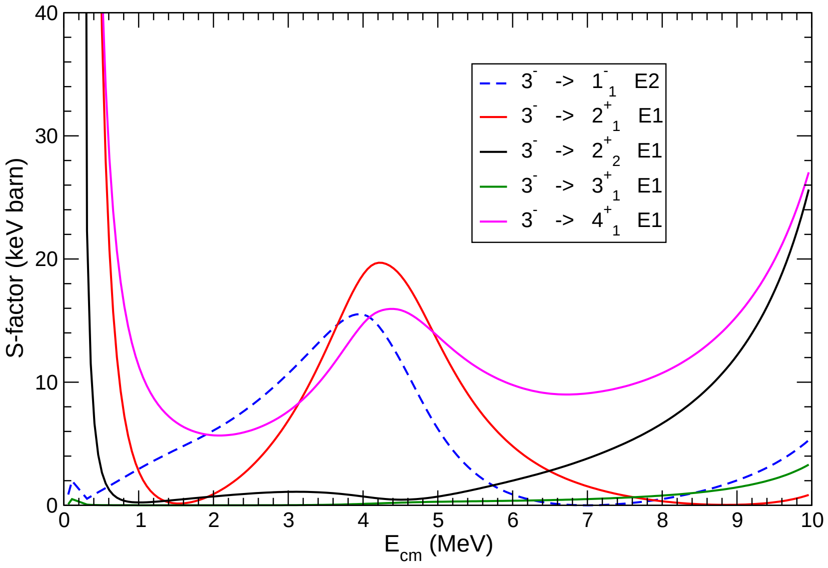

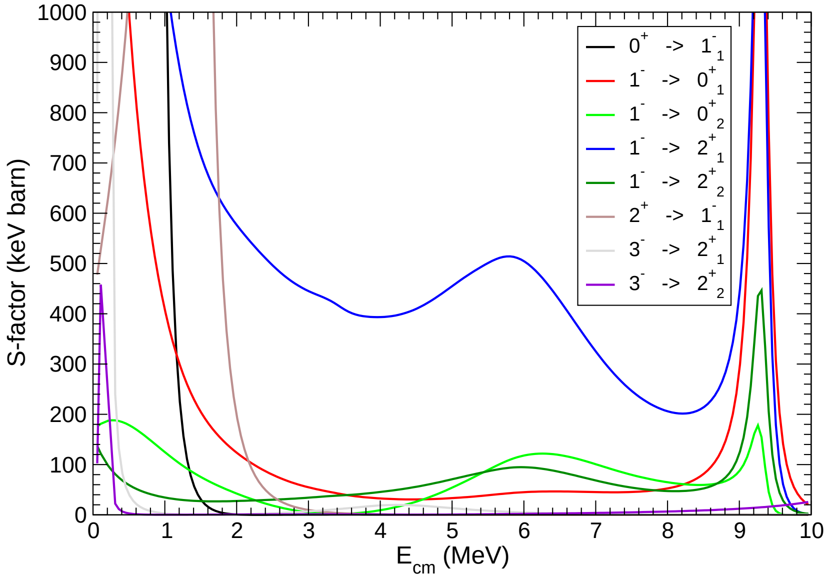

Figure 4.15.: The S-factor for all the possible E1 transitions in the chosen FMD model space.

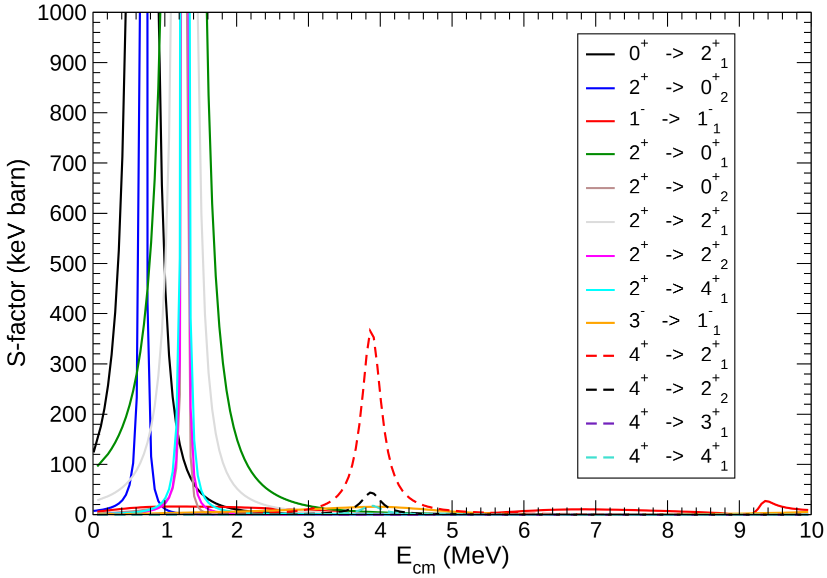

Figure 4.16.: The S-factor for all the possible E2 transitions in the chosen FMD model space.

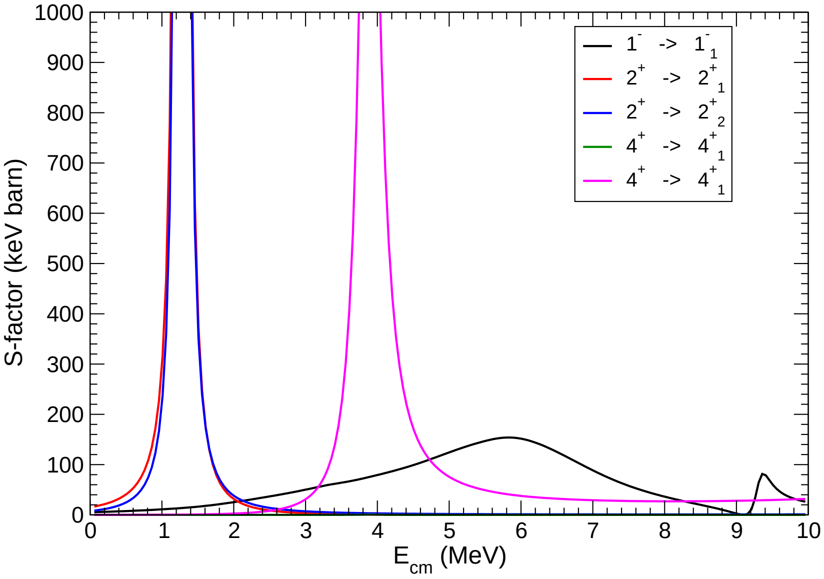

Figure 4.17.: The S-factor for all the possible M1 transitions in the chosen FMD model space.

5. Conclusions and outlook

The combination of the versatile FMD basis, making use of the correlated realistic potential V_{UCOM}, with the new Collective Coordinate Representation has been effectively applied to radiative capture reactions. With more investigations into appropriate model spaces and certain extensions to the code, this seems a promising fully microscopic and unified method that could in the future offer real predictive power for astrophysical reactions that are unreachable in the laboratory.

The work presented in this thesis has a lot of potential to be extended to other reactions and also to other types of reactions. With the present computing power available at GSI the calculations are limited to the sd-shell, but this will be able to be extended in the future with faster computers. The method could also be extended to calculate:

- Particle exchange reactions
- Coupled channel reactions
- Reactions requiring double projection
- Improved description of asymptotics of bound states by matching to Whittaker functions

To extend the method to particle exchange reactions would only involve calculating the transition from one scattering state to another, both of which could be calculated using FMD. This would make the model applicable to a large range of reactions of great astrophysical interest.

Incorporating the calculation of coupled channel reactions would enable the size of the model space to be increased probably in a very beneficial way in a number of cases. In [16] for example the description of the scattering was improved by adding in the ${}^{17}\mathrm{O}\,(n,\gamma)\,{}^{18}\mathrm{O}$ channel. In the FMD calculation it was possible to compensate in some part for this omission because interaction states as well as cluster configurations could be included in the model space. Including certain deformations of ${}^{18}\mathrm{O}$ can go some way to providing overlap with missing asymptotic states. However, for example in considering a reaction such as ${}^{12}\mathrm{C}\,(\alpha,\gamma)\,{}^{16}\mathrm{O}$ it would be necessary to include the 2^+ excitation of ${}^{12}\mathrm{C}$ to properly describe the reaction. This reaction actually exhibits other problems that are more difficult to surmount at the moment.

In cases such as $^{12}\mathrm{C}\,(\alpha,\gamma)\,^{16}\mathrm{O}$ where one or both of the interacting nuclei are deformed, the cluster state(s) must first be projected on angular momentum then the projected states must be used to create each of the frozen states. This double projection at the moment makes the computing time for such reactions unfeasible.

To improve the asymptotics of the bound states in the radiative capture reactions considered, the bound state wave function should be matched to the Whittaker function of the second kind outside the range of the nuclear interaction; as is done using the Coulomb wave function for the scattering states. This should be easily implementable using the same method as is used to search for resonances, although the search routine would be simpler as only real eigenvalues need be considered.

Lastly, S-factors for peripheral reactions in the non-resonant low energy regime could be obtained by using phase shifts and asymptotic normalisation coefficients calculated by the FMD code. These quantities could then be used to fix the exact form of the Whittaker functions and scattering states, which would enable the transition matrix element and hence the cross section to be calculated. This would give an independent check of the FMD results calculated by the method described in this thesis for low energy non-resonant reactions.

A. Appendix

A.1. Derivatives of the Coulomb wave function in the asymptotic region

As mentioned earlier, beyond the range of the nuclear interaction the clusters can be regarded to a good approximation as point charges moving in a Coulomb potential with an orbital angular momentum ℓ. The Hamiltonian of the system is then given by:

$$\underset{\sim}{H} \quad \overset{r\to\infty}{\Longrightarrow} \quad -\frac{1}{2\mu}\frac{d^2}{dr^2} + \frac{1}{2\mu}\frac{\ell\,(\ell+1)}{r^2} + \frac{Z_1 Z_2 e^2}{r} \ , \tag{A.1}$$

whose commutator with $\underset{\sim}{r}^2$ then has the form:

$$\begin{aligned} i[\underset{\sim}{H},\underset{\sim}{r}^2] &= -\frac{i}{2\mu}\ \left[\frac{d^2}{dr^2}\underset{\sim}{r}^2 - \underset{\sim}{r}^2\frac{d^2}{dr^2}\right] \\ &= -\frac{i}{2\mu}\ \left[\frac{d}{dr}\left(2\underset{\sim}{r} + \underset{\sim}{r}^2\frac{d}{dr}\right) - \underset{\sim}{r}^2\frac{d^2}{dr^2}\right] \\ &= -\frac{i}{2\mu}\left(2 + 4\underset{\sim}{r}\frac{d}{dr}\right) = -\frac{i}{\mu}\left(1 + 2\underset{\sim}{r}\frac{d}{dr}\right) \ , \end{aligned} \tag{A.2}$$

which it is easy to verify is nothing but:

$$i[\underset{\sim}{H},\underset{\sim}{r}^2] = \frac{\{\underset{\sim}{k},\underset{\sim}{r}\}_+}{\mu} = \frac{\underset{\sim}{k}\underset{\sim}{r} + \underset{\sim}{r}\underset{\sim}{k}}{\mu} \ . \tag{A.3}$$

Powers of the commutator are then given by:

$$[\underset{\sim}{H},\underset{\sim}{r}^2]^s = \left(-\frac{1}{\mu}\right)^s \left(1 + 2\underset{\sim}{r}\frac{d}{dr}\right)^s \ . \tag{A.4}$$

Using the binomial theorem

$$\begin{aligned}\left(-\frac{1}{\mu}\right)^s\left(1+2\underset{\sim}{r}\frac{d}{dr}\right)^s &= \left(-\frac{1}{\mu}\right)^s\sum_{k=0}^{s}\binom{s}{k}\left(2\underset{\sim}{r}\frac{d}{dr}\right)^{(s-k)} \\ &= \left(-\frac{1}{\mu}\right)^s\sum_{k=0}^{s}\binom{s}{k}2^{(s-k)}\left(\underset{\sim}{r}\frac{d}{dr}\right)^{(s-k)} \quad .\end{aligned} \tag{A.5}$$

Thompson and Barnett have written a Fortran routine called COULCC [44] [43], which calculates the value of the radial Coulomb wave function and its first derivative with respect to $\rho = kr$ where $k = \sqrt{2\mu E}$.[1] Applying a change of variables to the relevant part of the commutator from (A.5):

$$r\frac{d}{dr} = r\frac{d}{d\rho}\frac{d\rho}{dr} \qquad \rho = kr \qquad \frac{d\rho}{dr} = k \qquad r\frac{d}{dr} = \rho\,\frac{d}{d\rho}\ . \tag{A.6}$$

From equation (A.6) it can be seen that all the powers of $\rho\,\frac{d}{d\rho}$ up to s will be required to complete the matching.

$$\begin{aligned}\left(\rho\frac{d}{d\rho}\right)^2 &= \rho\frac{d}{d\rho} + \rho^2\frac{d^2}{d\rho^2} \\ \left(\rho\frac{d}{d\rho}\right)^3 &= \rho\frac{d}{d\rho} + 3\rho^2\frac{d^2}{d\rho^2} + \rho^3\frac{d^3}{d\rho^3} \\ \left(\rho\frac{d}{d\rho}\right)^4 &= \rho\frac{d}{d\rho} + 7\rho^2\frac{d^2}{d\rho^2} + 6\rho^3\frac{d^3}{d\rho^3} + \rho^4\frac{d^4}{d\rho^4} \\ \left(\rho\frac{d}{d\rho}\right)^5 &= \rho\frac{d}{d\rho} + 15\rho^2\frac{d^2}{d\rho^2} + 25\rho^3\frac{d^3}{d\rho^3} + 10\rho^4\frac{d^4}{d\rho^4} + \rho^5\frac{d^5}{d\rho^5} \\ \left(\rho\frac{d}{d\rho}\right)^6 &= \rho\frac{d}{d\rho} + 31\rho^2\frac{d^2}{d\rho^2} + 90\rho^3\frac{d^3}{d\rho^3} + 65\rho^4\frac{d^4}{d\rho^4} + 15\rho^5\frac{d^5}{d\rho^5} + \rho^6\frac{d^6}{d\rho^6}\ .\end{aligned} \tag{A.7}$$

Writing the coefficients for the different powers of $\left(\rho\,\frac{d}{d\rho}\right)^s$ into a matrix with s listed down the left hand side and the power of ρ^k from each term in (A.7) listed along the top gives:

---

[1] ρ, η and ℓ can all be complex parameters. This feature of COULCC is vital in calculating Gamow states as they are associated with complex eigenvalues, making k complex see section 2.3.6.

k s	1	2	3	4	5	6
1	1	0	0	0	0	0
2	1	1	0	0	0	0
3	1	3	1	0	0	0
4	1	7	6	1	0	0
5	1	15	25	10	1	0
6	1	31	90	65	15	1

From this table it can be seen that the coefficients $X_{s,k}$ can be calculated recursively using the following formula:

$$X_{s,k} = kX_{s-1,k} + X_{s-1,k-1} \; . \tag{A.8}$$

Having devised a way of calculating the coefficients, next the derivatives themselves must be calculated. This can be done using a rearranged form of the Schrödinger equation. The Schrödinger equation for two point charges is given by:

$$\left(-\frac{1}{2\mu}\frac{d^2}{dr^2} + \frac{1}{2\mu}\frac{\ell\,(\ell+1)}{r^2} + \frac{Z_1 Z_2 e^2}{r} \right) u(r) = Eu(r) \; , \tag{A.9}$$

rearranging this gives:

$$\frac{d^2}{dr^2}\,u(r) = \left(\frac{\ell\,(\ell+1)}{r^2} + \frac{2\mu Z_1 Z_2 e^2}{r} - 2\mu E \right) u(r) \; . \tag{A.10}$$

Incorporating $k = \sqrt{2\mu E}$ and repeating the change of variables from equation (A.6) gives:

$$\begin{aligned} \frac{d^2}{dr^2}\,u(r) &= \left(\frac{\ell\,(\ell+1)}{r^2} + \frac{2\mu Z_1 Z_2 e^2}{r} - k^2 \right) u(r) \\ \frac{d}{dr} = k\frac{d}{d\rho} \quad &\Rightarrow \quad \frac{d^2}{dr^2} = \frac{d}{d\rho}\frac{d\rho}{dr}\left(\frac{d}{d\rho}\frac{d\rho}{dr}\right) = \frac{d}{d\rho}\frac{d\rho}{dr}\left(k\,\frac{d}{d\rho}\right) = k^2\,\frac{d^2}{d\rho^2} \\ \frac{d^2}{dr^2}\,u(r) &= \left(\frac{\ell\,(\ell+1)}{k^2 r^2} + \frac{2\mu Z_1 Z_2 e^2}{k^2 r} - 1 \right) k^2 u(r) \; . \end{aligned} \tag{A.11}$$

Then using the definition of the Sommerfeld parameter $\eta = \mu\frac{Z_1 Z_2 e^2}{k}$ gives finally:

$$\frac{d^2}{d\rho^2}\,u(\rho) = \left(\frac{\ell\,(\ell+1)}{\rho^2} + \frac{2\eta}{\rho} - 1 \right) u(\rho) \; . \tag{A.12}$$

Therefore using the value of the wave function, calculated by COULCC, its second derivative can be calculated from equation (A.12). Taking the derivative of the last line of equation (A.12) with respect to ρ gives:

$$\frac{d^3}{d\rho^3}\,u(\rho) = \left(\frac{\ell\,(\ell+1)}{\rho^2} + \frac{2\eta}{\rho} - 1\right)\frac{d}{d\rho}\,u(\rho) - \left(\frac{2\ell\,(\ell+1)}{\rho^3} + \frac{2\eta}{\rho^2}\right)\,u(\rho)\ . \qquad \text{(A.13)}$$

Using the wave function and its first derivative, which is also obtained from COULCC, the third derivative can be calculated using equation (A.13). From this it can be seen that to calculate any higher derivatives up to s will just require the wave function and derivatives up to the power of $s-2$. Hence, this method enables the recursive calculation of any desired power of the Coulomb wave function, just by taking derivatives of (A.12). The only other requirement is that the Coulomb wave function be differentiable up to the required order; as it is smooth and continuous, this requirement is satisfied.

A.2. Non-resonant capture cross section in terms of reduced matrix elements

The starting point for deriving the cross section in a coupled basis and in terms of reduced matrix elements is equation (2.140):

$$\sigma = 8\pi\frac{\lambda+1}{\lambda\left((2\lambda+1))!!\right)^2}\,k_\gamma^{2\lambda+1}\frac{1}{(2I_1+1)\,(2I_2+1)}$$
$$\sum_{\ell=0}^{\infty}\ \sum_{M_{I_1}=-I_1}^{I_1}\ \sum_{M_{I_2}=-I_2}^{I_2}\ \sum_{\mu=-\lambda}^{\lambda}\ \sum_{M_f=-J_f}^{J_f}\ \left|\left\langle\, J_f, M_f \,\middle|\, O^\lambda_\mu \,\middle|\, \Psi, \ell, 0; I_1, M_{I_1}; I_2, M_{I_2} \,\right\rangle\right|^2\ . \qquad \text{(A.14)}$$

As the normalisation and phase factors do not change between (2.139) and (2.140) we will concentrate here on the derivation of the matrix element, which will be denoted by B. The first thing that will be done is to couple the spins of the two clusters to the total channel spin I:

$$B = \sum_{\ell}\ \sum_{M_{I_1}M_{I_2}}\ \sum_{\mu M_f}\sum_{II'}\ \sum_{M_I M_{I'}}\left\langle\, J_f, M_f \,\middle|\, O^\lambda_\mu \,\middle|\, \Psi, \ell, 0; (I_1 I_2)I, M_I \,\right\rangle$$
$$\left\langle\, J_f, M_f \,\middle|\, O^\lambda_\mu \,\middle|\, \Psi, \ell, 0; I', M_{I'} \,\right\rangle^* \left\langle \begin{matrix} I_1 & I_2 \\ M_{I_1} & M_{I_2} \end{matrix} \,\middle|\, \begin{matrix} I \\ M_I \end{matrix} \right\rangle \left\langle \begin{matrix} I_1 & I_2 \\ M_{I_1} & M_{I_2} \end{matrix} \,\middle|\, \begin{matrix} I' \\ M_{I'} \end{matrix} \right\rangle\ , \qquad \text{(A.15)}$$

where the limits on the sums have been left out to save space. Using the orthogonality relation of the Clebsch-Gordan coefficients [49]:

$$\sum_{I'M_{I'}} \sum_{M_{I_1}M_{I_2}} \left\langle \begin{matrix} I_1 & I_2 \\ M_{I_1} & M_{I_2} \end{matrix} \middle| \begin{matrix} I \\ M_I \end{matrix} \right\rangle \left\langle \begin{matrix} I_1 & I_2 \\ M_{I_1} & M_{I_2} \end{matrix} \middle| \begin{matrix} I' \\ M_{I'} \end{matrix} \right\rangle = \sum_{I'M_{I'}} \delta_{II'} \delta_{M_I M_{I'}} = 1 \; , \tag{A.16}$$

gives for the matrix element:

$$B = \sum_{\ell} \sum_{\mu M_f} \sum_{I M_I} \langle\, J_f, M_f \,|\, O^{\lambda}_{\mu} \,|\, \Psi, \ell, 0; I, M_I \,\rangle \langle\, J_f, M_f \,|\, O^{\lambda}_{\mu} \,|\, \Psi, \ell, 0; I', M_{I'} \,\rangle^{*} \; . \tag{A.17}$$

Coupling the ℓ and I to an initial total angular momentum of J_i gives:

$$\begin{aligned} B = \sum_{\ell} \sum_{\mu M_f} \sum_{I M_I} \sum_{J_i J_i'} & \langle\, J_f, M_f \,|\, O^{\lambda}_{\mu} \,|\, \Psi, (\ell I) J_i M_I \,\rangle \langle\, J_f, M_f \,|\, O^{\lambda}_{\mu} \,|\, \Psi, (\ell I') J_i' M_I \,\rangle^{*} \\ & \left\langle \begin{matrix} \ell & I \\ 0 & M_I \end{matrix} \middle| \begin{matrix} J_i \\ M_I \end{matrix} \right\rangle \left\langle \begin{matrix} \ell & I \\ 0 & M_I \end{matrix} \middle| \begin{matrix} J_i' \\ M_I \end{matrix} \right\rangle \; . \end{aligned} \tag{A.18}$$

Using the definition of the reduced matrix element:

$$\langle\, J_f, M_f \,|\, O^{(\lambda)}_{\mu} \,|\, \Psi, (\ell I) J_i M_I \,\rangle = (-1)^{2\lambda} \left\langle \begin{matrix} J_i & \lambda \\ M_I & \mu \end{matrix} \middle| \begin{matrix} J_f \\ M_f \end{matrix} \right\rangle \frac{\langle\, J_f \,||\, O^{\lambda} \,||\, \Psi, (\ell I) J_i \,\rangle}{\sqrt{2J_f + 1}} \; , \tag{A.19}$$

equation (A.18) can be written as:

$$\begin{aligned} B = \sum_{\ell} \sum_{\mu M_f} \sum_{I M_I} \sum_{J_i J_i'} & \langle\, J_f \,||\, O^{\lambda} \,||\, \Psi, (\ell I) J_i \,\rangle \langle\, J_f \,||\, O^{\lambda} \,||\, \Psi, (\ell I) J_i' \,\rangle * \\ & \left\langle \begin{matrix} \ell & I \\ 0 & M_I \end{matrix} \middle| \begin{matrix} J_i \\ M_I \end{matrix} \right\rangle \left\langle \begin{matrix} \ell & I \\ 0 & M_I \end{matrix} \middle| \begin{matrix} J_i' \\ M_I \end{matrix} \right\rangle \left\langle \begin{matrix} J_i & \lambda \\ M_I & \mu \end{matrix} \middle| \begin{matrix} J_f \\ M_f \end{matrix} \right\rangle \left\langle \begin{matrix} J_i' & \lambda \\ M_I & \mu \end{matrix} \middle| \begin{matrix} J_f \\ M_f \end{matrix} \right\rangle \\ & (-1)^{\mu} \frac{1}{\sqrt{2J_f + 1}} \frac{1}{\sqrt{2J_i' + 1}} \; . \end{aligned} \tag{A.20}$$

Using the symmetry properties of the Clebsch-Gordan coefficients [49]:

$$\begin{aligned} \left\langle \begin{matrix} J_i & \lambda \\ M_I & \mu \end{matrix} \middle| \begin{matrix} J_f \\ M_f \end{matrix} \right\rangle &= (-1)^{\lambda+\mu} \frac{\sqrt{2J_f + 1}}{\sqrt{2J_i + 1}} \left\langle \begin{matrix} J_f & \lambda \\ -M_f & \mu \end{matrix} \middle| \begin{matrix} J_i \\ -M_I \end{matrix} \right\rangle \\ &= (-1)^{\lambda+\mu} (-1)^{J_f+\lambda-J_i} \frac{\sqrt{2J_f + 1}}{\sqrt{2J_i + 1}} \left\langle \begin{matrix} J_f & \lambda \\ M_f & -\mu \end{matrix} \middle| \begin{matrix} J_i \\ M_I \end{matrix} \right\rangle \; , \end{aligned} \tag{A.21}$$

equation (A.20) can be written as:

$$\begin{aligned}B = \sum_{\ell}\sum_{\mu M_f}\sum_{I M_I}\sum_{J_i J_i'} &\left\langle\, J_f \,\middle\|\, O^\lambda \,\middle\|\, \Psi, (\ell I) J_i \,\right\rangle \left\langle\, J_f \,\middle\|\, O^\lambda \,\middle\|\, \Psi, (\ell I) J_i' \,\right\rangle^* \\ &\left\langle \begin{matrix} \ell & I \\ 0 & M_I \end{matrix} \,\middle|\, \begin{matrix} J_i \\ M_I \end{matrix} \right\rangle \left\langle \begin{matrix} \ell & I \\ 0 & M_I \end{matrix} \,\middle|\, \begin{matrix} J_i' \\ M_I \end{matrix} \right\rangle \left\langle \begin{matrix} J_f & \lambda \\ M_f & -\mu \end{matrix} \,\middle|\, \begin{matrix} J_i \\ M_I \end{matrix} \right\rangle \left\langle \begin{matrix} J_f & \lambda \\ M_f & -\mu \end{matrix} \,\middle|\, \begin{matrix} J_i' \\ M_I \end{matrix} \right\rangle \\ &(-1)^{\mu+\lambda+\mu+J_f+\lambda-J_i} \frac{\sqrt{2J_f+1}}{\sqrt{2J_f+1}} \frac{1}{\sqrt{2J_i+1}} \frac{1}{\sqrt{2J_i'+1}} \ .\end{aligned} \tag{A.22}$$

Then, using the following relation [49]:

$$\sum_{\mu M_f} \left\langle \begin{matrix} J_f & \lambda \\ M_f & -\mu \end{matrix} \,\middle|\, \begin{matrix} J_i \\ M_I \end{matrix} \right\rangle \left\langle \begin{matrix} J_f & \lambda \\ M_f & -\mu \end{matrix} \,\middle|\, \begin{matrix} J_i' \\ M_I \end{matrix} \right\rangle = \delta_{J_i J_i'} \delta_{M_I M_I} = \delta_{J_i J_i'} \ , \tag{A.23}$$

equation (A.22) can be written as:

$$\begin{aligned}B = \sum_{\ell}\sum_{I M_I}\sum_{J_i} &\left\langle\, J_f \,\middle\|\, O^\lambda \,\middle\|\, \Psi, (\ell I) J_i \,\right\rangle \left\langle\, J_f \,\middle\|\, O^\lambda \,\middle\|\, \Psi, (\ell I) J_i \,\right\rangle^* \\ &\left\langle \begin{matrix} \ell & I \\ 0 & M_I \end{matrix} \,\middle|\, \begin{matrix} J_i \\ M_I \end{matrix} \right\rangle \left\langle \begin{matrix} \ell & I \\ 0 & M_I \end{matrix} \,\middle|\, \begin{matrix} J_i \\ M_I \end{matrix} \right\rangle \frac{1}{2J_i+1} \ .\end{aligned} \tag{A.24}$$

To sum over these Clebsch-Gordan coefficients it is useful to introduce a sum over M', which is a dummy variable as it must be equal to M_I for the Clebsch-Gordan coefficients to be non-zero:

$$\sum_{M_I M'} \left\langle \begin{matrix} \ell & I \\ 0 & M_I \end{matrix} \,\middle|\, \begin{matrix} J_i \\ M' \end{matrix} \right\rangle \left\langle \begin{matrix} \ell & I \\ 0 & M_I \end{matrix} \,\middle|\, \begin{matrix} J_i \\ M' \end{matrix} \right\rangle = \frac{2J_i+1}{2\ell+1} \ , \tag{A.25}$$

Finally this gives:

$$\begin{aligned} B &= \sum_{\ell I J_i} \frac{1}{2\ell+1} \left| \left\langle\, J_f \,\middle\|\, O^\lambda \,\middle\|\, \Psi, (\ell I) J_i \,\right\rangle \right|^2 \\ \sigma &= \ 8\pi \frac{\lambda+1}{\lambda\left((2\lambda+1))!!\right)^2} \ k_\gamma^{2\lambda+1} \frac{1}{(2I_1+1)\,(2I_2+1)} \\ &\qquad \times \sum_{\ell I J_i} \frac{1}{2\ell+1} \left| \left\langle\, J_f \,\middle\|\, O^\lambda \,\middle\|\, \Psi, (\ell I) J_i \,\right\rangle \right|^2 \ , \end{aligned} \tag{A.26}$$

which is exactly equation (2.140).

A.3. Nomenclature used in this thesis

- Operators are marked throughout by a tilde underneath the operator name, for example: $\underset{\sim}{H}$.
- Vectors are marked by an arrow above them: $\vec{b}$.
- Eigenstates are wherever possible given the same letter to mark them as the operator they belong to, for example for the relative distance: $\underset{\sim}{B}$ and $\left| B; i \right\rangle$.
- All energies are given in the centre of mass frame of reference unless otherwise explicitly stated.
- The formulae throughout this thesis are given in natural units unless otherwise stated with $\hbar$ and c set equal to unity. Through a choice of scale sensible for nuclear physics, distance and time are measured in fm; energy, momentum and mass are measured in fm^{-1}, velocity is dimensionless as is the fine structure constant $\alpha = e^2$ the square of the elementary charge. Factors of $\hbar c = 197.327053$ MeV fm can then be used to convert to units more widely used in experiment.
- Matrices are denoted by a capital, bold, sans-serif letter; for example: H.
- Clebsch-Gordon coefficients are given in the form: $\left\langle \begin{matrix} j_1 & j_2 \\ m_1 & m_2 \end{matrix} \middle| \begin{matrix} J \\ M \end{matrix} \right\rangle$.
- Numbering of energy levels in spectra starts at 1, so for example, the ground state of ^{16}O would be denoted: 0^+_1.
- Subscripts and superscripts written in the normal body text are indices, when written in capitals in a Roman font they are labels, for example: n_{IN}.

Bibliography

[1] M. Abramowitz and I. Stegun, eds., *Handbook of mathematical functions*, Dover Publications, Inc., New York, 1965.

[2] T. A. D. Brown, C. Bordeanu, K. A. Snover, D. W. Storm, D. Melconian, A. L. Sallaska, S. K. L. Sjue, and S. Triambak, *$^3He+^4He \to ^7Be$ astrophysical S-factor*, Phys. Rev. C, 76 (2007), p. 055801.

[3] E. Burbidge, G. Burbidge, W. Fowler, and F. Hoyle, *Synthesis of the elements in stars*, Reviews of Modern Physics, 29 (1957), p. 547.

[4] M. Caprio, *Levelscheme: A level scheme drawing and scientific figure preparation system for mathematica*, Computer Physics Communications, 171 (2005), p. 107.

[5] R. F. Christy and I. Duck, *γ-rays from an extranuclear direct capture process*, Nuclear Physics, 24 (1961), p. 89.

[6] F. Confortola, D. Bemmerer, H. Constantini, A. Formicola, G. Gyürky, P. Bezzon, R. Bonetti, C. Broggini, P. Corvisiero, Z. Elekes, Z. Fülöp, G. Gervino, A. Guglielmetti, C. Gustavino, G. Imbriani, M. Junker, M. Laubenstein, A. Lemut, B. Limata, V. Lozza, M. Marta, R. Menegazzo, P. Prati, V. Roca, C. Rolfs, C. R. Alvarez, E. Somorjai, O. Straniero, F. Strieder, F. Terrasi, and H. P. Trautvetter, *Astrophysical S-factor of the $^3He(\alpha,\gamma)^7Be$ reaction measured at low energy via detection of prompt and delayed γ rays*, Phys. Rev. C, 75 (2007), p. 065803.

[7] A. Cribeiro, *Nuclear many-body continuum states and their boundary conditions in a collective-coordinate representation*, PhD thesis, Technische Universität Darmstadt, 2005.

[8] P. Descouvemont, A. Adahchour, C. Angulo, A. Coc, and E. Vangioni-Flam, *Compilation and R-matrix analysis of Big Bang nuclear reaction rates*, Atomic Data and Nuclear Data Tables, 88 (2004), p. 203.

[9] P. Descouvemont and D. Baye, *Multiconfiguration microscopic study of $\alpha + ^{14}C$ molecular states*, Physical Review C, 31 (1985), p. 2274.

[10] H. Feldmeier, *Fermionic Molecular Dynamics*, Nuclear Physics A, 515 (1990), p. 147.

[11] H. Feldmeier and T. Neff, *Fermionic Molecular Dynamics clusters, halos, skins and S-factors*, in Proceedings of the International School of Physics "E. Fermi", 2007.

[12] H. Feldmeier, T. Neff, and R. Roth, *Cluster structures, halos, skins, and s-factors in Fermionic Molecular Dynamics*, in Frontiers in Nuclear Structure, Astrophysics, and Reactions - FINUSTAR, 2006.

[13] H. Feldmeier, T. Neff, R. Roth, and J. Schnack, *A unitary correlation operator method*, Nuclear Physics A, 632 (1998), p. 61.

[14] H. Feldmeier and J. Schnack, *Molecular dynamics for fermions*, Reviews of Modern Physics, 72 (2000), p. 655.

[15] B. Flannery, W. Press, S. Teukolsky, and W. Vetterling, *Numerical Recipes in C: The Art of Scientific Computing (Second Edition)*, New York: Cambridge University Press, 1992.

[16] C. Funck and K. Langanke, *The* $^{14}C(\alpha,\gamma)^{18}O$ *reaction at astrophysical energies*, Astrophysical Journal, 344 (1989), p. 46.

[17] G. Gamow, *Zur Quantentheorie des Atomkernes*, Zeitschrift fur Physik, 51 (1928), p. 204.

[18] J. Görres, S. Graff, M. Wiescher, R. Azuma, C. Barnes, and T. Wang, *Alpha capture on* ^{14}C *and its astrophysical implications*, Nuclear Physics A, 548 (1992), p. 414.

[19] J. Griffin and J. Wheeler, *Collective motions in nuclei by the method of generator coordinates*, Physical Review, 108 (1957), p. 311.

[20] M. Hilgemeier, H. W. Becker, C. Rolfs, H. P. Trautvetter, and J. W. Hammer, *Absolute cross section of the* $^{3}He(\alpha,\gamma)^{7}Be$ *reaction*, Zeitschrift fur Physik, 329 (1988), p. 243.

[21] D. Hill and J. Wheeler, *Nuclear constitution and the interpretation of fission phenomena*, Physical Review, 89 (1953), p. 1102.

[22] H. Horiuchi and K. Ikeda, *Cluster Models and Other Topics*, World Scientific Publishing Company Pte Ltd, 1986.

[23] Y. Kanada-En'yo and H. Horiuchi, *Structure of Light Unstable Nuclei Studied with Antisymmetrized Molecular Dynamics*, Progress of Theoretical Physics Supplement, 142 (2001), p. 205.

[24] H. Kräwinkel, H. W. Becker, L. Buchmann, J. Görres, K. U. Kettner, W. E. Kieser, R. Santo, P. Schmalbrock, H. P. Trautvetter, A. Vlieks, C. Rolfs, J. W. Hammer, R. E. Azuma, and W. S. Rodney, *The* $^{3}He(\alpha,\gamma)^{7}Be$ *reaction and the solar neutrino problem*, Zeitschrift fur Physik, 304 (1982), p. 307.

[25] N. Michel, *Precise coulomb wave functions for a wide range of complex ℓ, η and z*, Computer Physics Communications, 176 (2007), p. 232.

[26] T. Milosic, *Nuclear reactions within Fermionic Molecular Dynamics*, Master's thesis, Technische Universität Darmstadt, 2006.

[27] A. Mukhamedzhanov and R. Tribble, *Connection between asymptotic normalization coefficients, subthreshold bound states, and resonances*, Physical Review C, 59 (1999), p. 3418.

[28] T. Neff and H. Feldmeier, *Tensor correlations in the unitary correlation operator method*, Nuclear Physics A, 713 (2003), p. 311.

[29] T. Neff and H. Feldmeier, *Clustering and other exotic phenomena in nuclei*, in Proceedings of the International Les Houches School on "Exotic Nuclei: New Challenges", 2007.

[30] ——, *Clustering and other exotic phenomena in nuclei*, The European Physical Journal - Special Topics, 156 (2008), p. 69.

[31] A. Nogga, H. Kamada, and W. Glöckle, *Modern Nuclear Force Predictions for the α-particle*, Physical Review Letters, 85 (2000), p. 944.

[32] J. L. Osborne, C. A. Barnes, R. W. Kavanagh, R. M. Kremer, G. J. Mathews, J. L. Zyskind, P. D. Parker, and A. J. Howard, *Low energy $^3He(\alpha,\gamma)^7Be$ cross-section measurements*, Physical Review Letters, 48 (1982), p. 1664.

[33] P. D. Parker and R. W. Kavanagh, *$^3He(\alpha,\gamma)^7Be$ Reaction*, Physical Review, 131 (1963), p. 2578.

[34] P. Ring and P. Schuck, *The Nuclear Many-Body Problem*, Texts and Monographs in Physics, Springer-Verlag, 1980.

[35] C. Rolfs and W. Rodney, *Cauldrons in the Cosmos*, Theoretical Astrophysics Series, The University of Chicago Press, 1988.

[36] R. Roth, *Ab initio nuclear structure calculations with transformed realistic interactions*, The European Physical Journal - Special Topics, 156 (2008), p. 191.

[37] R. Roth, H. Hergert, P. Papakonstantinou, T. Neff, and H. Feldmeier, *Matrix elements and few-body calculations within the unitary correlation operator method*, arXiv:nucl–th/0505080, Physical Review C, 72 (2005).

[38] R. Roth, T. Neff, H. Hergert, and H. Feldmeier, *Nuclear structure based on correlated realistic nucleon–nucleon potentials*, Nuclear Physics A, 745 (2004), p. 3.

[39] R. Roth, P. Papakonstantinou, N. Paar, H. Hergert, T. Neff, and H. Feldmeier, *Hartree-fock and many body perturbation theory with*

correlated realistic NN interactions, arXiv:nucl–th/0510036v1, Physical Review C, 73 (2006).

[40] J. J. Sakurai, *Modern Quantum Mechanics*, Addison-Wesley Publishing Company, revised ed., 1994.

[41] B. S. Singh, M. Hass, Y. Nir-El, and G. Haquin, *New Precision Measurement of the* $^3He(\alpha,\gamma)^7Be$ *Cross Section*, Physical Review Letters, 93 (2004).

[42] R. J. Spiger and T. A. Tombrello, *Scattering of* ^3He *by* ^4He *and of* ^4He *by Tritium*, Physical Review, 163 (1967), p. 964.

[43] I. Thompson and A. Barnett, *COULCC: a continued-fraction algorithm for coulomb functions of complex order with complex arguments*, Computer Physics Communications, 36 (1984), p. 363.

[44] ——, *Coulomb and bessel functions of complex arguments and order*, Journal of Computational Physics, 64 (1986), p. 490.

[45] D. Tilley, C. Cheves, J. Godwin, G. Hale, H. Hofmann, J. Kelley, C. Sheu, and H. Weller, *Energy levels of light nuclei A=5,6,7*, Nuclear Physics A, 708 (2002), p. 3.

[46] D. R. Tilley, H. R. Weller, and G. M. Hale, *Energy levels of light nuclei* $A = 4$, Nuclear Physics A, 541 (1992), p. 1.

[47] D. R. Tilley, H. R. Weller, and H. H. Hasan, *Energy levels of light nuclei* $A = 3$, Nuclear Physics A, 474 (1987), p. 1.

[48] C. Ugalde, J. Görres, M. Lugaro, and M. Wiescher, *Rates for reactions relevant to fluorine nucleosynthesis*, Memorie Societa Astronomica Italiana, 75 (2004), p. 712.

[49] D. A. Varshalovich, A. N. Moskalev, and V. K. Khersonskii, *Quantum Theory of Angular Momentum*, World Scientific Publishing Company Pte Ltd, 1988.

[50] J. Wheeler, *Molecular viewpoints in nuclear structure*, Physical Review, 52 (1937), p. 1083.

[51] R. B. Wiringa, V. G. J. Stoks, and R. Schiavilla, *Accurate nucleon-nucleon potential with charge-independence breaking*, Physical Review C, 51 (1995), p. 38.

[52] S. Wong, *Introductory nuclear physics*, Prentice Hall Advanced Reference Series, Prentice Hall, 1990.

Acknowledgements

I would like to thank my supervisor Professor Hans Feldmeier for opening up to me the fascinating world of nuclear physics, but more importantly for his intuitive explanations and amazing patience. The generosity with which he gives of his time is much appreciated by all. I have greatly enjoyed our many discussions over such a wide range of topics.

I am very grateful to Professor Karlheinz Langanke for the opportunity to come to Germany and work in the theory department and before that to work with him in Denmark.

Thanks to Dr. Thomas Neff for his well maintained FMD code and for explanations of things both technical and scientific.

Thank you to Heide Rinnert for so many things that she has done for me in the time I have been in Germany and for being such a cheerful and helpful presence in the department.

Thank you to my colleagues in the theory department who have made my time at GSI so enjoyable by providing a congenial and friendly working environment. I would especially like to thank Timo Milosic for his collaboration and friendship over the last three years. Thanks also to the rest of the FMD 'crowd' past and present for fruitful discussions and their help during my time here.

Thank you to the German people for their monetary support and for the welcome I have received as a foreigner in their country.

Thanks are due to Dr. Tony Winzor who first stimulated my interest in physics, in particular nuclear and astrophysics, by his own enthusiasm for the subject.

Thanks to all the friends both back home and abroad that have helped and supported me over the years, especially the Owens; you can never know how much the friendship of all of you means to me.

Thank you to my mother and father for fostering and encouraging my curious nature and helping me to achieve everything that I ever have. Thank you Sarah for many things including convincing me to take part in the Year in Industry scheme. Thanks to my brother who, however far away he is, is always there to help me and can manage with only a few words to cheer me up.

Lastly and most importantly, thank you to my wonderful wife Jennifer for her support, always flavoured with good humour, and her untiring patience particularly in the concluding months of this work; but above all else for agreeing to marry me.

Curriculum Vitae

Name: Robert Cussons

Place of Birth: Ascot

Date of Birth: 9th March 1980

Marital Status: Married

Nationality: British

Education

09 / 1984 - 07 / 1991	Holme Grange Primary School, Wokingham, England.
09 / 1991 - 07 / 1998	St. Bees School, Cumbria, England.
09 / 1998 - 06 / 1999	Technical Assistant (Year in Industry), Capital Controls, Didcot, England.
09 / 1999 - 06 / 2003	Master of Physics with Astrophysics (European), University of Leeds, England.
10 / 2003 - 09 / 2004	Research Assistant, TRIUMF, Vancouver, Canada.
03 / 2005 - 07 / 2008	PhD position at the Gesellschaft für Schwerionenforschung, Darmstadt, Germany.

Erklärung

Hiermit erkläre ich an Eides statt, daß ich die vorliegende Dissertation selbständig verfaßt, keine anderen als die angegebenen Hilfsmittel verwendet und noch keinen Promotionsversuch unternommen habe.

Darmstadt, den 16. Juni 2008,

gez. Robert Cussons.

Unterschrift